A PHYSICS-BASED MODEL FOR INFLOW CHARACTERISTICS OF MULTI-ROTOR CONFIGURATIONS

A Dissertation
Presented to
The Academic Faculty

by

Po-Wei Chen

In Partial Fulfillment
of the Requirements for the Degree
Doctor of Philosophy in the
School of Aerospace Engineering

Georgia Institute of Technology
December 2021

A PHYSICS-BASED MODEL FOR INFLOW CHARACTERISTICS OF MULTI-ROTOR CONFIGURATIONS

Approved by:

Dr. Lakshmi N. Sankar, Advisor
School of Aerospace Engineering
Georgia Institute of Technology

Dr. Jechiel Jagoda
School of Aerospace Engineering
Georgia Institute of Technology

Dr. J.V.R. Prasad
School of Aerospace Engineering
Georgia Institute of Technology

Dr. Xiaomeng 'Shine' Zhai
Numeca R&D
Cadence Design Systems

Dr. Daniel P Schrage
School of Aerospace Engineering
Georgia Institute of Technology

Date Approved: August 11, 2021

Dedicated to my wife,

Yi-Ting Wu

for her unconditional love and support

ACKNOWLEDGEMENTS

My sincere and heartfelt thanks to my advisor and mentor, Dr. Lakshmi N. Sankar, for his consistent support and valuable guidance throughout my doctoral studies at Georgia Tech. I am also thankful to him for financially supporting me as a graduate researcher under his projects.

I would like to thank Dr. J. V. R. Prasad for giving me the opportunity to work with him and for providing helpful feedback throughout the research. His vast knowledge of helicopter inflow models and rotorcraft flight control shaped much of the inflow modeling work documented in this study. I am also thankful to him for financial support as a graduate researcher under his projects.

I am especially thankful to Professor Daniel P. Schrage for his encouragement and support throughout my studies at Georgia Tech. He has a fountain of information on rotorcraft design methodology, flight control technologies, and life cycle cost modeling of rotorcraft systems. The rotorcraft design course he taught was one of the most enjoyable and stimulating courses at Georgia Tech. My appreciation also goes to the members of the dissertation committee Professor Jechiel Jagoda, and Dr. Xiaomeng 'Shine' Zhai for reviewing this dissertation and providing insightful comments and suggestions.

I would like to thank my lab mates and friends Dr. Zhou Chong, Avani Gupta, Auraluck Pichitkul, Luke S. Battey, Dr. Yong-Boon Kong, Dr. Feyyaz Guner, Petro Junior Milan, Kiran Ravikumar, David Jovel, Kyle Schau, Noah Adam Bern, and Zhenhao Jing for their friendship and support during my doctoral studies.

I am grateful to Dr. Jeewoong Kim (ART Inc.) for being supportive and sharing his experience in GT-Hybrid with me. I would like to thank Dr. Dhwanil Shukla for providing the flow field measurement data for multi-rotor configurations. It has been my pleasure to work with many wonderful people in the Rotorcraft research area including Dr. Chengjian He, Prof. Narayanan Komerath, Dr. Natasha L. Schatzman, and Prof. Ganesh Rajagopalan. Prof. Rajagopalan generously shared with me his insight into rotorcraft aerodynamics and provide a license free version of the flow solver RotCFD. He was always just a phone call away when there were questions on the use of the solver. The world lost a great scholar and a wonderful human being when he passed away unexpectedly a few months ago.

I feel so blessed to have such a great family. They have been very supportive in the choices that I have made, helping me to overcome the difficulties and challenges throughout my doctoral studies.

Lastly, I would like to express my deep appreciation to the unconditionally love and encouragement from my wife. It would have been very difficult for me to conduct this work without her support, and I dedicate this thesis work to my wife, Yi-Ting Wu.

This research is partially funded by the U.S. Government, the U.S. Army Technology Development Directorate, CCDC AvMC, under Technology Investment Agreement W911W6-17-2-0002, entitled Georgia Tech Vertical Lift Research Center of Excellence (GT-VLRCOE) with Dr. Mahendra Bhagwat as the Program Manager.

TABLE OF CONTENTS

LIST OF TABLES

LIST OF FIGURES

LIST OF SYMBOLS AND ABBREVIATIONS

Letter Symbols

AS	Axial Spacing
c	Chord
C_D	Drag coefficient
C_{d0}	Nominal drag coefficient
C_L	Lift coefficient
C_P	Power coefficient
C_T	Thrust coefficient
d	Distance to the nearest wall
D	Drag force, Tangential force, Diameter
e	Total energy
EN	Energy per unit volume
J	Jacobian of transformation
k	Thermal conductivity, Turbulent kinetic energy
L	Lift force, Distance between the shaft center
M	Mach number
max, min	Maximum, minimum
$\mathcal{O}$	Order of the function
p	Static pressure
Q	Flow properties vector

r	Radial location
r_c	Vortex core radius
R	Rotor radius
Re	Reynolds number
S_{ij}	Mean rate of strain tensor
T	Temperature, Thrust, Normal force
$T_{u\infty}$	Flow turbulent intensity
t	Time
u, v, w	Cartesian components of velocity
U, V, W	Contravariant velocity
VS	Vertical Spacing
x, y, z	Cartesian coordinates

Greek Symbols

α	Angle of attack
α_s	Shaft angle
δ_{ij}	Kronecker delta
Δ	Difference, Grid spacing
ε	Turbulent dissipation rate
γ	Specific heat ratio
γ_{BC}	Intermittency distribution function
Γ	Vortex strength
λ_0	Uniform inflow coefficient

λ_{1c}	Fore-to-aft (longitudinal) inflow coefficient
λ_{1s}	Side-to-side (lateral) inflow coefficient
μ	Dynamic viscosity, Advance ratio $V_\infty/\Omega R$
μ_l	Molecular viscosity
μ_t	Turbulent viscosity
ν	Kinematic viscosity
ν_t	Eddy viscosity
ρ	Density
σ	Solidity
θ_0	Collective pitch angle
θ_{1s}, θ_{1c}	Longitudinal cyclic control angle, Lateral cyclic control angle
τ_{ij}	Shear stress tensor component
ξ, η, ζ	Curvilinear coordinates
ψ, Ψ	Azimuth angle
Ω	Shaft angular velocity, Magnitude of the vorticity

Subscripts

i, j, k	Indices in three coordinate directions
i, v	Inviscid, Viscous
L, R	Left and right sides of the cell faces
max	Maximum
n	Normal direction
tip	Rotor tip

x, y, z	Derivatives with respect to Cartesian coordinates
ξ, η, ζ	Derivatives with respect to curvilinear coordinates
∞, inf, ref	Reference value

Superscripts

$n, n+1$	Time levels
$\vec{\ }$	Vector

Abbreviation

2-D	Two Dimensional
3-D	Three Dimensional
AIAA	American Institute of Aeronautics and Astronautics
BLDC	Brushless Direct Current
CFD	Computational Fluid Dynamics
CPU	Central Processing Unit
CUDA	Compute Unified Device Architecture
DAQ	Data Acquisition Device
DBM	Discrete Blade source Model
DSM	Distributed Source Model
eVTOL	Electric Vertical Takeoff and Landing
GPU	Graphics Processing Unit
GUI	Graphic User Interface
HPW	Hover Prediction Workshop
LHS	Left Hand Side

MPI	Message Passing Interface
NASA	National Aeronautics and Space Administration
PCI	Peripheral Component Interconnect
RANS	Reynolds Averaged Navier-Stokes
RHS	Right Hand Side
rpm	Rotation-per-minute
SA	Spalart-Allmaras
SIMPLE	Semi-Implicit Method for Pressure Linked Equations
SM	Streaming Multiprocessor
SPIV	Stereo Particle Image Velocimetry
TFLOPS	Tera Floating-point Operations per Second
UAV	Unmanned Aerial Vehicle
VTOL	Vertical take-off and landing

SUMMARY

A physics-based model for modeling helicopter and autonomous rotor configurations, previously developed for isolated rotors and coaxial rotors in hover and forward flight, has been extended to more general multi-rotor configurations. Simulations for coaxial and tandem rotor configurations have been performed for a number of low and high Reynolds number configurations, and comparisons with test data have been made. The physics behind the rotor interactions has been explored through visualization and analysis of vortex wake trajectories and inflow velocity distributions.

As part of this effort, a fast off-body velocity field analysis that employs GPU processors has been implemented. In addition to computation of inflow velocity field above or below the rotor disks, this approach is capable of rapidly computing and visualizing velocity field on any user specified plane. In many helicopter design studies, the adverse interactions caused by the main rotor wake should be considered in the placement of horizontal and vertical stabilizers, as well as the tail rotors and pusher-propulsors. This capability for rapid calculation and visualization of the off-body flow field would greatly aid the designers in the placement of these components.

A previously developed algebraic transition model that regulates the magnitude of the production term in the Spalart-Allmaras one-equation turbulence model has been independently implemented in the present solver, and in the commercial CFD solver ANSYS Fluent as a user-defined function. Previous validation of this model was limited to 2-D flow over airfoils in the transitional Reynolds number regime. In the present work, this model has been also validated for large scale rotors in hover.

CHAPTER 1. Introduction

Vertical take-off and landing (VTOL) vehicles have rapidly evolved over the past century. At first glance, most modern helicopters still have many of the features of the Vought-Sikorsky VS-300 helicopter designed and flown by Igor Sikorsky in 1939 [1]. These features include single main rotor, long tail boom, tail rotor, and stabilizers. However, underneath the skin, modern systems are substantially different than these early systems. Advances in engineering materials, replacement of piston engines with turboshaft systems, advanced drive train components, improved manufacturing processes, electrical/hydraulic control systems and actuators, and digital flight control technologies have all played a major role in this evolution.

In order to reduce the development time and cost, industries and designers are increasingly relying on robust and reliable modeling tools that support and complement comprehensive rotorcraft analyses [2], and multi-disciplinary design methodologies [3, 4]. This reliance has spurred the development of analytical and computational tools for the modeling of solid and fluid dynamics phenomena, advanced flight control models, and control laws.

Over the past decade, interest has also grown on the development and fielding of military and urban air mobility or on-demand mobility applications that can vertically take-off and land [5]. In the United States, NASA researchers and their industry and university partners, are actively collaborating on research activities related to the development of urban air mobility systems, in particular VTOL air taxi operations [6].

These urban and military air mobility systems tend to employ multiple rotors for generation of lift and thrust, and for control. Elimination of the tail boom gives rise to a compact shape and a smaller footprint compared to conventional helicopters. On the other hand, the close proximity of rotors to the airframe gives rise to interaction of the rotor wake with nearby rotors and airframe surfaces. Understanding and anticipating these interactions, and alleviating potential adverse interactions, have become increasingly important while designing these systems.

As may be expected, computational fluid dynamics play an increasingly important role in modeling next generation helicopters. Physics based aeroelastic models of rotors have become routinely available to the industry. These models are well validated for conventional single rotor and coaxial rotor systems. User confidence and experience in these tools has been as a result of joint workshop activities such as the UH-60A Airloads Workshop, AIAA Hover Workshop, and the HART-I and HART-II Workshop.

1.1 Research Motivation

Modern CFD methods attempt to capture the details of the entire flow field over the rotor blades, and the rotor wake. Unfortunately, these “wake capturing” methods require a rather fine grid for an accurate capture of the distorted tip vortex geometry and resolving the boundary layer over the blades. As an example, one of the AIAA Hover Workshop simulations for modeling isolated rotors required 392 million cells, and 275,000 CPU hours on high performance computers [7]. Such detailed simulations are essential for understanding the physical phenomena. On the other hand, a direct application of a similar wake-capturing approach to multi-rotor configurations would drive up the computational

time by an order of magnitude more. One of the primary motivations of the present effort is to reduce the simulation time for modeling multi rotor interactional aerodynamic phenomena.

The dynamic inflow coupling with rotor/body dynamics is also crucial in the analysis of stability and control law design for helicopters. Hence, an accurate yet efficient estimate of the rotor inflow is essential. Over the past several decades, finite-state inflow models for single rotor configurations in hover, forward flight, and maneuver have been well developed [8-10]. With the advent of high-speed coaxial helicopters, and multi-rotor drones, the focus of the dynamic inflow modeling has shifted from single rotors to coaxial and tandem rotor configurations. [11-14]. Pressure potential and velocity potential based dynamic inflow models both have been developed. By capturing the interference effects between rotors, the extension of pressure potential finite state inflow model has promising result for coaxial rotor configuration. These promising results for coaxial rotors have led to extension of this approach to tandem rotor configurations [15-17].

Dynamic inflow models rely on a linear superposition of the velocity potential (or pressure potential) for the individual rotors and acknowledge the presence of adjacent interfering rotors. These linear methods, however, capture interference effects of adjacent rotors only to a first order. These approaches cannot capture secondary effects such as wake contraction and distortion, viscous wake dissipation, rotor-wake interaction, and wake-wake interaction. Where possible, it is a common practice to apply empirical corrections to these models using additional knowledge of the flow field and the wake structure. A second motivation of the present effort is to develop a computationally efficient physics-

based process for predicting distorted rotor wake geometry and interactions and rotor inflow, that would facilitate further development dynamic inflow models.

1.2 Related Prior Research

While a majority of helicopters currently in operation use a single main rotor and a tail rotor, there has been considerable interest in the research community and in industry on the use of tandem rotors and coaxial rotors. These systems eliminate the need for a tail rotor leading to a more compact system.

1.2.1 Coaxial rotors

In Russia, the Kamov Company developed Ka-27 around 1969, and flight tests began in 1973 [18]. This vehicle and its successors, including Ka-50 [19] are in civilian and military operations around the world.

In the United States, the ever-growing need for higher forward speeds, limited by retreating blade stall in the case of conventional single rotor helicopter systems, has led to a renewed interest in coaxial rotors. In an innovation known as the “Advancing Blade Concept” the rotor blades are unloaded on the retreating side, eliminating the possibility of dynamic stall. Only the advancing side of the rotor disk generates useable lift. With the coaxial rotor, each of the two counter-rotating rotors generate equal amounts of lift providing roll balance [20]. Sikorsky Aircraft built and tested an X2 Technology Demonstrator during the 2005-2008 period [21-23]. Over the past decade, Sikorsky Aircraft has developed and demonstrated several derivatives of the X2 Technology Demonstrator, varying in speed, gross weight, and capability.

The increased interest in coaxial rotor systems has spurred the development of computational methods and experimental studies related to these systems. Coleman has conducted a comprehensive review of research in this field during the past decades [24]. McAlister et al. have documented experimental and numerical studies of a smalls scale coaxial model rotor tested at NASA Ames [25].

As in the case of conventional single rotors, coaxial rotors were first modeled using Lagrangian vortex wake models, with a table look of the airfoil aerodynamic characteristics [26, 27]. Wachspress et al. have examined the use of these methodologies for assessing coaxial rotor design, including the noise impact [28].

Conventional comprehensive analyses do an excellent job of modeling the performance of the coaxial rotors [29-31]. With the advances in computational fluid dynamics and the availability of faster shared and distributed memory computer systems, attention has turned to computational methods. Vorticity and vortex particle transport equation solvers coupled to a lifting line representation of the coaxial rotor blades have also been employed [32-34]. Kim et al. solved the Vorticity transport equations and the associated velocity field on an adaptive Cartesian grid, and the rotors were modeled as embedded actuator lines that rotate above their axes [35]. Ruzicka et al. used an early version of the OVERFLOW overset grid based Navier-Stokes solver for modeling coaxial rotors [36]. Lakshminarayan and Baeder performed compressible Reynolds Averaged Navier Stokes (RANS) analyses of the coaxial rotor unsteady aerodynamics under hovering conditions [37]. Egolf et al. used an early version of the hybrid methodology described in this work to study the forward flight performance of coaxial rotors [38].

Additional work has also been done using physics-based models, particularly CFD methods, to better understand the complex physical interaction between the adjacent rotors [39-42]. Barbely et al. [43] have presented a comprehensive survey of recent studies related to coaxial rotor phenomena. Researchers at Georgia Institute of Technology have developed a physics-based, computationally efficient, hybrid Navier-Stokes/free wake tool called GT-Hybrid for analyzing conventional and coaxial rotors [44, 45]. All these benefited from the availability of well documented experimental data [46].

1.2.2 Tandem rotors

Tandem rotor helicopters, similar to coaxial rotor helicopters, use counter-rotating rotors. Because the lift is distributed over two rotors that are laterally spaced apart, these vehicles allow a large variation in the center of gravity compared to coaxial and single rotor helicopters, and good longitudinal stability. These helicopters have been in development and use for a considerable period of time. The most popular of these may be Boeing CH-47 Chinook, with over 1200 units in operation [47]. The classical text by Stepniewski and Keys includes a wealth of information on the aerodynamic characteristics of tandem rotor helicopters [48].

Dingledein has presented one of the earliest wind tunnel studies on the performance of multi-rotor configurations [49]. Sweet performed experimental studies of the hovering performance of large-scale tandem rotor helicopter models at two different solidities at the Langley full scale wind tunnel [50]. He presented data for rotor thrust, torque, and blade flapping. Sweet observed that a tandem rotor with 76-percent-radius overlap required 14% more induced power in hover, relative to an isolated rotor of equivalent disk area. Sweet

also found that, above a shaft-to-shaft distance of 1.03 diameter, the performance of the tandem rotor was nearly the same as two isolated rotors. Huston conducted wind tunnel studies of tandem rotor helicopters for a variety of rotor spacings, and has documented the rotor performance, airloads, and blade motion [51]. Ramasamy has experimentally studied the interference effects associated with coaxial, tandem, and tilt-rotor configurations [52]. Similar to Sweet, Ramasamy also did not find significant aerodynamic interference between the rotors when the shaft-to-shaft distance was greater than 1.10 times the front rotor radius.

Comprehensive analyses are also widely used for modeling tandem rotor and other compound helicopter configurations. Yeo and Johnson used the CAMRAD-II analysis to look at heavy lift compound rotor configurations [53]. Lee et al. have used a time marching free wake methodology for modeling tandem rotors with the rotor blades represented using a panel method that employed source and doublet singularities. These researchers have also examined the effects of rotor overlap [54, 55]. Bagai et al. have conducted free wake analyses of tandem, tilt rotor, and coaxial rotor configurations [26]. Griffith and Leishman have used this approach to examine dual rotor interference and ground effects [56].

Dimanlig et al. have modeled the CH-47 tandem rotor-fuselage configuration using a state-of-the-art CFD solver called OVERFLOW, coupled to a comprehensive analysis called RCAS [57]. Excellent results for fuselage drag and vibratory loads at the hub were predicted and matched against flight test data. Meadowcroft and Jain have also reported additional results for a similar configuration [58].

Many of the studies for tandem rotors tend to focus on the rotor performance and vibrations. Relatively few studies have focused on rotor inflow model development. Shukla et al. used the SPIV velocity measurement technique to study the wake interactions on low Reynolds number multi-rotor systems [59-63]. Shukla's study focused on the detailed measurement of inflow field for low Reynolds number multi-rotor configurations. The hybrid methodology described in this document has been used to model these flows [64-67].

1.2.3 Inflow model development

Work has also been done on the development of physics based inflow models for flight control applications. Zhao et al. combined the classical finite state dynamic inflow model [8, 9] with a vortex particle method to develop inflow data and rotor loads suitable for flight simulations [34].

Xin et al. have explored the use of a free wake model to estimate the interference velocities above and below the rotor disk, and used this information to express the influence coefficient matrix in the form of Pitt-Peters inflow model [68]. Rand et al. have attempted to extract inflow models from high fidelity aerodynamics tools [69-71]. A viscous vortex particle method was used by He et al. for extracting inflow models for coaxial rotor configurations [72].

Prasad et al., Nowak et al., and Kong et al. have employed a pressure potential superposition approach for the development of finite state inflow models [11-15, 73-75]. Guner et al. have developed a velocity potential superposition approach for the development of finite state inflow models [76]. This model has also been used to analyze

tandem rotor inflow velocity field [77, 78]. CFD results from a version of the hybrid methodology has also been used to extract inflow models [64-67].

1.3 Research Objectives

A primary objective of the present study is to extend and validate a hybrid Navier-Stokes/ free wake methodology, previously used to model single rotors and coaxial rotors, to more general multi-rotor configurations operating over a broad range of laminar, transitional, and turbulent flow conditions.

A second objective of this research is to characterize the rotor inflow and wake structure and make it available in a form suitable for use in dynamic inflow models.

1.4 Organization of the Document

The rest of this document is organized as follows. Chapter 2 addresses the mathematical formulation and solution methodologies related to hybrid Navier-Stokes/free wake models, as well as the enhancement of these models for multi-rotor interactions. Chapter 3 focuses on modeling large scale coaxial and tandem rotors, both from an induced power perspective, and the quantification of the rotor inflow velocity field. Chapter 4 focuses on detailed modeling of the interactional phenomena related to small scale overlapping tandem rotors, and comparisons with measured inflow. Chapter 5 gives a summary of the contributions of this research work to the state of the art, and presents conclusions based on the simulations and a list of recommended future studies.

Appendix A documents a one-equation turbulence model used in this study, including the incorporation of a transition model implemented as part of this research. This model is validated for 2-D airfoils and an S-76 rotor in hover.

The configurations discussed in Chapter 4 include a matrix of lateral and vertical displacement of the rotors. This in turn led to a large number of simulations, for the express purpose of capturing the details of the rotor inflow. Chapter 4 includes only a small subset of these simulations, for brevity. Appendix B includes a more complete set of computed results.

Appendix C gives detailed specifications regarding the architecture of the GPU processor units used in this work.

CHAPTER 2. Methodology

In this chapter, the methodologies used in present study will be introduced including the computational fluid dynamics tools, the free-wake model, and the method of extracting the inflow coefficients.

2.1 Computational Fluid Dynamics Methodologies and Tools

The bulk of the analyses reported in this work were done using an enhanced version of a hybrid Navier-Stokes/free wake methodology. The baseline Navier-Stokes/free wake methodology is described first. The baseline is limited to modeling single rotors and coaxial rotors. Enhancements to the baseline solver, implemented as part of the present work, extending this methodology to multiple rotors, are described next.

While exploring transition models, two dimensional analyses are more useful because of the greater availability of data for airfoils undergoing laminar to turbulent flow transition. For these two-dimensional airfoil analyses, a companion 2-D solver, similar in structure to the 3-D solver, called Dynamic Stall Solver Version 2 (DSS2), was used in present study [79].

For comparison purposes, calculations were also done using a flow analysis called RotCFD from Sukra Helitek, Inc [80, 81].

2.2 Baseline Hybrid Navier-Stokes/Free Wake Analysis

The starting point for this effort us an existing hybrid Navier-Stokes/free wake analysis called GT-Hybrid, developed by researchers in the Computational Fluid Dynamics Lab at Georgia Institute of Technology [82-85]. GT-Hybrid employs a hybrid wake methodology, meaning that the flow field is only resolved within a body-fitted gridded domain surrounding a single rotor blade. Outside of the gridded domain, the rotor wake is efficiently modeled as grid-free field of vorticity elements with a free wake model.

2.2.1 Governing equations in physical and transformed coordinate systems

In the GT-Hybrid analysis, the Reynolds averaged Navier-Stokes (RANS) equations are solved on a body-fitted grid surrounding individual rotor blades and moving and deforming with the rotor blades as shown in Figure 2-1.

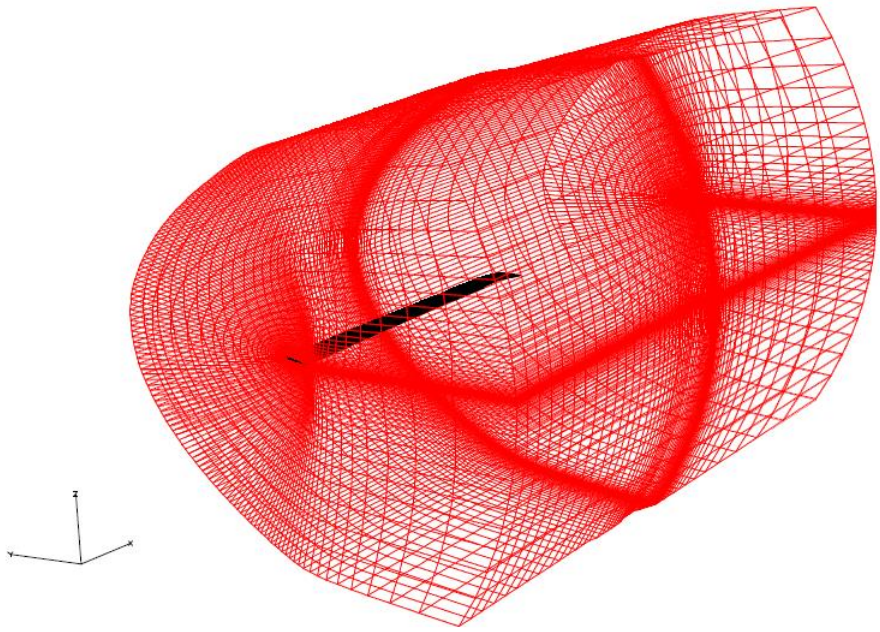

Figure 2-1 Body-fitted grid surrounding a blade

These equations may be written on a Cartesian coordinate system as

$$\frac{\partial Q}{\partial t}+\frac{\partial F}{\partial x}+\frac{\partial G}{\partial y}+\frac{\partial H}{\partial z}=\frac{\partial R}{\partial x}+\frac{\partial S}{\partial y}+\frac{\partial T}{\partial z} \tag{2-1}$$

Here, Q is the flow properties vector:

$$Q=\begin{Bmatrix}\rho\\ \rho u\\ \rho v\\ \rho w\\ e\end{Bmatrix} \tag{2-2}$$

The quantity e is the total energy per unit volume related to the static pressure p, density ρ, and the Cartesian components of velocity (u, v, and w) by

$$e=\frac{p}{\gamma-1}+\frac{1}{2}\rho(u^2+v^2+w^2) \tag{2-3}$$

The quantities F, G, H are flux vectors given by

$$F=\begin{Bmatrix}\rho\\ \rho u^2+p\\ \rho uv\\ \rho uw\\ u(e+p)\end{Bmatrix}, G=\begin{Bmatrix}\rho\\ \rho uv\\ \rho v^2+p\\ \rho vw\\ v(e+p)\end{Bmatrix}, H=\begin{Bmatrix}\rho\\ \rho uw\\ \rho vw\\ \rho w^2+p\\ w(e+p)\end{Bmatrix} \tag{2-4}$$

The right side of the Navier-Stokes equations contain the viscous terms given by

$$R = \begin{Bmatrix} 0 \\ \tau_{xx} \\ \tau_{yx} \\ \tau_{zx} \\ EN_x \end{Bmatrix}, S = \begin{Bmatrix} 0 \\ \tau_{xy} \\ \tau_{yy} \\ \tau_{zy} \\ EN_y \end{Bmatrix}, T = \begin{Bmatrix} 0 \\ \tau_{xz} \\ \tau_{yz} \\ \tau_{zz} \\ EN_z \end{Bmatrix} \tag{2-5}$$

The last row of equations (2-5) above correspond to the viscous work and heat conduction terms, as follows.

$$EN_x = u\tau_{xx} + v\tau_{xy} + w\tau_{xz} + k\frac{\partial T}{\partial x}$$

$$EN_y = u\tau_{xy} + v\tau_{yy} + w\tau_{yz} + k\frac{\partial T}{\partial y} \tag{2-6}$$

$$EN_z = u\tau_{xz} + v\tau_{yz} + w\tau_{zz} + k\frac{\partial T}{\partial z}$$

In the above equation, k is the conductivity, and the viscous stresses are related to the velocity gradients based on Stokes relations.

The curvilinear grid (x, y, z, t) surrounding the blades may be numerically mapped on a Cartesian system (ξ, η, ζ, τ) as follows, acknowledging the fact that the grid may be moving in space, and deforming with time t due to bending and torsional motion of the blades.

$$\frac{\partial \hat{Q}}{\partial \tau} + \frac{\partial \hat{F}}{\partial \xi} + \frac{\partial \hat{G}}{\partial \eta} + \frac{\partial \hat{H}}{\partial \zeta} = \frac{M}{Re}\left[\frac{\partial \hat{R}}{\partial \xi} + \frac{\partial \hat{S}}{\partial \eta} + \frac{\partial \hat{T}}{\partial \zeta}\right] \tag{2-7}$$

In the above equation, the tip Mach number M and the Reynolds number Re, arise from the non-dimensionalization of flow equations. All velocities, flow and grid velocities both, are non-dimensionalized based on the speed of sound. Reynolds number is based on a reference length such as the rotor radius, freestream density, the rotor tip speed, and molecular viscosity.

The mapping may be formally written as

$$\begin{aligned} \tau &= t \\ \xi &= \xi(x, y, z, t) \\ \eta &= \eta(x, y, z, t) \\ \zeta &= \zeta(x, y, z, t) \end{aligned} \tag{2-8}$$

Where

$$\begin{aligned} \hat{Q} &= \frac{Q}{J} = \frac{1}{J}\begin{Bmatrix} \rho \\ \rho u \\ \rho v \\ \rho w \\ e \end{Bmatrix} \\ \hat{F} &= \frac{1}{J}\left(F\xi_x + G\xi_y + H\xi_z + q\xi_t\right) \\ \hat{G} &= \frac{1}{J}\left(F\eta_x + G\eta_y + H\eta_z + q\eta_t\right) \\ \hat{H} &= \frac{1}{J}\left(F\zeta_x + G\zeta_y + H\zeta_z + q\zeta_t\right) \\ \hat{R} &= \frac{1}{J}\left(R\xi_x + S\xi_y + T\xi_z\right) \\ \hat{S} &= \frac{1}{J}\left(R\eta_x + S\eta_y + T\eta_z\right) \\ \hat{T} &= \frac{1}{J}\left(R\zeta_x + S\zeta_y + T\zeta_z\right) \end{aligned} \tag{2-9}$$

Here J is the Jacobean of transformation, given by

$$J \equiv \frac{\partial(x,y,z)}{\partial(\xi,\eta,\zeta)} \equiv \begin{bmatrix} x_\xi & y_\xi & z_\xi \\ x_\eta & y_\eta & z_\eta \\ x_\zeta & y_\zeta & z_\zeta \end{bmatrix}$$

$$= \frac{1}{x_\xi\left(y_\eta z_\zeta - y_\zeta z_\eta\right) + x_\eta\left(y_\zeta z_\xi - y_\xi z_\zeta\right) + x_\zeta\left(y_\xi z_\eta - y_\eta z_\xi\right)} \tag{2-10}$$

The metrics of transformation are defined as follows:

$$\begin{aligned} \xi_x &= J\left(y_\eta z_\zeta - y_\zeta z_\eta\right) & \eta_x &= J\left(y_\zeta z_\xi - y_\xi z_\zeta\right) & \zeta_x &= J\left(y_\xi z_\eta - y_\eta z_\xi\right) \\ \xi_y &= J\left(x_\zeta z_\eta - x_\eta z_\zeta\right) & \eta_y &= J\left(x_\xi z_\zeta - x_\zeta z_\xi\right) & \zeta_y &= J\left(x_\eta z_\xi - x_\xi z_\eta\right) \\ \xi_z &= J\left(x_\eta y_\zeta - x_\zeta y_\eta\right) & \eta_z &= J\left(x_\zeta y_\xi - x_\xi y_\zeta\right) & \zeta_z &= J\left(x_\xi y_\eta - x_\eta y_\xi\right) \end{aligned} \tag{2-11}$$

Finally, the quantities U, V, and W are the contravariant components of velocity:

$$\begin{aligned} U &= \xi_t + u\xi_x + v\xi_y + w\xi_z \\ V &= \eta_t + u\eta_x + v\eta_y + w\eta_z \\ W &= \zeta_t + u\zeta_x + v\zeta_y + w\zeta_z \end{aligned} \tag{2-12}$$

And

$$\begin{aligned} \xi_t &= -x_\tau\xi_x - y_\tau\xi_y - z_\tau\xi_z \\ \eta_t &= -x_\tau\eta_x - y_\tau\eta_y - z_\tau\eta_z \\ \zeta_t &= -x_\tau\zeta_x - y_\tau\zeta_y - z_\tau\zeta_z \end{aligned} \tag{2-13}$$

In the equation above, x_τ, y_τ, and z_τ are the grid velocities. For example, for a rotor in forward flight, the grid would move from right to left relative to a stationary inertial observer and will also rotate at an angular velocity of magnitude Ω in radians per second. In that case, we may define the grid velocity in a global inertial coordinate system as

$$x_\tau \vec{\imath} + y_\tau \vec{\jmath} + z_\tau \vec{k} = -\overrightarrow{V_\infty} + \vec{\Omega} \times \vec{r} \tag{2-14}$$

In the case of a vehicle in maneuvers, the hub motion as a function of time, obtained from a flight dynamics simulation, may be added to the grid velocity. While the angular velocity is kept constant in the simulations presented in this work, the present approach allows angular velocity to vary as a function of time. Thus, RPM control of drones and eVTOL configurations may be modelled with the present approach.

2.2.2 Discretized form of governing equations

Since the transformed coordinate system (ξ, η, ζ) is a Cartesian system, with uniform spacing ($\Delta\xi$, $\Delta\eta$, and $\Delta\zeta$ are all chosen to be unity), equation (2-7) above may be discretized as follows:

$$\left(\frac{\partial \hat{Q}}{\partial \tau}\right)_{i,j,k} + \frac{\hat{F}_{i+\frac{1}{2},j,k} - \hat{F}_{i-\frac{1}{2},j,k}}{\Delta\xi} + \frac{\hat{G}_{i,j+\frac{1}{2},k} - \hat{G}_{i,j-\frac{1}{2},k}}{\Delta\eta} + \frac{\hat{H}_{i,j,k+\frac{1}{2}} - \hat{H}_{i,j,k-\frac{1}{2}}}{\Delta\zeta}$$
$$= \frac{M}{Re}\left(\frac{\hat{R}_{i+\frac{1}{2},j,k} - \hat{R}_{i-\frac{1}{2},j,k}}{\Delta\xi} + \frac{\hat{S}_{i,j+\frac{1}{2},k} - \hat{S}_{i,j-\frac{1}{2},k}}{\Delta\eta} + \frac{\hat{T}_{i,j,k+\frac{1}{2}} - \hat{T}_{i,j,k-\frac{1}{2}}}{\Delta\zeta}\right) \tag{2-15}$$

Here

$$\Delta\xi = \xi_{i+\frac{1}{2},j,k} - \xi_{i-\frac{1}{2},j,k} = 1$$

$$\Delta\eta = \eta_{i,j+\frac{1}{2},k} - \eta_{i,j-\frac{1}{2},k} = 1 \tag{2-16}$$

$$\Delta\zeta = \zeta_{i,j,k+\frac{1}{2}} - \zeta_{i,j,k-\frac{1}{2}} = 1$$

The time derivative appearing in equation (2-15) is expressed to first order time accuracy as follows:

$$\left.\frac{\partial\hat{q}}{\partial\tau}\right|^{n+1} = \frac{\hat{q}^{n+1} - \hat{q}^{n}}{\Delta\tau} + \mathcal{O}(\Delta\tau) \tag{2-17}$$

With this approach, setting the mesh spacing in the transformed coordinate system to be unity, the discretized form of the governing equations may be expressed as

$$\begin{aligned}
&\hat{q}^{n+1} - \hat{q}^{n} \\
&+\Delta t\left[\hat{F}_{i+\frac{1}{2},j,k} - \hat{F}_{i-\frac{1}{2},j,k} + \hat{G}_{i,j+\frac{1}{2},k} - \hat{G}_{i,j-\frac{1}{2},k} + \hat{H}_{i,j,k+\frac{1}{2}} - \hat{H}_{i,j,k-\frac{1}{2}}\right]^{n+1} \\
&-\Delta t\left[\hat{R}_{i+\frac{1}{2},j,k} - \hat{R}_{i-\frac{1}{2},j,k} + \hat{S}_{i,j+\frac{1}{2},k} - \hat{S}_{i,j-\frac{1}{2},k} + \hat{T}_{i,j,k+\frac{1}{2}} - \hat{T}_{i,j,k-\frac{1}{2}}\right]^{n+1} = 0
\end{aligned} \tag{2-18}$$

Or, formally, a nonlinear system of algebraic equations of the form

$$P(q^{n+1}, q^{n}) = 0 \tag{2-19}$$

The flux terms in the transformed plane contain information crossing the boundaries of a cell. In compressible flow, information is transported by acoustic waves, entropy waves, and vorticity waves. In order to be physically consistent, the flux terms must be evaluated with information upstream and downstream of any given face, such as $\left(i+\frac{1}{2},j,k\right)$ shown below. For example, acoustic waves may travel with the flow at a velocity (u_n+a), and against the flow at a velocity (u_n-a). Here u_n is the component of the velocity vector (relative to the moving cell face), normal to the face.

Over the past several decades, a number of "upwind" weighted schemes have been developed [86-90]. The most popular of these is the Roe scheme [91], with a third order upwind weighting proposed by Van Leer [92].

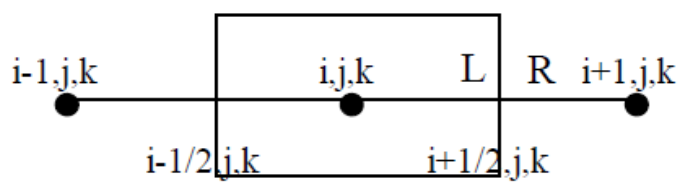

Figure 2-2 Computational domain in the transformed plane

In this approach, we first compute the flow properties just to the left and right side of a given cell face such as $\left(i+\frac{1}{2},j,k\right)$ as follows.

$$q_L = q_{i,j,k} + \frac{1}{4}\left[(1-\kappa)\left(q_{i,j,k}-q_{i-1,j,k}\right)+(1+\kappa)\left(q_{i+1,j,k}-q_{i,j,k}\right)\right]$$

$$q_R = q_{i+1,j,k} - \frac{1}{4}\left[(1-\kappa)\left(q_{i+1,j,k}-q_{i,j,k}\right)+(1+\kappa)\left(q_{i+2,j,k}-q_{i+1,j,k}\right)\right] \tag{2-20}$$

In this equation, κ determines the spatial accuracy. For example, $\kappa = 1/3$ yields third order spatial accuracy.

Once the third order interpolation of the flow properties q_L and q_R at the left and right side of cell spaces are found, the fluxes are found using Roe's approximate Riemann solver as follows:

$$\hat{F}_{i+\frac{1}{2},j,k} = \frac{1}{2}\left\{\left(\hat{F}_L + \hat{F}_R\right) - \left|\tilde{A}\right|(q_R - q_L)\right\}$$

$$q_L = \begin{Bmatrix} \rho_L \\ u_L \\ v_L \\ w_L \\ p_L \end{Bmatrix}, q_R = \begin{Bmatrix} \rho_R \\ u_R \\ v_R \\ w_R \\ p_R \end{Bmatrix} \tag{2-21}$$

Vinokur and Liu [93] have given explicit expressions for these terms.

$$\left|\tilde{A}\right|(q_R - q_L) = \left|\tilde{\lambda}_1\right| \begin{Bmatrix} \Delta\rho \\ \Delta\rho u \\ \Delta\rho v \\ \Delta\rho w \\ \Delta e \end{Bmatrix} + \delta_1 \begin{Bmatrix} \tilde{\rho} \\ \tilde{\rho}\tilde{u} \\ \tilde{\rho}\tilde{v} \\ \tilde{\rho}\widetilde{w} \\ \tilde{\rho}\widetilde{h_0} \end{Bmatrix} + \delta_2 \begin{Bmatrix} 0 \\ \eta_x \\ \eta_y \\ \eta_z \\ \widetilde{U_C} \end{Bmatrix} \tag{2-22}$$

where

$$\delta_1 = C_1 \frac{\Delta p}{\tilde{\rho}\tilde{a}^2} + \frac{1}{2} C_2 \frac{\Delta U_C}{\tilde{a}}$$

$$\delta_1 = C_1 \tilde{\rho} \Delta U_C + \frac{1}{2} C_2 \frac{\Delta p}{\tilde{a}} \tag{2-23}$$

$$C_1 = -\left|\widetilde{\lambda_1}\right| + 0.5\left(\left|\widetilde{\lambda_2}\right| + \left|\widetilde{\lambda_3}\right|\right)$$

$$C_2 = -\left|\widetilde{\lambda_2}\right| - \left|\widetilde{\lambda_3}\right|$$

Here, the operator Δ represents changes in the flow properties from the left to right. Also,

$$\widetilde{\lambda_1} = \widetilde{U}$$
$$\widetilde{\lambda_2} = \widetilde{U} + a$$
$$\widetilde{\lambda_3} = \widetilde{U} - a$$
$$\widetilde{U} = \eta_t + \eta_x \tilde{u} + \eta_y \tilde{v} + \eta_z \tilde{w} = \left(\vec{V} - \overrightarrow{V_G}\right) \cdot \vec{n} \tag{2-24}$$
$$\widetilde{U_C} = n_x \tilde{u} + n_y \tilde{v} + n_z \tilde{w} = \vec{V} \cdot \vec{n}$$
$$\Delta U_C = n_x(u_R - u_L) + n_y(v_R - v_L) + n_z(w_R - w_L)$$

The vector $\vec{n}$ is the unit normal vector with its Caresian componets (n_x, n_y, n_z) at the cell face and the vector $\overrightarrow{V_G}$ is the grid velocity at $\left(i + \frac{1}{2}, j, k\right)$.

2.2.3 Time marching algorithm

With the temporal discretization and spatial discretization briefly discussed above, we get a system of non-linear algebraic equations at any given time level $(n + 1)$ coupling the flow properties q at the cell (i, j, k) to the properties in the neighbour cells. Recall that the discretized form may formally be written as

$$P(q^{n+1}, q^n) = 0 \tag{2-25}$$

P is a non-linear function and includes contributions from the discretized from of the time derivative and the discretized from of the spatial derivatives shown in equation (2-25). It is customary to use a Newton-Raphson iteration scheme, expanding the function about the known value at a previous time step using Taylor series.

$$P(q^{n+1}, q^n) \approx P(q^n) + \left[\frac{\partial P}{\partial q}\right]^n (q^{n+1} - q^n) = 0 \tag{2-26}$$

Here $\frac{\partial P}{\partial q}$ is the derivative of the function P (discretized form of governing equations), and is computed at the previous time level n. Thus, this derivative is explicitly known. Since P involves the properties at the cell and its neighbours both, a coupled linear system of equations results, which may be written as

$$[A](q^{n+1} - q^n) = -P(q^n) \tag{2-27}$$

The matrix A is diagonally dominant, since the main diagonal is of order 1 while the off-diagonal terms are multiplied by Δt, and therefore are of order Δt. One such equation results at each of the nodes (i, j, k). This results in a very large sparse system of simultaneous equations. Each equation contains non-zero elements only along the main diagonal and corresponding the immediate neighbours.

An exact inversion of the above sparse system is costly in terms of arithmetic operations, and memory requirements. For this reason, in the present study, this system is inverted using an incomplete LU factorization scheme as discussed in [94].

2.2.4 Turbulent mixing effects

In turbulent flows, the molecular viscous mixing effects are augmented by an eddy transport of momentum and energy. In RANS equations, it is customary to augment the molecular viscosity μ with $\rho\nu_\tau$, where ν_τ is the eddy viscosity. A variety of eddy viscosity models are available in the baseline solver. In this particular work, the Spalart-Allmaras

one equation model is used. A detailed discussion of the Spalart-Allmaras model, and the modifications to this solver to incorporate the effects of transition, are given in Appendix A.

2.2.5 Full span wake model

In many computational fluid dynamics solvers, the discretized form of the governing equations is solved over the entire flow domain, both the near field surrounding the rotor blades, and the far field wake. This approach is very costly, especially if the wake from the blades need to be resolved accurately. For an accurate resolution of the vortex wake, the required grid spacing will be approximately one-tenth of the vortex core, on the order of millimetres. This would result in billions of grid points. If a coarser grid is used, the vorticity field will be quickly dissipated and the induced flow effects from the wake would not be accurately captured. As a result, adverse effects of the rotor wake on downstream components such as a tail rotor would not be accurately predicted.

In the baseline hybrid solver, the following approach is used. At each radial location on the blade, the lift force per unit span is converted into bound vortices using the classical Biot-Savart law. Due to conservation of angular momentum, any radial variation in the bound circulation would generate a trailing vortex downstream of the blade. Likewise, azimuthal (or temporal) variations in the bound circulation would cause shed vortices to be shed from the blade. Thus, each and every blade would generate its own system of trailing and shed vorticity field, which would be captured and carried away from the rotor by the forward speed.

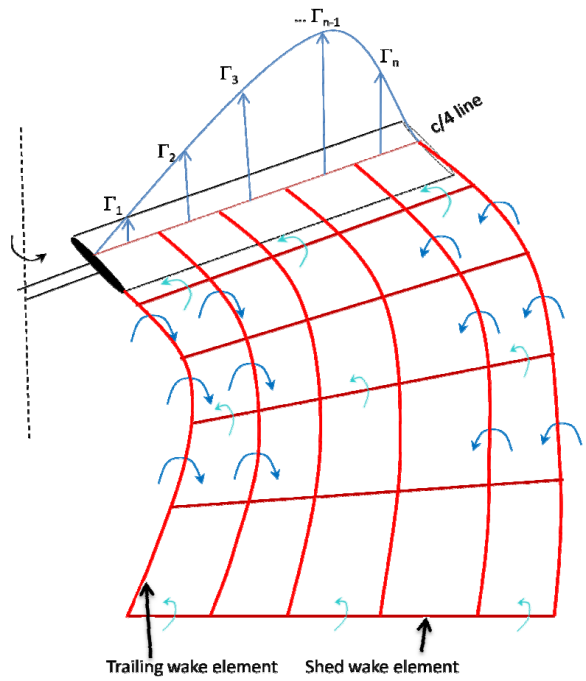

Figure 2-3 Schematic of the trailing and shed wake structures

In the hybrid methodology, the far field is represented by piecewise straight-line elements that form the edges of the trailing and shed vortex structures. To avoid double counting the near field of vorticity in the rotor's immediate wake captured within the body-fitted grid, the wake model keeps track only of the wake elements outside the computational grid.

The distributed structure of shed and trailing vortices shown above would induce a velocity field. This may be evaluated using Biot-Savart law. For a given segment of the vortex, the induced velocity at any "control" point away from that filament may be computed from equation (2-28) as follows:

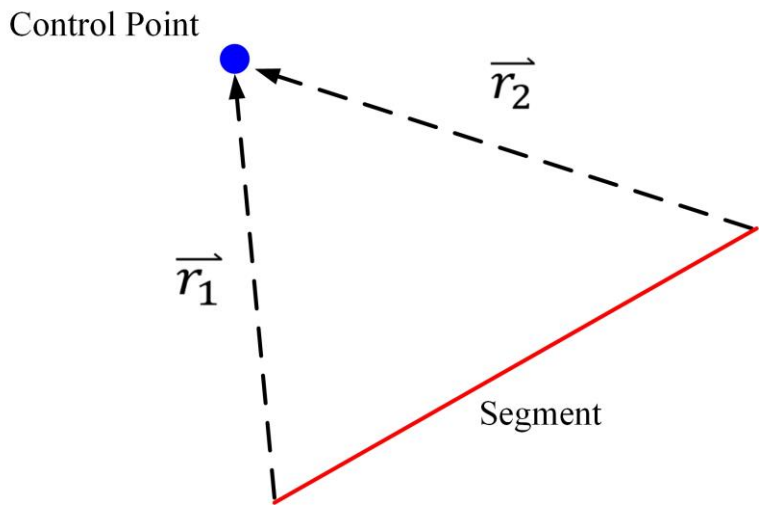

Figure 2-4 Schematic of a vortex filament segment and the control point where induced velocity is computed

$$\vec{V}_{induced} = \frac{\Gamma}{4\pi}\overrightarrow{r_1} \times \overrightarrow{r_2}\frac{(r_1 + r_2)\left(1 - \frac{\overrightarrow{r_1} \cdot \overrightarrow{r_2}}{r_1 r_2}\right)}{(r_1 r_2)^2 - (\overrightarrow{r_1} \cdot \overrightarrow{r_2})^2 + r_c^2(r_1^2 + r_2^2 - 2\overrightarrow{r_1} \cdot \overrightarrow{r_2})} \tag{2-28}$$

In the above equation the quantity r_c is the vortex core. It serves the following purpose. It ensures that the denominator does not go to zero, when the control point approaches the filament, and falls anywhere on the filament. In that event, the denominator would be finite, while the numerator goes to zero. Thus, the induced velocity in the core of the vortex would approach zero, consistent with the Rankine vortex core approximation.

The induced velocity from the vortex wake from all the rotor blades (and all the rotors) is computed and applied as boundary conditions at the inflow boundaries of the body-fitted grid. As a result, the effect of the wake is felt by the solver, while the bound circulation over the rotor blades is coupled to the rotor wake.

The self-induced velocity is also computed at selected points on the rotor wake filaments, as shown in Figure 2-3 above. Since the vorticity field would move with the local flow velocity, the filament location is advanced by a distance over the time period Δt. Thus, the present approach allows a fully distorted wake for a single rotor to form and evolve as shown in Figure 2-5 below. In the case of multi-rotor configurations, additional wake structures from neighbor rotors need to be included in the induced velocity computation. Therefore, the problem size increases by n times, where n is number of rotors in the simulation. Furthermore, while computing the induced velocity on each rotor disk in the multi-rotor configuration, the problem size increases by n^2 times. The GPU CUDA program developed to speed up the induced velocity computation will be addressed in the section 2.7.

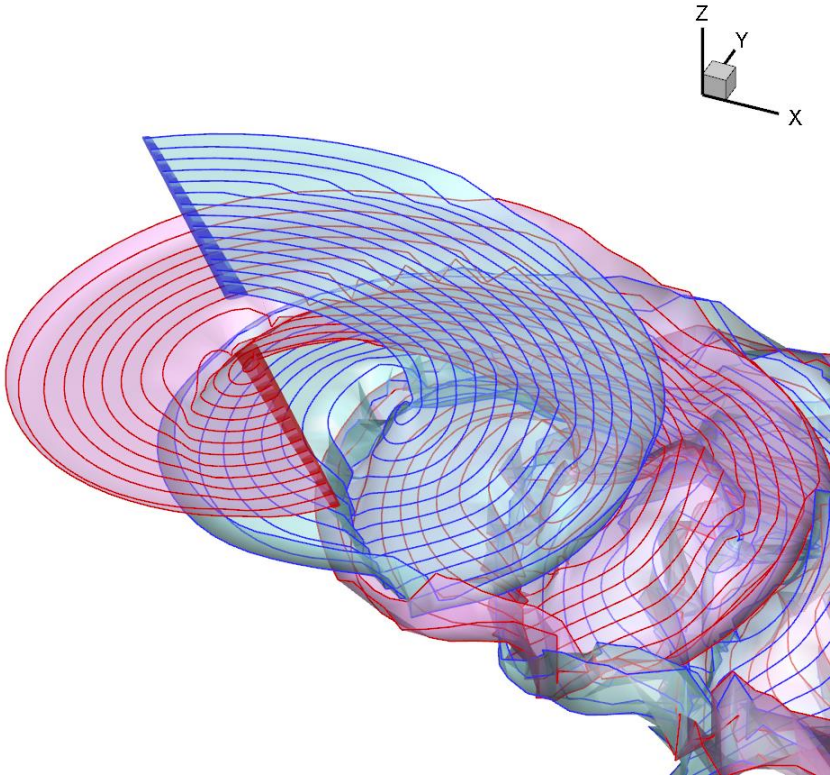

Figure 2-5 Visualization of the distorted rotor wake for a two-bladed rotor

(For clarity, only the trailing filaments are shown)

2.3 **Rotor Trim**

The present formulation predicts all the three components of forces at the shaft (thrust, H-force, and Y-force), and the three moments (torque, pitch, roll) through an integration of the surface pressure and shear forces on individual blades. In the case of multiple rotors, the integrated loads are independently stored for each of the rotors. Additionally, for each rotor at each computational radial location, the sectional forces normal to and along the chord are computed and saved. The sectional pitching moments are also computed. These computed values are saved as ASCII files at user specified azimuth intervals.

In the case of a helicopter in flight (hover, forward flight, or maneuvers), the target values for the forces and moments are specified as part of the flight conditions, in addition to flight speed, rotor RPM, and the shaft tilt as a function of time in an inertial coordinate system. The purpose of rotor trim is to iteratively adjust the collective and cyclic pitch of the individual rotors at each instance in time (averaged over multiple blade revolutions), ensuring that the computed hub forces and moments match the target values. In the present framework, the trim may be done in one of three ways.

The sectional forces and moments at user specified radial locations, at user specified azimuth locations, may be passed on to a comprehensive analysis such as DYMORE, RCAS, or CAMRAD-II in a standardized ASCII file format that is being used in the US helicopter research and development community. The comprehensive analysis performs the rotor trim using the computed CFD airloads, and models the blade flapping and pitching dynamics, as well as the elastic bending and torsional deformations of the

blade. The resulting information about the blade motion (three linear displacements and three rotations at each radial location and selected azimuth locations, including elastic effects) is returned to the flow solver as a "motion file" in a standardized format. The data between the CFD and comprehensive CSD (computational structural dynamics) tools is exchanged over multiple loosely coupled CFD/CSD iterations, until the computed hub forces and moments converge to target values. This approach has been used by a number of researchers within the present research group to model UH-60A rotor in steady level flight, pull up maneuvers, and dive turn maneuvers [44].

Alternatively, for rigid rotors, a simplified manual trim procedure may be used, where the collective and cyclic pitch settings are adjusted iteratively. For example, for the coaxial rotor in hover, an increase in the collective pitch would result in an increase in thrust as well as an increase in torque required to turn the rotor. The lateral and longitudinal cyclic coefficients would affect the rolling and pitching moments and influence the blade flapping dynamics. A three-by-three system of nonlinear equations are solved. A Newton Raphson method is used, with the terms within the 3x3 Jacobians are estimated analytically from classical blade element methods with a uniform inflow. This iterative process may also be modified to ensure that the sum of the rotor torque adds up to zero in the case of coaxial rotors.

Finally, the rotor trim settings may be directly taken from experiments or obtained from outside sources. For example, in the case of the Georgia Tech studies on coaxial and tandem rotors, the individual rotors were connected to separate shafts. The collective pitch was held fixed, and no cyclic variations were applied. These values were directly used in the calculations reported here. No attempt was therefore made to ensure zero net torque. In

the case of Harrington Coaxial Rotor 1 in forward flight, the trim settings obtained by Barbely and Komerath, using CAMRAD-II loosely coupled to RotCFD solver with the discrete blade model were used. These values are readily available in tabulated form [43]. This was done to ensure that the two flow solvers being used (GT-Hybrid and RotCFD) both used identical trim settings.

2.4 Calculation of Sectional Loads, Thrust, and Power

At user specified time intervals, the surface pressure data and skin friction data are computed at several radial locations on the blade. For each radial segment, the surface pressure forces and viscous forces are numerically integrated using Trapezoidal rule to arrive at sectional normal force ΔT (normal to the plane of rotation) and sectional tangential force ΔD (along the plane of rotation) as shown in Figure 2-6.

It should be noted that the inviscid and viscous contributions are individually stored. For example, ΔD would include inviscid drag ΔD_i, as well as the viscous force ΔD_v contributions. The inviscid drag would include induced drag as well as wave drag, in the event shocks form on the blade surface.

These contributions from each blade segment (blade element) are summed up to get the thrust force per blade, at a given azimuthal location. This quantity is multiplied by the total number of blades, and an azimuthal averaging is done in a separate post-processing step (which involves a simple arithmetic average of thrust over 360 azimuthal locations on the rotor disk, 1 degree apart, say) to get azimuthally averaged thrust force T generated by the entire rotor.

The quantity ΔD (equal to $\Delta D_i + \Delta D_v$) is multiplied by the radial location r to get the sectional contribution to torque. Likewise, this quantity is multiplied by the in-plane component of velocity ($\Omega r + V_\infty \cos \alpha_s \sin\Psi$) to arrive at the sectional contribution to induced power and profile power at that particular azimuthal location. Here Ω is the blade angular velocity in radians per second, V_∞ is the forward speed, and α_s is the shaft angle of attack. These quantities are summed up over all blade segments, multiplied by the number of blades, and finally azimuthally averaged to get induced power, and profile power.

These dimensional values of azimuthally averaged thrust and power (profile power and induced power) are subsequently non-dimensionalized to extract C_T, C_{Pi}, and C_{P0}.

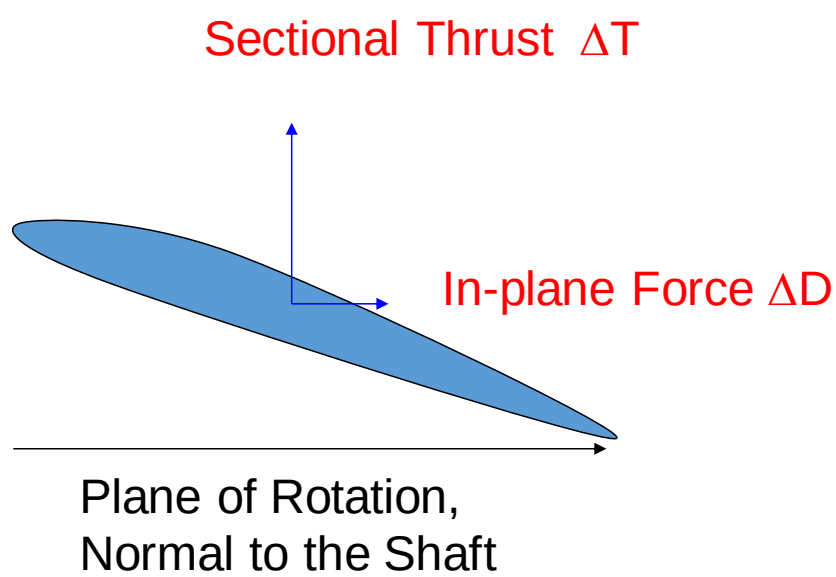

Figure 2-6 Force coordinates for sectional normal force and sectional tangential force

2.5 Computer Resources Requirements

The GT-Hybrid method is computationally very efficient, since the time consuming Navier-Stokes calculations are done only in a small region surrounding the rotor blades. The wake is modeled using discrete line or point vortices. The present simulation, on an eight-core desktop system (Intel® Xeon® E5-1650 v4 processors 3.60GHz), requires 45 minutes of computer time per blade revolution for a single rotor configuration. Calculations are continued for 10 or more revolutions to ensure that the solution has fully converged. The overall CPU time is around 8 hours on a desktop system for a single CFD/CSD iteration. For multiple rotors, the computer time is directly proportional to the number of rotors.

In contrast, wake capturing methods would require hundreds of millions of grid points and a distributed (or a shared memory) computing architecture. Reported computer times are of the order of several hundred hours on these high-speed systems. For example, recent studies for a rotor similar to the S-75 rotor were done on a grid with 393 million points. The computational resources required to generate a solution of 20 rotor revolutions is 275,000 CPU hours. Spread across 1600 processors, the time to generate a solution is over 7 days[95]. These approaches are not presently suitable for design and development studies. However, in spite of the large computer resources required by these methods, it is necessary to pursue such fundamental studies to capture vortex phenomena not adequately modeled by Lagrangian wake models.

2.6 Enhancement to the GT-Hybrid Solver Implemented in the Present Study

As part of the present analysis, the following enhancements were made to the baseline GT-Hybrid solver.

1. The previous version of the analysis was limited to isolated rotors, and coaxial rotors. Thus, all the blades revolved around a single rotor shaft axis. The angular velocity vector was along the shaft axis, clockwise or counterclockwise.

   Under the present study, the analysis was generalized to handle any number of rotors revolving about their own shaft axes. The angular velocity vectors may be pointing in a direction specified at the start of the simulation. As a result, in addition to multi-rotors such as tandem and quad-rotor systems, the present analysis allows main rotor- tail rotor interactions, and rotor-propulsor interactions to be modeled. Ground effects may also be modeled (with the ground plane assumed to be an inviscid symmetry plane) simply by placing image rotors and image trailing vortices beneath the ground plane.

2. The Spalart-Allmaras model implemented in the baseline solver assumes the flow over the rotor blade surfaces to be fully turbulent. While this may be a reasonable assumption for large scale rotors, this approach would yield incorrect results for small scale rotors with Reynolds numbers (based on local chord length) of the order of 10^4 to 10^5.

   To address this deficiency, an existing transition model was implemented in the analysis. Appendix A gives details of the baseline turbulence models, and the implementation of the transition model. This model, to the author's knowledge, has only been implemented for 2-D flows. As part of the present analysis, this model

was validated for rotors in hover. Appendix A includes the 2-D and 3-D validation studies.

3. In the case of multi-rotor configurations, the interaction of the rotor wake with downstream components are of interest. These components may include the tail rotor, pusher propeller, horizontal and vertical stabilizers, and tail booms. A GPU based induced velocity solver was developed which allows the induced velocities on any plane in the flow to be computed in a matter of seconds.

2.7 Inflow Distribution Computation by Using GPU CUDA

The graphics processing unit (GPU) was originally designed to handle computation only for computer graphics which required memory-intensive calculations. Compared to the central processing units (CPU) with a latency-oriented processor architecture, the GPU execute single task slower than CPU. However, GPU processors have a large number of cores and superior memory bandwidth, making these processors well suited for solving massively parallel simulations. Over the past decades, the GPU computing has become an integral part of mainstream computing system [96, 97].

In the current study, a NVIDIA GeForce RTX 2060 SUPER graphics with a Turing architecture card is used. The graphics card specifications are given in Appendix C. The software implemented in this work is based on CUDA which is the native parallel programming platform from NVIDIA. NVIDIA, introduced CUDA in November 2006, originally stood for “Compute Unified Device Architecture”, a parallel computing platform and programming model that leverages the parallel compute engine in NVIDIA GPUs for solving computational problems in a more efficient way than on a CPU.

The workflow and the pseudo code for the parallel induced velocity algorithm by using GPU CUDA are shown in Figure 2-7 and Figure 2-8. After initialization and reading the input file from GT-Hybrid, the program precomputes the size of the wake and prepares the array to store the wake structure. The GT-Hybrid is written in Fortran 90, with data arrays stored in the column-major order. The GPU CUDA program is written in C++ programming language, which expects the data to be available in row-major order. For this reason, the wake data received from the GT-Hybrid solver is first converted into row-major order. This speeds up the memory access process in the following steps. The user specified locations on a 2-D plane where induced velocity values are desired are also stored in a target points array within the GPU solver.

The *cudaMalloc()* API is used to allocate the memory on the device side for the data transferred from the host to the device. The data is copied from host to the device using *cudaMemcpy()*. Once the data is available on the device side, the kernel is launched with user specified dimensions (dimGrid, dimBlock) which corresponds to the size of the target plane. Each thread is assigned one target point, and the threads are executed in parallel. After the computation on the device side is completed, the data is copied back to the host side and the memory is released on the device using *cudaFree()*. Finally, the results are written to an output file for post-processing purposes.

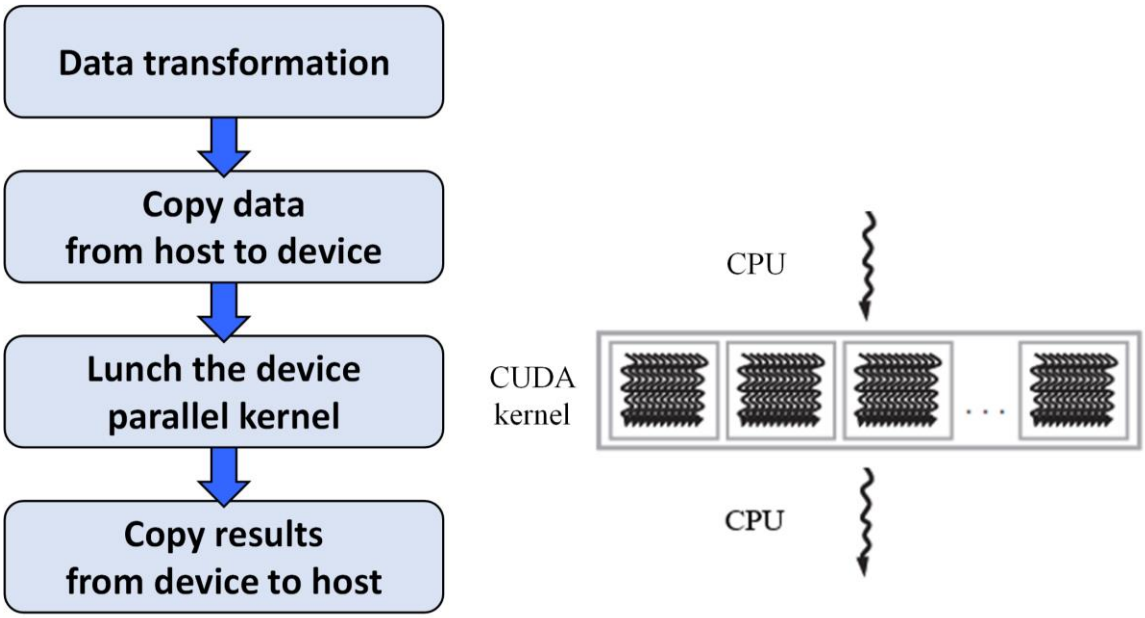

Figure 2-7 Workflow for the induced velocity computation using GPU CUDA

Algorithm : Induced Velocity Computation (GPU CUDA)

```
initialization;
read input file of GT-Hybrid (hybrid.inp);
read output files of GT-Hybrid (wake.xyz and wake.fun);
assign target points;
allocate memory on the device cudaMalloc();
copy data from the host to the device cudaMemcpy();
launch the kernel on the device kernel <<< dimGrid, dimBlock >>> ();
index = threadIdx.x + (blockIdx.x × blockDim.x);
if index < number of target points then
  | loop through ntrailers and nmarkers to compute all the contributions
else
  | do nothing
end
copy data from the device to the host cudaMemcpy();
free memory on the device cudaFree();
write the results to the output file;
```

Figure 2-8 Pseudo code for the parallel induced velocity algorithm

Three version of the induced velocity calculations have been implemented. The first version uses serial execution on a single processor. The second version uses message passing interface (MPI) to exchange data between the processors on a distributed computer system. This version utilized 24 processors and 18 fold speed up was achieved. The GPU CUDA version achieved a hundredfold speed up in computer time, compared to the serial CPU-based version. The run-time comparison between these three methods is shown in Table 2-1 below.

Table 2-1 Run-time and speed up comparison between serial, MPI, and GPU CUDA

	Run-time	Speed-up
Serial	~2000s	1
MPI (24 processors)	~110s	~18
GPU CUDA	~20s	~100

2.8 Extraction of the Dynamic Inflow Model

The computed inflow velocity field normal to the rotor disk is a function of non-dimensional radial location $\vec{r}$ and azimuth angle ψ. In many fight dynamics applications, only the azimuthally induced velocity component, and the one-per-rev variations are of interest. The following methodology from [17] is used to reduce this data from the CFD calculations.

The induced velocity $\overrightarrow{v_z}(\vec{r},\psi)$ at the rotor disk, normalized by the rotor tip speed, is related to the mean thrust, and the rolling and pitching moments generated by the rotor at the hub and may be expressed as a series. The first few terms of this series are:

$$\overrightarrow{v_z}(\vec{r},\psi) = \lambda_0 + \lambda_{1c}\vec{r}\cos(\psi) + \lambda_{1s}\vec{r}\sin(\psi) \tag{2-29}$$

Since the induced velocity is available from CFD simulations, we may compute λ_0, λ_{1c}, and λ_{1s} as:

$$\lambda_0 = \frac{1}{\pi}\int_0^{2\pi}\int_0^1 \overrightarrow{v_z}(\vec{r},\psi)\vec{r}d\vec{r}d\psi$$

$$\lambda_{1c} = \frac{4}{\pi}\int_0^{2\pi}\int_0^1 \overrightarrow{v_z}(\vec{r},\psi)\vec{r}^2 cos(\psi)d\vec{r}d\psi \tag{2-30}$$

$$\lambda_{1s} = \frac{4}{\pi}\int_0^{2\pi}\int_0^1 \overrightarrow{v_z}(\vec{r},\psi)\vec{r}^2 \sin(\psi)\, d\vec{r}d\psi$$

2.9 RotCFD

RotCFD is widely used in the rotorcraft industry [80, 81, 98-100]. With a user-friendly graphic user interface (GUI), one can access either the Rot3DC structured solver or the RotUNS unstructured solver. The flow solver in RotUNS is a finite volume based SIMPLE solution algorithm for pressure-velocity coupling. The solver uses a k-ε turbulence model. Two options are available for modeling rotors: the discrete blade source model (DBM) and the distributed source model (DSM). Both options rely on user-provided tables of two-dimensional airfoil load coefficients for a range of angle-of-attack and Mach number. Using the computed velocity field at the rotor disk, the sectional angles-of-attack and the Mach number are computed at several radial sections. The corresponding aerodynamic coefficients are retrieved from the airfoil tables. The sectional forces and moments are then converted into source terms that are added to the momentum equations at the grid cells that encompass the blade section. In this study, the distributed source model (RotUNS) has been used.

CHAPTER 3. High Reynolds Number Multi-Rotor Simulations

In the previous chapter, extensions to the hybrid Navier-Stokes methodology for modeling multi-rotor configurations were discussed. The specific extensions include the ability to handle multiple tip vortex and inner wake structures that mutually interact and undergo extensive deformation. These extensions also allow the methodology to handle rotors that are placed with a user specified vertical and horizontal offset distances. Scenarios where the rotor shaft axes are pointing in different directions (as in the case of rotor-propulsor interactions) may also be handled. These extensions allow a broader variety of configurations, representative of modern eVTOL and drone configurations, to be modeled without approximations related to airfoil tables, tip losses, analytically derived non-uniform inflow models, etc. The present approach may also be readily coupled to an elastic analysis of the rotor blades allowing a full aeroelastic simulation of these systems.

In this chapter, two specific applications of the present approach are presented, and compared against available test data.

3.1 Coaxial Harrington Rotor

Harrington performed one of the earliest experimental studies of full scale coaxial rotors in the Langley full scale wind tunnel in 1951 [46]. He examined the aerodynamic performance of two rotor blade planforms, commonly referred to as Rotor 1 and Rotor 2. The coaxial rotors had two-bladed rotors, with a 25-foot diameter.

Rotor 1 had a more complex geometry with a solidity of 0.027 per rotor (0.054 for both rotors), with the blades tapering from root to tip with a tip-to-root chord ratio of 0.35. As shown in Figure 3-1, the airfoils also varied in thickness from the root, with a thickness-to-chord ratio t/c of 0.31 at the root, and a t/c of 0.12 at the tip. The vertical spacing between the upper and lower rotors was of 9.3% of the rotor diameter.

Rotor 2 had a much simpler geometry, with constant-chord blades with a solidity of 0.076 per rotor (0.152 for both rotors). The blades were linearly tapered in thickness (31% chord at root to 15% at tip). The rotor spacing for Rotor 2 was 8.0% of the rotor diameter.

In this study, Rotor 1 configuration is being modeled. A piecewise linear interpolation of the blade surface is done in the radial direction based on the supplied information at these stations.

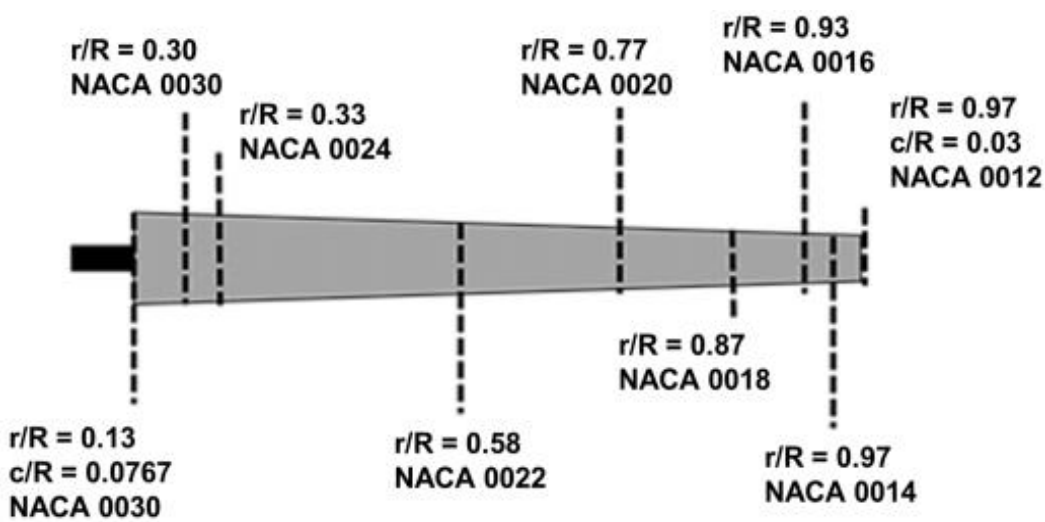

Figure 3-1 Harrington rotor1 blade geometry

This rotor has been extensively studied by a number of researchers, although most simulations have focused only on the rotor performance, i.e. variation of power with thrust. These studies include computational fluid dynamics solvers based on Reynolds averaged Navier-Stokes methods [101], unsteady surface panel methods with a free wake [102], and viscous vortex particle methods [103].

3.2 Tandem Rotors

The tandem rotor considered in this study has been documented in [50]. As shown in Figure 3-2, the front rotor is rotating in the counter-clockwise direction (when viewed from above the helicopter), and the rear rotor is rotating in the clockwise direction. The blades are initially placed at a 90-degree azimuthal offset as shown above. Both the rotors have an identical radius of 7.62 feet, and an identical solidity of 0.0968. L is the distance between the shaft centers, and the D is the diameter of the rotor. In the experiments, the tandem rotor configuration has no vertical offset. Two cases with overlapping and non-overlapping cases are studied. The corresponding length-to-diameter ratios for non-overlapping and the overlapping cases are 1.03 and 0.63, respectively. For the overlapping rotor case, the total disk area is reduced by 13.4%.

(a)

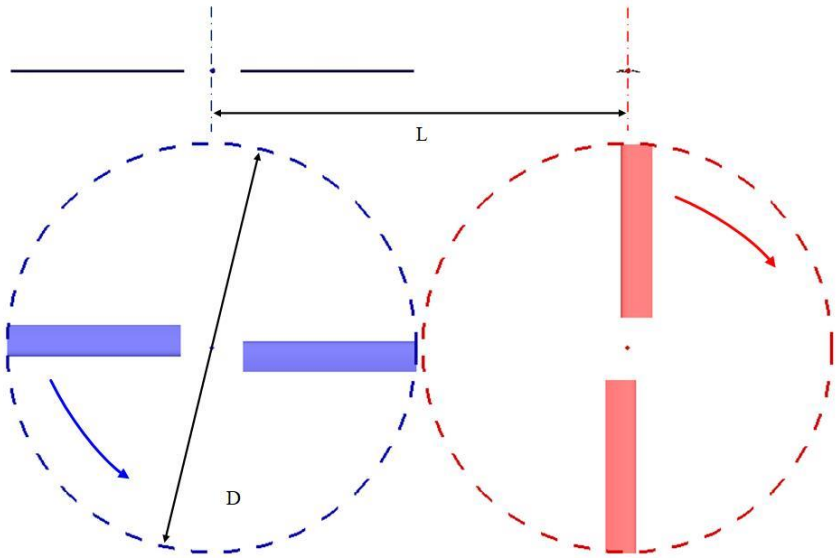

(b)

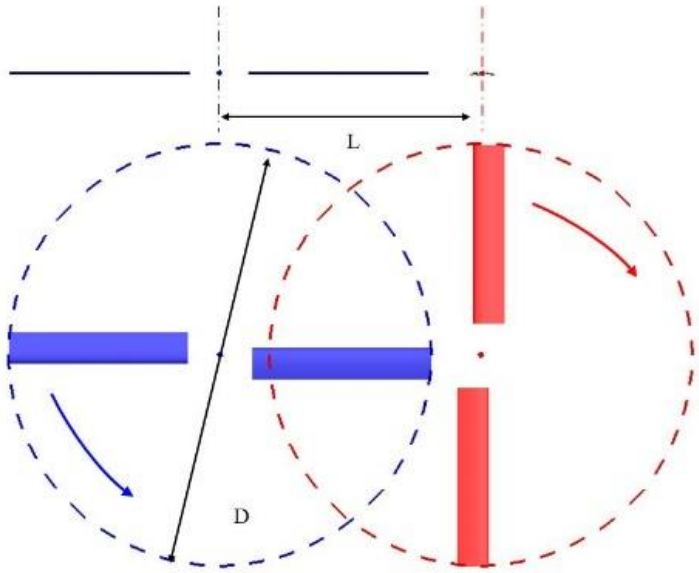

Figure 3-2 Tandem rotor configuration (a) zero overlap (b) 13.4% area overlap

3.3 Results for the Harrington Coaxial Rotor 1

3.3.1 Hover control input

For the hover condition, the collective pitch values for both the rotors are held fixed, and no cyclic pitch variations are applied. Barbely et al. trimmed the rotors for zero net torque, using the comprehensive analysis CAMRAD-II [98] for various total thrust values. There values, shown in Table 3-1 below, have been used in GT-Hybrid and RotCFD both to facilitate one-to-one comparisons between the two flow solvers.

Table 3-1 Hover control angle inputs for the Harrington rotor 1

Upper Rotor θ_0(°)	Lower Rotor θ_0(°)
1.5	1.5
3.0	3.2
5.0	5.2
7.0	7.2
8.0	8.2
9.0	9.2
10.0	10.2
11.0	11.0
11.9	12.0

3.3.2 Hover performance

Figure 3-3 shows GT-Hybrid hover performance predictions compared with experimental measurements for the Harrington coaxial rotor 1. These results were generated for a collective pitch range from 1° to 10°. At low thrust settings, the power consumption is primarily from the profile drag of the rotor, including the connectors that join the rotor blades to the rotor. Since these components are not modeled in GT-Hybrid, the agreement is very poor. Agreement improves at high thrust settings, where the induced power effects dominate.

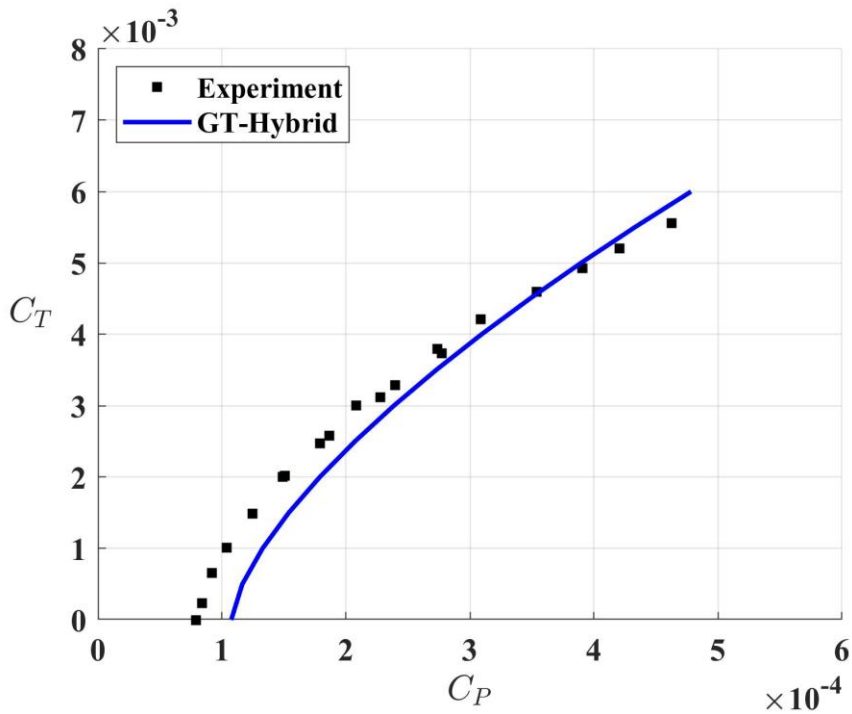

Figure 3-3 Power coefficient variation with thrust coefficient for the Harrington rotor 1 in hover

3.3.3 Hover inflow distribution

The computed inflow velocity distribution at the rotor disk was next examined. Contour plots of the induced flow over the rotor disk were extensively used to visually examine the interference effects, as shown in Figure 3-4 at a representative thrust setting of $C_T = 0.005$.

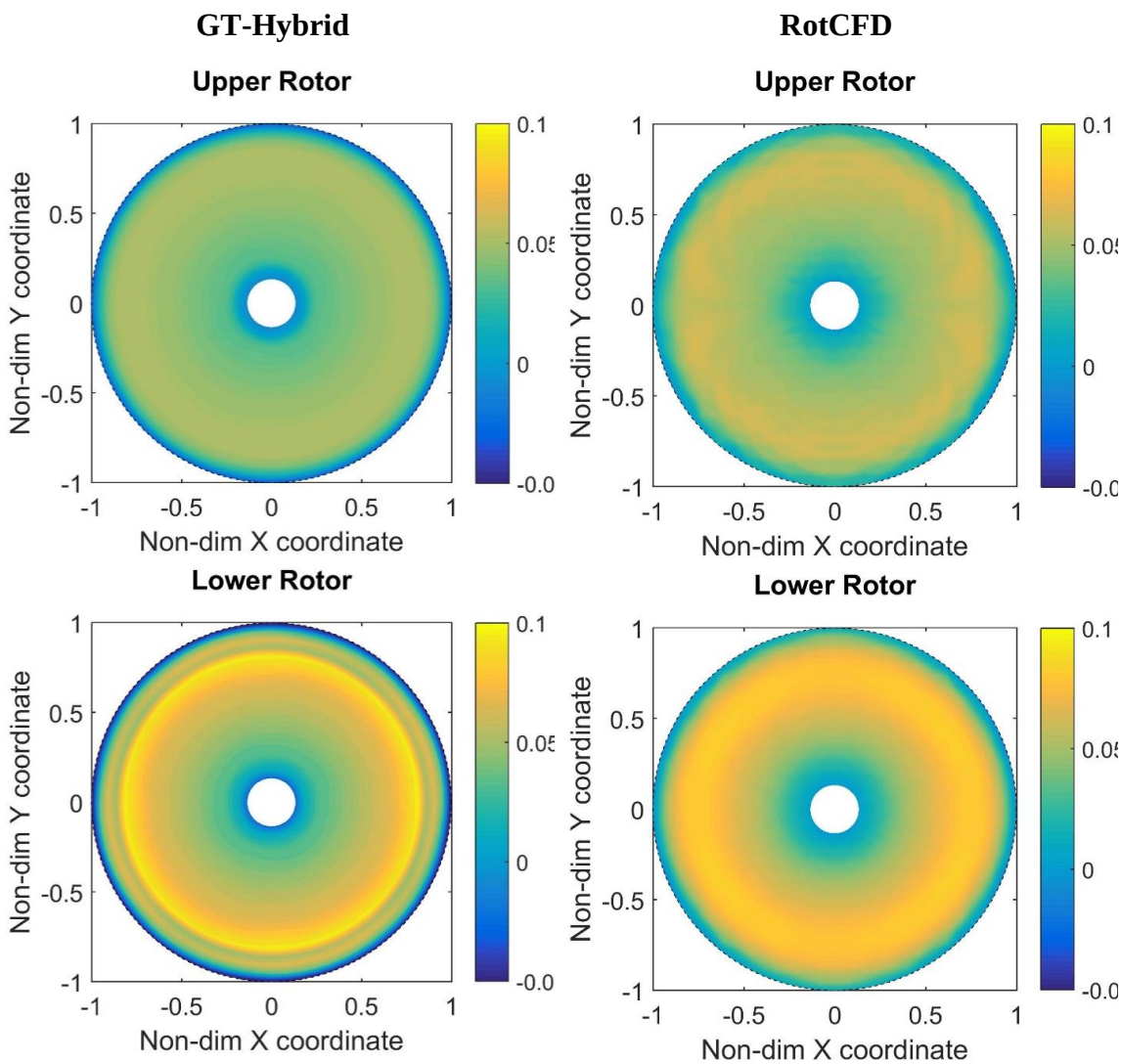

Figure 3-4 Induced velocity distribution of Harrington rotor 1 from GT-Hybrid and RotCFD

The inflow distributions for the upper rotor from the two solvers were quite comparable. For the lower rotor, GT-Hybrid indicated a steeper radial variation of the inflow. This was traced to the vortex wake from the upper rotor (which is discretely modeled using a vortex lattice) interacting with the lower rotor. RotCFD uses a wake capturing model with a somewhat diffused wake, and the radial variations were smooth.

For quantitative analyses, the values of λ_0, λ_{1c}, and λ_{1s} extracted from the inflow were used. In hover, the coefficients λ_{1c} and λ_{1s} are negligible, i.e. at least two orders of magnitude smaller than λ_0. Table 3-2 below shows the extracted data at $C_T = 0.0051$. Both solvers gave very similar estimates for λ_0 for the upper rotor (within 3% of each other). The results for λ_0 for the lower rotor were higher compared to the upper rotor as may be expected. The predictions from the two solvers are noticeably different for the lower rotor by 8%.

Table 3-2 Inflow coefficients for the Harrington rotor 1 in hover from GT-Hybrid and RotCFD for $C_T = 0.0051$

Harrington rotor 1		λ_0	λ_{1c}	λ_{1s}
Upper rotor	GT-Hybrid	0.0393	2.41e-4	-2.33e-6
	RotCFD	0.0406	-2.94e-4	1.45e-4
Lower rotor	GT-Hybrid	0.0521	4.10e-4	3.51e-6
	RotCFD	0.0567	-8.81e-5	2.60e-4

3.3.4 Forward flight inflow distribution

The forward flight calculations have been done for the Harrington Rotor 1 using both GT-Hybrid and RotCFD at range of advance ratios of 0.12 to 0.24. The shaft axis and control settings from [98] are shown in Table 3-3. Both solvers used identical settings.

Table 3-3 Forward flight control angle inputs for Harrington rotor 1

Upper Rotor

μ	$\alpha_s(°)$	$\theta_0(°)$	$\theta_{1s}(°)$	$\theta_{1c}(°)$
0.12	-2.16	8.07	-2.75	1.05
0.14	-2.85	8.08	-3.12	0.84
0.16	-3.64	8.31	-3.55	0.69
0.18	-4.51	8.69	-4.03	0.59
0.20	-5.47	9.21	-4.57	0.50
0.22	-6.46	9.87	-5.19	0.42
0.24	-7.53	10.68	-5.90	0.36

Lower Rotor

μ	$\alpha_s(°)$	$\theta_0(°)$	$\theta_{1s}(°)$	$\theta_{1c}(°)$
0.12	-2.16	7.98	-2.43	1.32
0.14	-2.85	8.03	-2.89	0.99
0.16	-3.64	8.27	-3.35	0.81
0.18	-4.51	8.67	-3.85	0.69
0.20	-5.47	9.19	-4.36	0.63
0.22	-6.46	9.85	-5.07	0.55
0.24	-7.53	10.65	-5.75	0.50

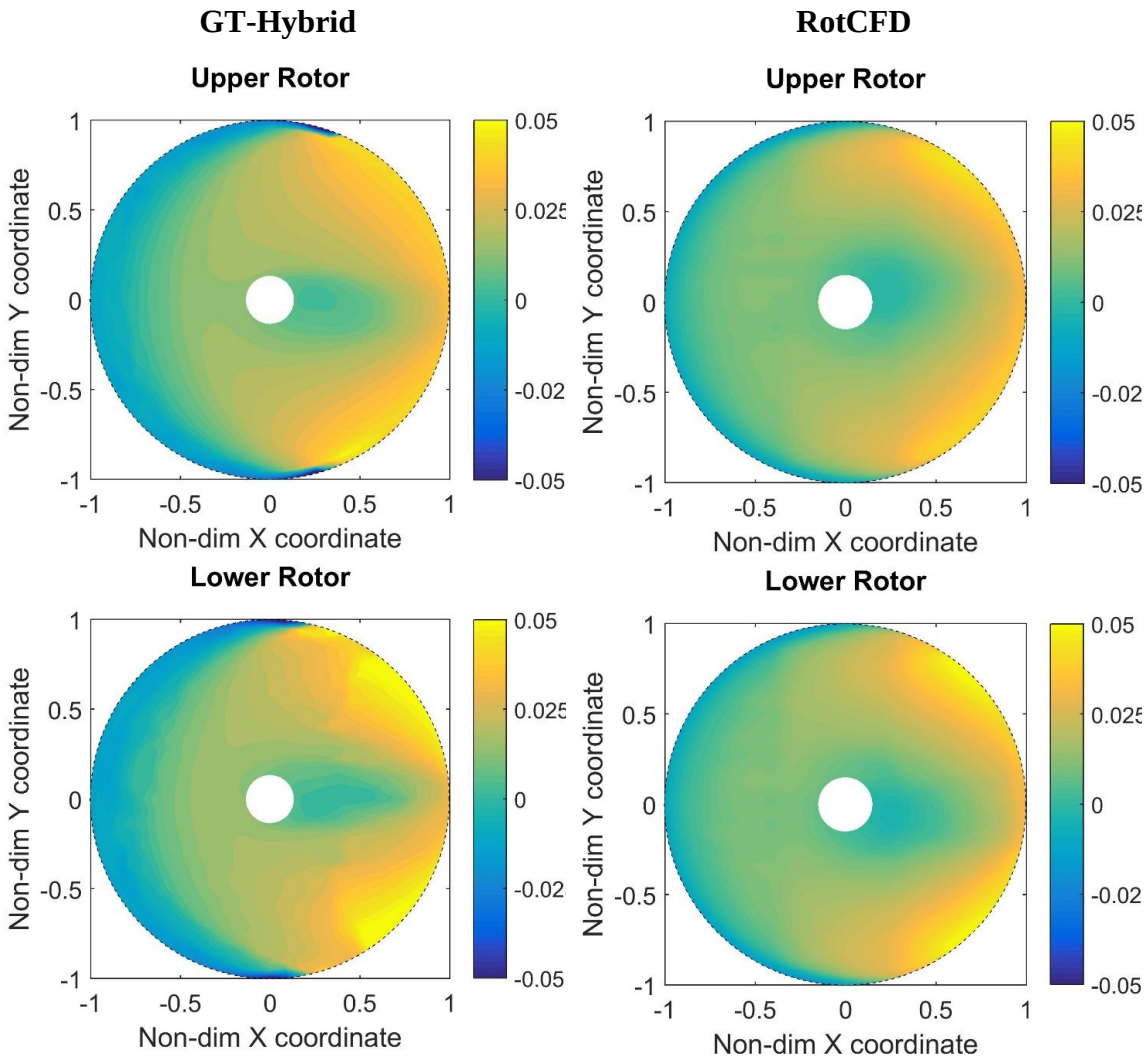

Figure 3-5 Induced velocity distribution for Harrington rotor 1 from GT-Hybrid and RotCFD at $\boldsymbol{\mu}$ = 0.14

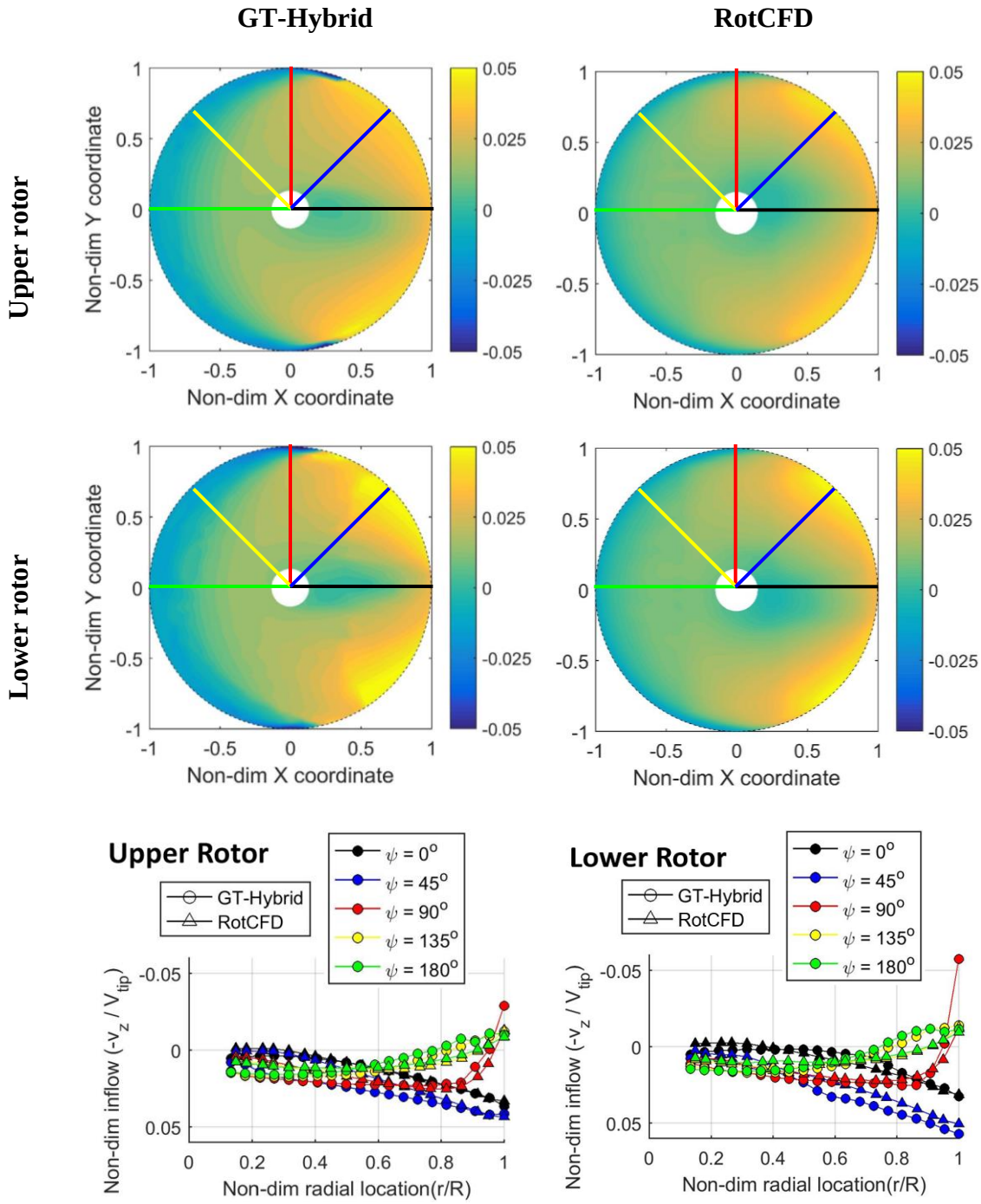

Figure 3-6 Comparison of sectional induced velocity distributions between GT-Hybrid and RotCFD for upper and lower rotors at $\boldsymbol{\mu}$ = 0.14

Figure 3-5 above shows the induced velocity fields for visual comparison between GT-Hybrid and RotCFD at μ = 0.14. Both solvers captured the downward directed induced flow through the upper and lower rotors. The lower rotor tends to have higher induced velocities near the 45-degree azimuth location as shown in Figure 3-6.

Table 3-4 shows the extracted inflow coefficients from the two solvers at μ = 0.14. The two solvers produced 3% to 6% difference in thrust at the same advance ratio. Since λ_0 behaves like $C_T^{3/2}$ this resulted in 5% to 9% variation in λ_0 between the two solvers for the upper and lower rotor both. The simulations indicate a small but finite positive value for λ_{1c}. In the front part of the rotor disk, in the tip region, a small amount of upwash is also seen as expected. The flow field is nearly symmetric in the lateral direction. Consequently, the coefficient λ_{1s} is nearly zero.

Table 3-4 Inflow coefficients for the Harrington rotor 1 in forward flight from GT-Hybrid and RotCFD

$\mu = 0.14$		λ_0	λ_{1c}	λ_{1s}
Upper rotor	GT-Hybrid	0.0154	0.0221	4.51e-4
	RotCFD	0.0148	0.0164	2.06e-4
Lower rotor	GT-Hybrid	0.0160	0.0253	3.83e-4
	RotCFD	0.0148	0.0175	2.71e-4

Figure 3-7 shows the variation of inflow distribution at several advance ratios for the Harrington rotor 1, using GT-Hybrid. As the forward flight speed increases, the wake from the upper rotor is convected downstream, and the region of the downward directed induced velocity is shifted towards the rear half of the lower disk. Figure 3-8 shows the variation of inflow coefficients with advance ratio for the Harrington rotor 1 in graphical form. It is seen that the two solvers behave in a consistent, and physically expected manner. The azimuthally averaged component of the inflow behaves like $C_T/2\mu$. As expected from the Glauert inflow model, the uniform inflow coefficient λ_0 through the upper rotor progressively decreases as advance ratio increases. Similar to upper rotor, the λ_0 of the lower rotor is found to decrease as the advance ratio increases. It is seen that the lower rotor experiences a higher inflow λ_0 relative to the upper rotor, due to wake interference effects from the upper rotor. The forward flight carries the wake aft, causing induced inflow in the rear half of the rotor disk to be higher for both the upper and lower rotors. Therefore, the longitudinal inflow coefficient λ_{1c} for both rotors also decreases with increasing advance ratio. Furthermore, the magnitude of the longitudinal inflow coefficients for lower rotor is higher because of the fore-aft asymmetry in the inflow caused by the interaction of the upper rotor wake with the lower rotor disk. The lateral variation λ_{1s} was negligibly small at all advance ratios as in hover.

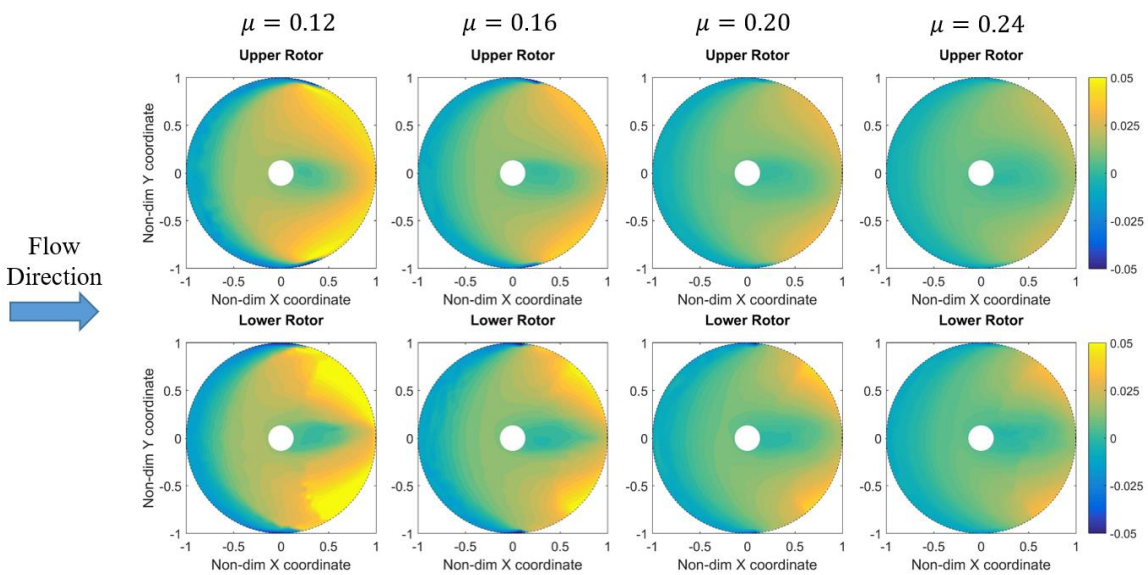

Figure 3-7 Induced velocity distribution for the Harrington rotor 1 from GT-Hybrid at $\boldsymbol{\mu}$ = 0.12, 0.16, 0.20, and 0.24

Upper Rotor

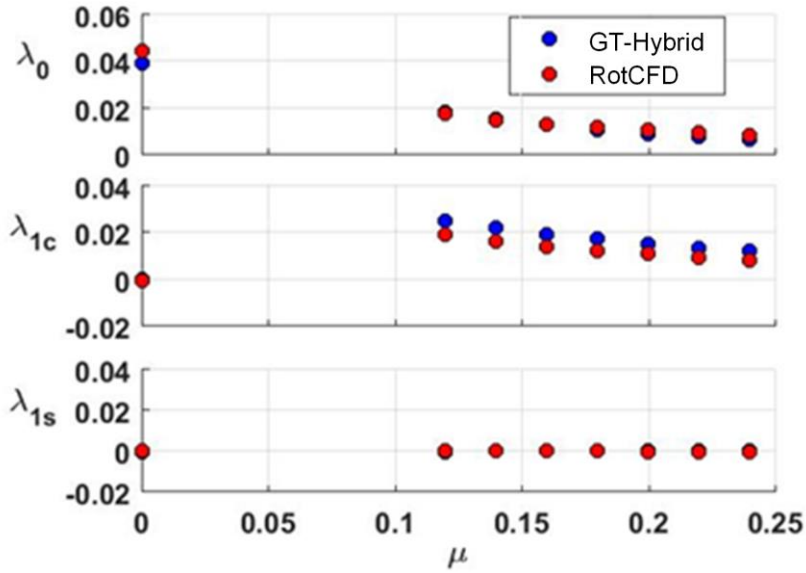

Lower Rotor

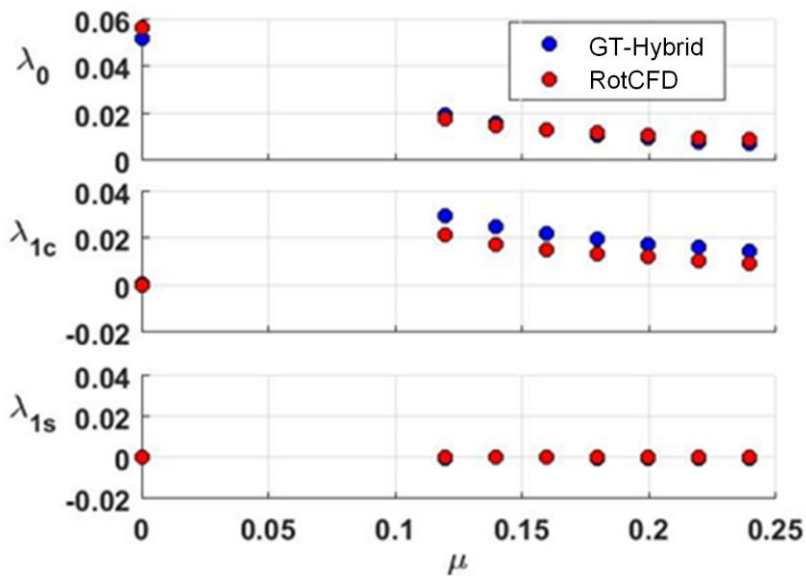

Figure 3-8 Inflow coefficients in forward flight for the Harrington rotor 1

3.4 Results for the Tandem Twin Rotor

3.4.1 Hover control inputs

For the tandem twin rotor in hover, the collective pitch values for the rotors range from 1 degree to 10 degrees in one-degree increments, to cover the thrust coefficient range reported in the experiments. The test report does not indicate whether the collective pitch values were adjusted to ensure torque balance. The control setting used in both flow solvers (GT-Hybrid and RotCFD) is identical.

3.4.2 Hover performance

The test data is available as a plot of required thrust vs. required power [50]. Reasonably good agreement between the present predictions and measurements is observed.

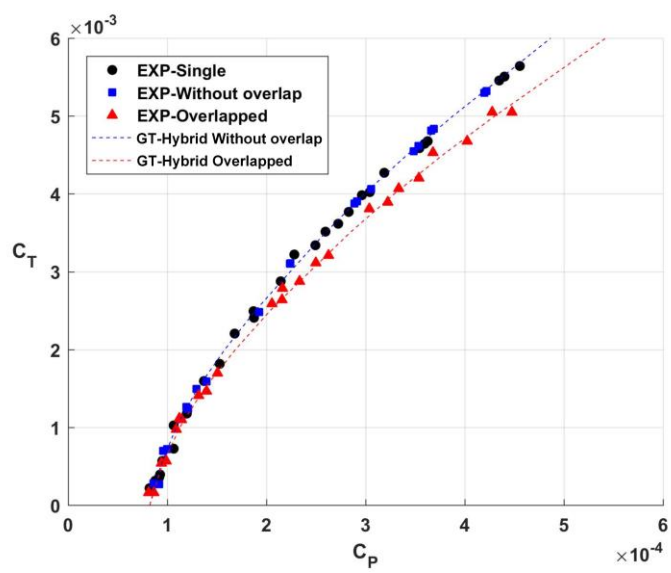

Figure 3-9 Comparison of predicted and measured power coefficient as a function of thrust coefficient

3.4.3 Hover inflow distribution

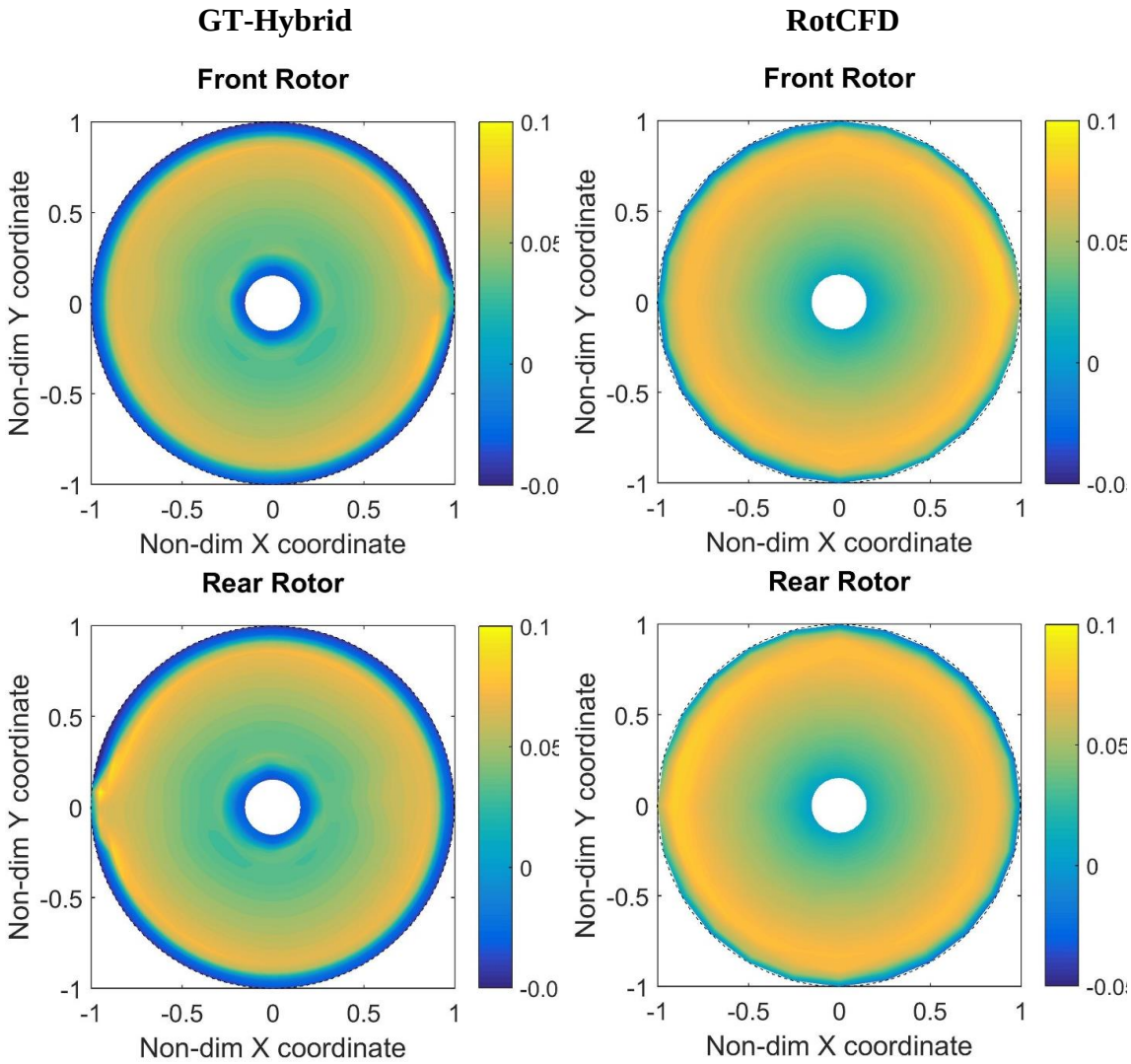

Figure 3-10 Induced velocity distribution for the no-overlap tandem rotor configuration from GT-Hybrid and RotCFD

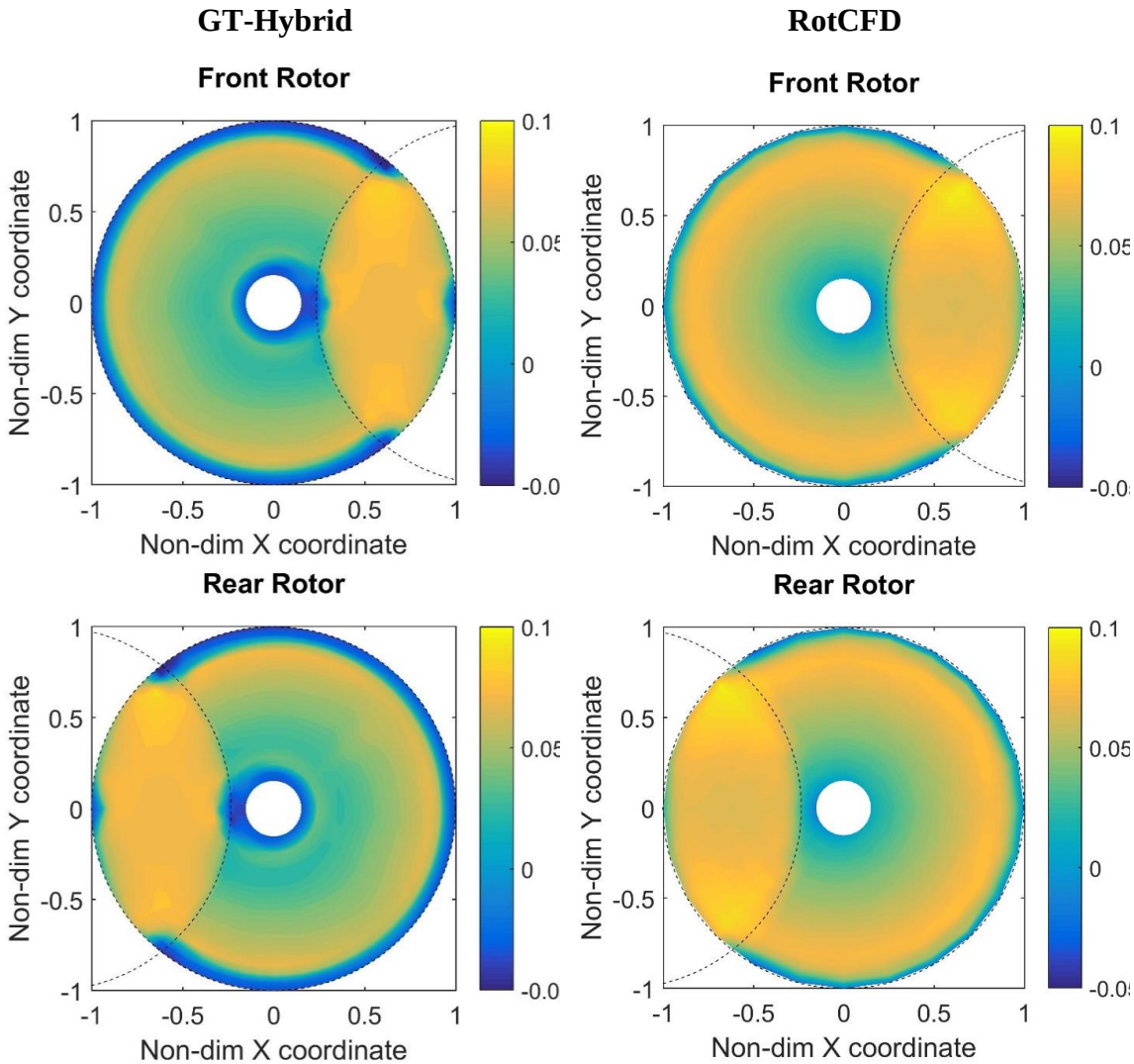

Figure 3-11 Induced velocity distribution for the overlapped tandem rotor configuration from GT-Hybrid and RotCFD

The inflow velocity distribution at the rotor disk was next examined. The flow field is unsteady with a two-per rev variation in both the airloads and the inflow. In flight dynamics simulations, time-averaged inflow distribution as well as the unsteady (or azimuthal) variation of inflow is of interest. Figure 3-10 and Figure 3-11 above show the time-averaged inflow velocity normal to the rotor disk from the two analyses. While there are radial variations in the inflow, it is seen that the inflow velocity is nearly uniform with respect to the azimuth except in the region of interference - near zero-degree azimuth for the front rotor and 180-degree azimuth for the rear rotor. Again, the radial gradients in the GT-Hybrid were somewhat sharper because of the way the wake was modeled (free wake) related to RotCFD (wake capturing).

The inflow data for the tandem rotor configurations were examined visually and quantitatively in a manner similar to the coaxial rotor. The flow field is unsteady even in hover, with a two-per rev variation in airloads and the inflow both. In flight dynamics simulations, time-averaged inflow distribution and the unsteady (or azimuthal) variation of inflow are both of interest. Table 3-5 shows the representative inflow coefficients from GT-Hybrid at a collective pitch of 8 degrees. The computed thrust coefficient was 0.0053 for the non-overlap case, and 0.0049 for the overlap case, indicating that the overlap has an adverse effect on thrust production. At the same time, the induced inflow component λ_0 increases for the overlap case relative to the non-overlap case. Thus, rotor overlap has an adverse effect on power consumption. It is also clearly seen that strong azimuthal variations are indeed present, even in hover as indicated by the non-zero components of λ_{1c} and λ_{1s}.

Table 3-5 Inflow coefficients for no-overlap and overlapped tandem rotor configurations from GT-Hybrid

No-overlap tandem rotor		λ_0	λ_{1c}	λ_{1s}
Front rotor	GT-Hybrid	0.0434	0.0027	0.0005
Rear rotor	GT-Hybrid	0.0436	-0.0020	-0.0004
Overlapped tandem rotor		λ_0	λ_{1c}	λ_{1s}
Front rotor	GT-Hybrid	0.0465	0.0188	0.0016
Rear rotor	GT-Hybrid	0.0459	-0.0172	0.0019

The tip vortex as well as the inner wake trajectories have been examined to obtain further insight into the rotor interference effects. In Figure 3-12, the tip vortex structure for a reference blade is shown at a representative time, for the non-overlap case. The solid lines in the vicinity of the rotor blade tip represent the strong tip vortex trajectory, while the lattice structure corresponds to the inner wake. It is seen that the tip vortices from the front and rear rotor both descend slowly compared to the inner wake. It is also seen that the inner wake has a linear variation in the descent rate from root to tip, so that the outer edge of the inner wake (close to the blade tip) descends faster than the inner edge close to the root. These features have been experimentally observed by Gray [104] and Landgrebe [105]. It is also seen that the tip vortices from the front and rear rotor interact with each other and pushed upwards towards the rotor disk. They may also have a cancelling effect on the upward directed induced flow outboard of the tip vortex.

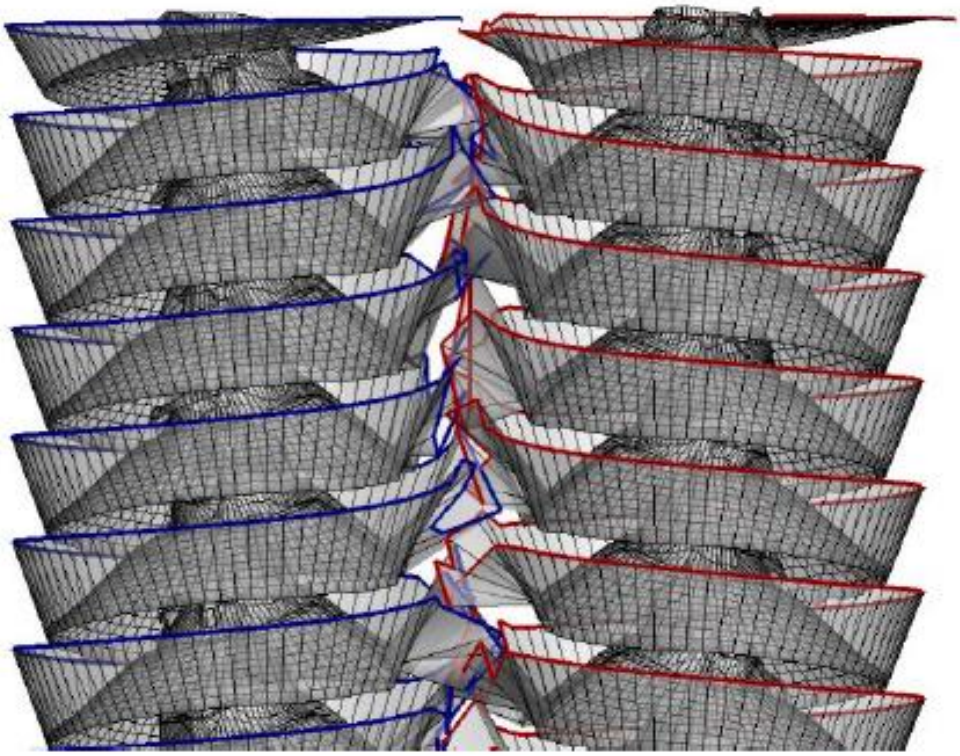

Figure 3-12 Tip vortex and inner wake structures for the non-overlapped tandem rotor configuration from GT-Hybrid

Figure 3-13 shows the tip vortex for reference blades on the front and rear rotor, and its associated inner wake for the overlap case. As expected, it is seen that there is strong interaction between the tip vortices. There are significant interactions also between the inner wake structure of the front rotor and the tip vortices from the rear rotor, and vice versa.

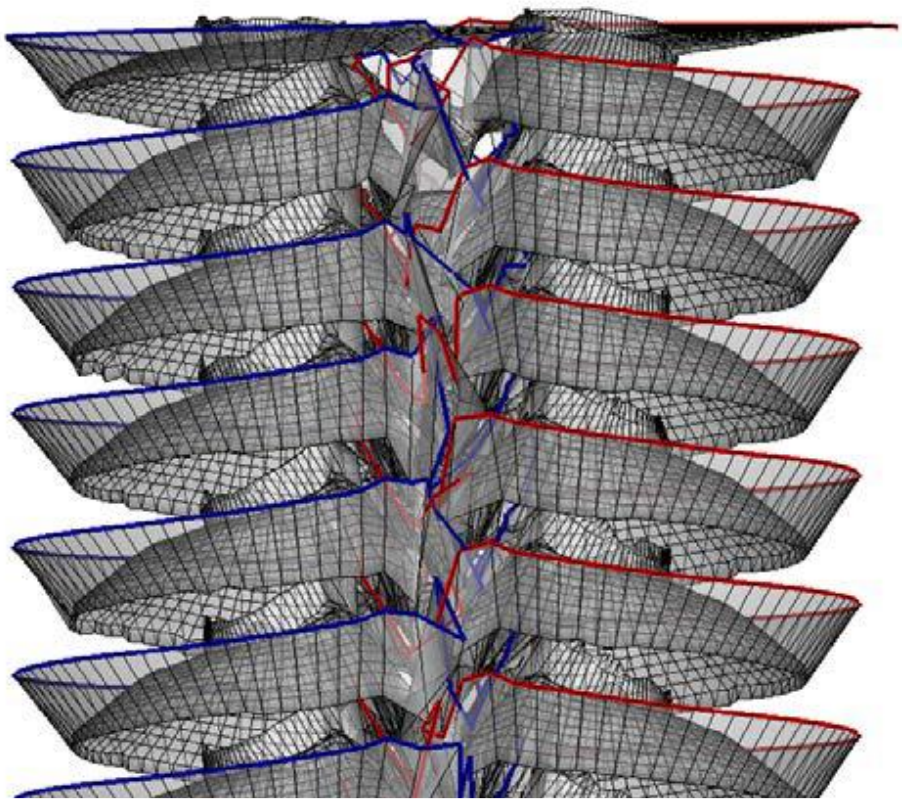

Figure 3-13 Tip vortex and inner wake structures for the overlapping tandem rotor configuration from GT-Hybrid

CHAPTER 4. Low Reynolds Number Multi-Rotor Simulations

In the previous chapter the aerodynamic phenomena associated with coaxial and tandem rotors with interacting wake structures were considered. The rotor diameters for these configurations are large, representative of a full-scale helicopter. Thus, the experimental studies and the computational studies directed at these large configurations, including the present numerical work, are of great interest to the helicopter industry and the research community.

As discussed in the previous chapter, there has been a large body of work on wake characteristics and inflow flow field characteristics of large-scale rotors. Experimental and computational data are available for single and coaxial rotors, and for tandem rotor configurations. Results are available for rotor performance in hover and forward flight, spanwise and azimuthal blade loading, and wake structures. These results are being used to improve dynamic inflow models and comprehensive aeroelastic analyses.

A similar set of data is not available for small scale rotors that are in use in drones and other autonomous systems [106-112]. The small rotor radius, combined with small chord, imply low Reynolds numbers. The aerodynamic characteristics of the blade sections at such Reynolds numbers differ significantly from conventional rotors at higher Reynolds numbers. Both the static and dynamic stall characteristics are widely different. The wake trajectories are also different both due to the increased diffusion at lower Reynolds numbers and the differences in the descent and contraction rates compared to large scale rotors.

Interaction between closely spaced rotors in coaxial, tandem, or quadrotor configurations cause further complications. Work is urgently needed to characterize these effects through complementary experimental and computational studies, in order to develop reliable inflow models for use in flight dynamics simulations.

The present work is motivated by this need for developing a good understanding of the inflow characteristics of multirotor configurations. The following approach is used:

1. Extensive use is made of the data from a series of experimental studies performed at Georgia Institute of Technology for coaxial and tandem rotor configurations at low Reynolds numbers in hover. Detailed measurements of the inflow velocity field and visualization of the wake structures are used.

2. The First three components of the dynamic inflow velocity (mean flow, longitudinal, and lateral variations) are extracted to assess how the spacing between adjacent rotors and the differences in Reynolds number (between large and small-scale rotors) affect the inflow.

4.1 Rotor Configuration

The data used in this study are from hover experiments conducted by Professor Narayanan Komerath and his coworkers in the 2.13m × 2.74m (7 ft × 9 ft) test section of the John Harper closed circuit low speed wind tunnel at the Georgia Institute of Technology [59-63]. The upper rotor was suspended from the ceiling and the lower rotor was supported from the floor such that the rotors are approximately 1.5 meters above the floor. The support rods were in-line with the rotor axes to avoid their interaction with the rotor inflow and wake. Figure 4-1 shows the experimental set-up, for the coaxial case.

A two bladed untwisted rotor with a rectangular planform, made of NACA 0010 airfoil sections, has been studied in the present work. The rotor characteristics are given below in Table 4-1, and the arrangement of the rotors is shown in Figure 4-2. The horizontal and vertical spacing between the two rotors could be changed to study a wide range of rotor configurations of interest. Table 4-2 below gives details of the configurations that have been analyzed experimentally and computationally. The coaxial rotor configurations are studied with two vertical spacings of 0.25R and 0.40R. The side-by-side rotor configurations are studied with four values of axial spacing: 2.1R, 2.2R, 2.3R, and 2.4R. The tandem rotor configurations are studied for any combination of the two vertical spacing of 0.25R and 0.4R and the following axial spacing: 0.25R, 0.5R, 0.75R, 1.0R, 1.25R, 1.5R.

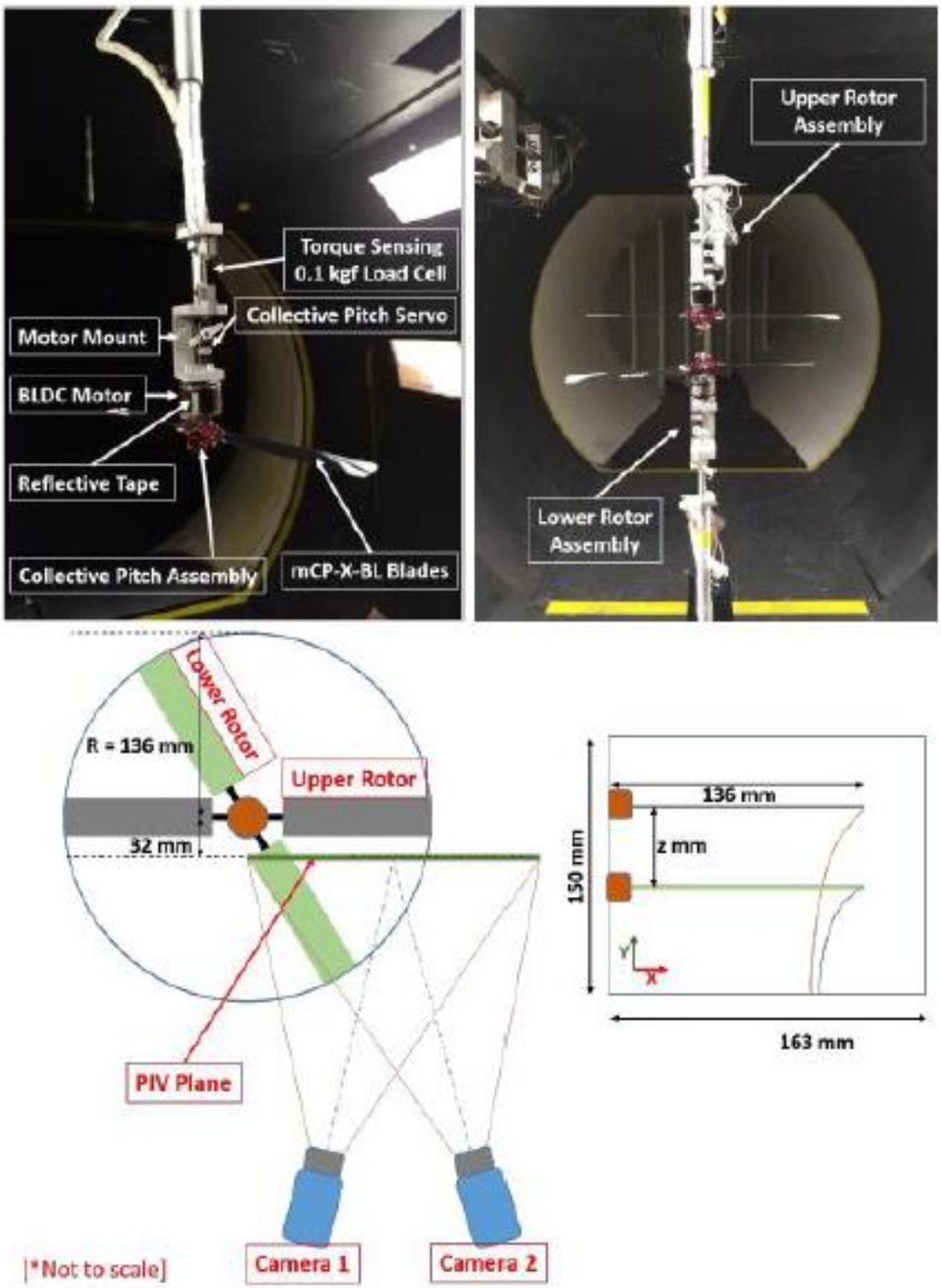

Figure 4-1 Georgia Tech experimental set-up for the coaxial rotor [62]

Table 4-1 Georgia Tech rotor geometry characteristics

Number of rotors, b	2
Number of blades	2 blades per rotor
Chord length, c	0.019m (0.062 ft.)
Rotor radius (R)	0.136m (0.446 ft.)
Solidity bc/(πR)	0.0890
Root cutout radius	0.021m (0.069 ft.)
Tip speed	61.5 m/s (201.8 ft./s)
Tip Reynolds Number	80,000

Table 4-2 Rotor spacing details

Rotor Configuration	Axial Spacing (AS)	Vertical Spacing (VS)
Coaxial Rotor	0	0.25R/0.40R
Side-by-Side Rotor	2.1R/2.2R/2.3R/2.4R/2.5R	0
Tandem Rotor	0.25R/0.5R/0.75R/1.0R/1.25R/1.5R/2.0R	0.25R/0.40R

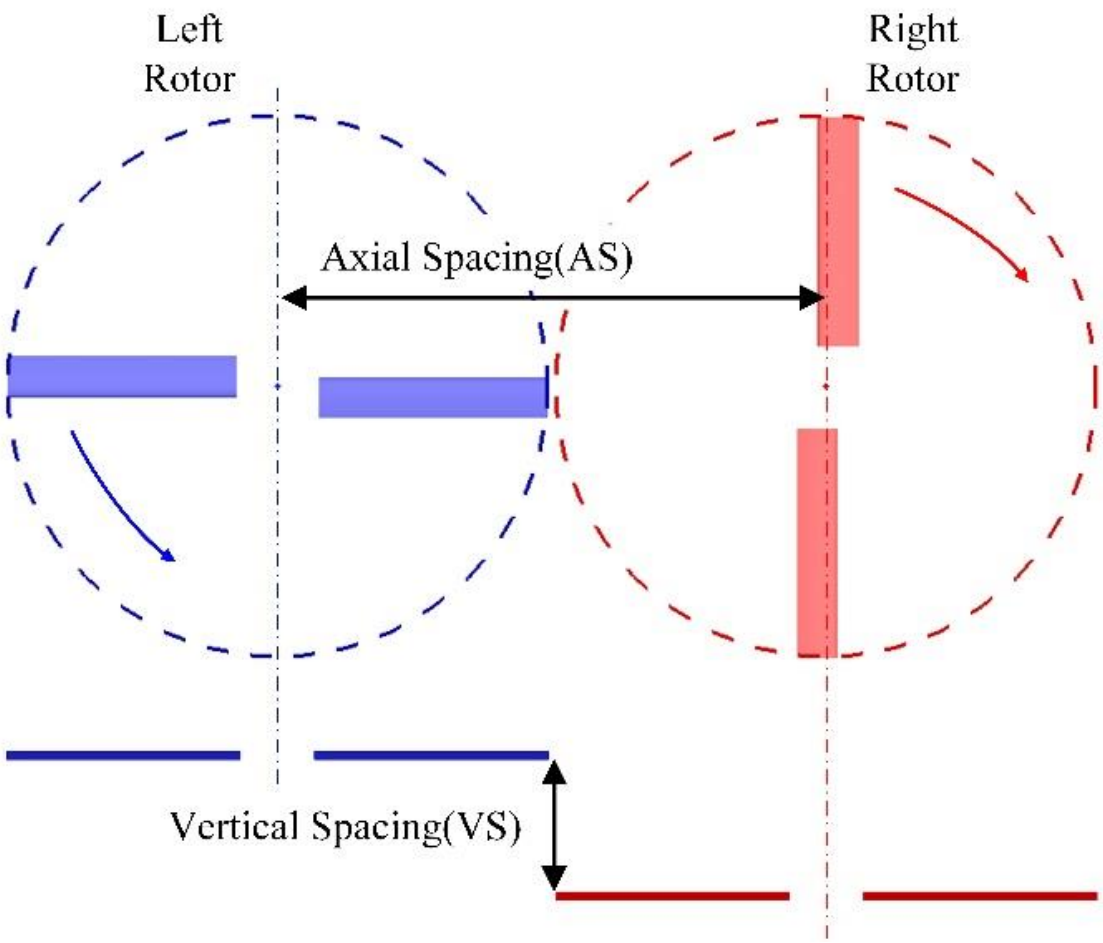

Figure 4-2 Low Reynolds number multi-rotor configuration

The rotors were powered by brushless DC motors (BLDC). The upper rotor rotates counterclockwise and the lower rotor clockwise. The collective pitch on both rotors could be adjusted independently during the test runs through variable pitch assemblies actuated using servos. The rotor speeds were monitored and controlled within +/- 10 RPM of the set values using laser tachometers and a microcontroller that employs a proportional feedback loop control. The thrust and torque generated by the rotors were measured independently using load cells.

For the torque measurements, the motor mounts were mounted on the support rods through friction-less bearings. The rotation about the bearings is restricted by 0.1 kgf range load cells placed off-center such that the counter torque necessary to keep the motor mount from rotating about the bearing due to aerodynamic torque was provided through them. Thrust was measured using 1kgf range load cell placed along the rotor axis.

Signals of all the load cells were passed through low-pass filters set at 40 Hz and amplified before reading them using data acquisition device (DAQ). The thrust and the torque data have been collected at the rate of 1000 Hz for a span of 60 seconds and then averaged. Figure 1 shows the setup for a typical coaxial rotor configuration.

High-speed stereo particle image velocimetry (SPIV) has been used to quantify the inflow velocity distributions and for tracking the streamlines through the rotors. SPIV captured the flow field on a vertical plane in the region between the two rotors.

The control setting used in the simulations are listed in Table 4-3. These values are directly obtained from the experimental settings. The collective pitch was held fixed, and no cyclic pitch variations were applied.

Table 4-3 Control settings for multi-rotor configurations

Coaxial Rotor		Upper Rotor $\theta_0(°)$	Lower Rotor $\theta_0(°)$
VS0.25R/VS0.40R		6.7455	9.0792
Side-by-Side Rotor		**Left Rotor $\theta_0(°)$**	**Right Rotor $\theta_0(°)$**
AS2.1R		6.8598	7.5388
AS2.2R		6.7455	7.4286
AS2.3R		6.4606	7.1509
AS2.4R		6.7455	7.4286
AS2.5R		6.7455	7.4286
Tandem Rotor		**Left Rotor $\theta_0(°)$**	**Right Rotor $\theta_0(°)$**
VS0.25R	AS0.25R	7.4353	9.6673
	AS0.5R	6.8598	8.6313
	AS0.75R	7.2043	8.6313
	AS1.0R	6.7455	8.2479
	AS1.25R	6.8598	8.4116
	AS1.5R	6.4037	8.0846
	AS2.0R	6.1768	7.5388
VS0.40R	AS0.25R	7.0318	9.0792
	AS0.5R	6.7455	8.5212
	AS0.75R	6.7455	8.0846
	AS1.0R	7.0318	7.9758
	AS1.25R	6.4606	7.9758
	AS1.5R	6.1768	7.5388
	AS2.0R	6.2902	7.5388

4.2 Inflow Distribution Results

The available test data included rotor performance (thrust vs. power), tip vortex trajectories, and PIV data (time averaged over a fixed plane shown in Figure 4-1). The primary focus of the computational studies is the development of inflow models that may be used in helicopter and UAV/drone flight dynamics simulations. For this reason, all of the comparisons in this section are limited to velocity field comparisons.

All the simulations in this study were analyzed after 10 rotor revolutions to eliminate impulsive start effects. The wake generated by each rotor blade is modeled with 15 trailers and resolved for 15 revolutions of wake age. Because the bound circulation over the rotor varies with time, shed wake filaments are generated once every 5 degrees of azimuth.

4.2.1 Coaxial rotor simulations

The coaxial rotor studies reported here were done at a thrust coefficient of 0.004 per rotor (0.008 for the entire coaxial system). Figure 4-3 shows the rotor inflow for the coaxial rotor at a vertical spacing of 0.25 R. The inflow and outflow data presented here are extracted at a distance 0.1 R above and below the rotors respectively for both the rotors.

The hi-speed PIV was performed on a plane 32 mm offset from the rotor centre to avoid motor mount shadows. Given that the rotor wake is symmetric in hover, data was collected only over the right half of the rotor setup as shown in Figure 4-1 above. In this study, comparisons are done against test data at the PIV plane for the reference blade (for the coaxial rotors, and tandem rotors, both).

As seen in Figure 4-3, the velocity field above the upper rotor is smooth as expected. The comparisons between the test data and the simulations are in very good agreement. At an axial location just below the upper rotor, the outflow (axial) velocity distribution linearly varies from the root cut-out to 80%R. The hybrid method used in this study predicted a more rapid contraction of the tip vortex structure from the upper rotor compared to test data. The velocity gradient outboard of the tip vortex trajectory was captured in magnitude and slope, although there was 0.05 R difference in the tip vortex trajectory radial position passing through the measurement plane. This difference is likely due to the vortex line representation of the tip vortex and inner wake, with an assumed vortex core. Small changes to these parameters can dramatically change the velocity field in the immediate vicinity of the strong tip vortex structure, influencing its radial contraction and axial descent rate, both.

The predicted inflow through the lower rotor at the PIV plane compares well with the measurements, except in the immediate vicinity of the tip vortex passage. The outflow below the lower rotor was under predicted in the calculations compared to test data, although other features such as the velocity jumps near the tip vortices from the top and bottom rotors were reasonably well resolved.

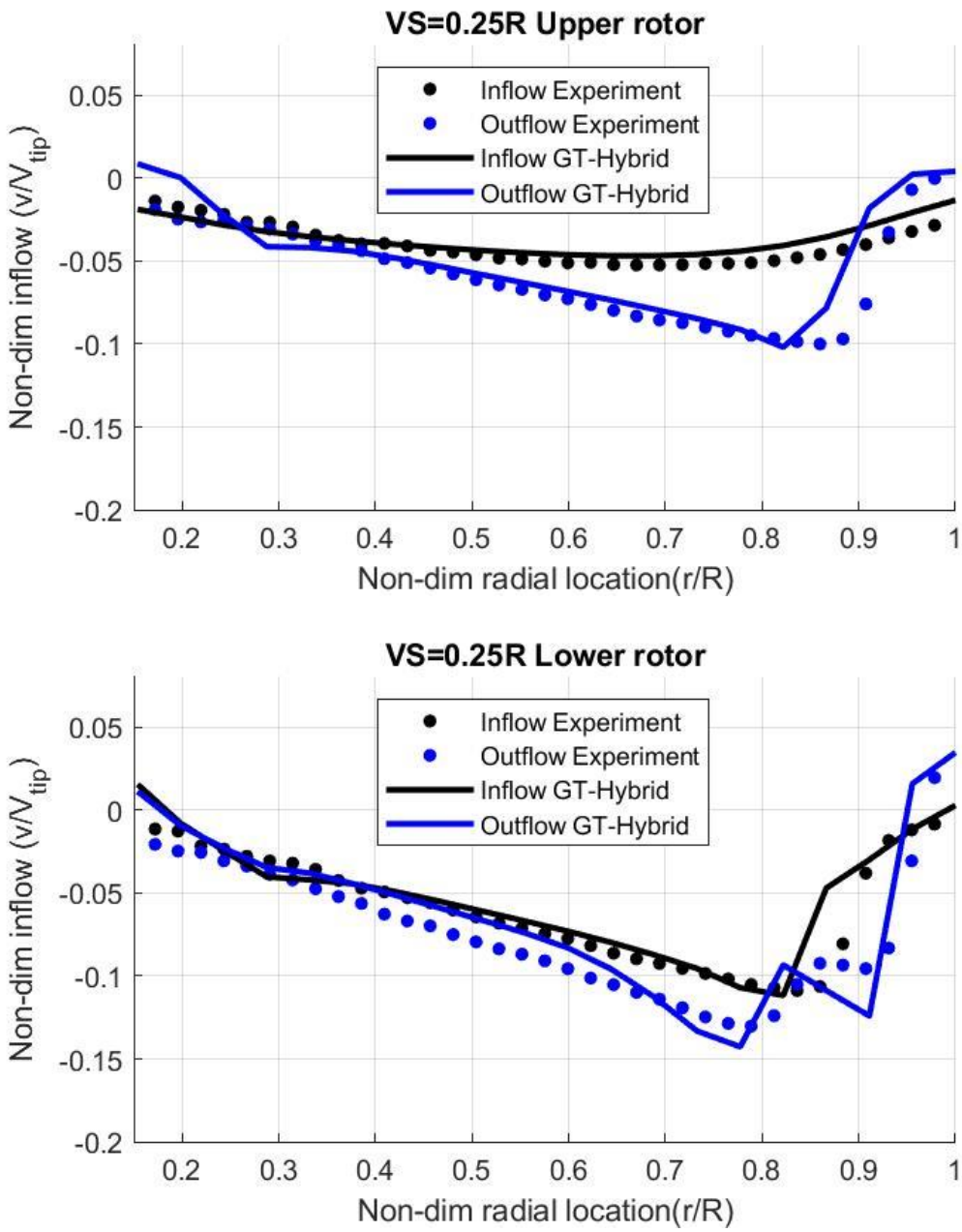

Figure 4-3 Inflow and outflow velocity profiles comparison for the coaxial rotor (with a vertical spacing of 0.25R)

4.2.2 Georgia Tech side-by-side rotor

This case is of greater interest, since many drone configurations are compact, and the rotors are placed very close to each other. Again, the thrust coefficient per rotor was trimmed to 0.004 in the experiments. The measured collective pitch was used to perform the simulations.

In Figure 4-4 and Figure 4-5, the inflow and outflow velocity fields are shown for four representative axial spacing, ranging from 2.1R to 2.4 R. The test data is not available after r/R over 1.6, due to the size limitation of the PIV measurement plane. The comparisons between the test data and measurement are very good.

The inflow and outflow profile plots in Figure 4-4 and Figure 4-5 contain some common features. The induced velocity profiles underneath both rotors are wedge-shaped with a linear increase in the magnitude of velocity from hub to tip, before dropping back to zero steeply just before the tip. Such a linear variation is common for simple untwisted rotors of rectangular planform. The peak in the induced velocity profile consistently occurs near 90%R.

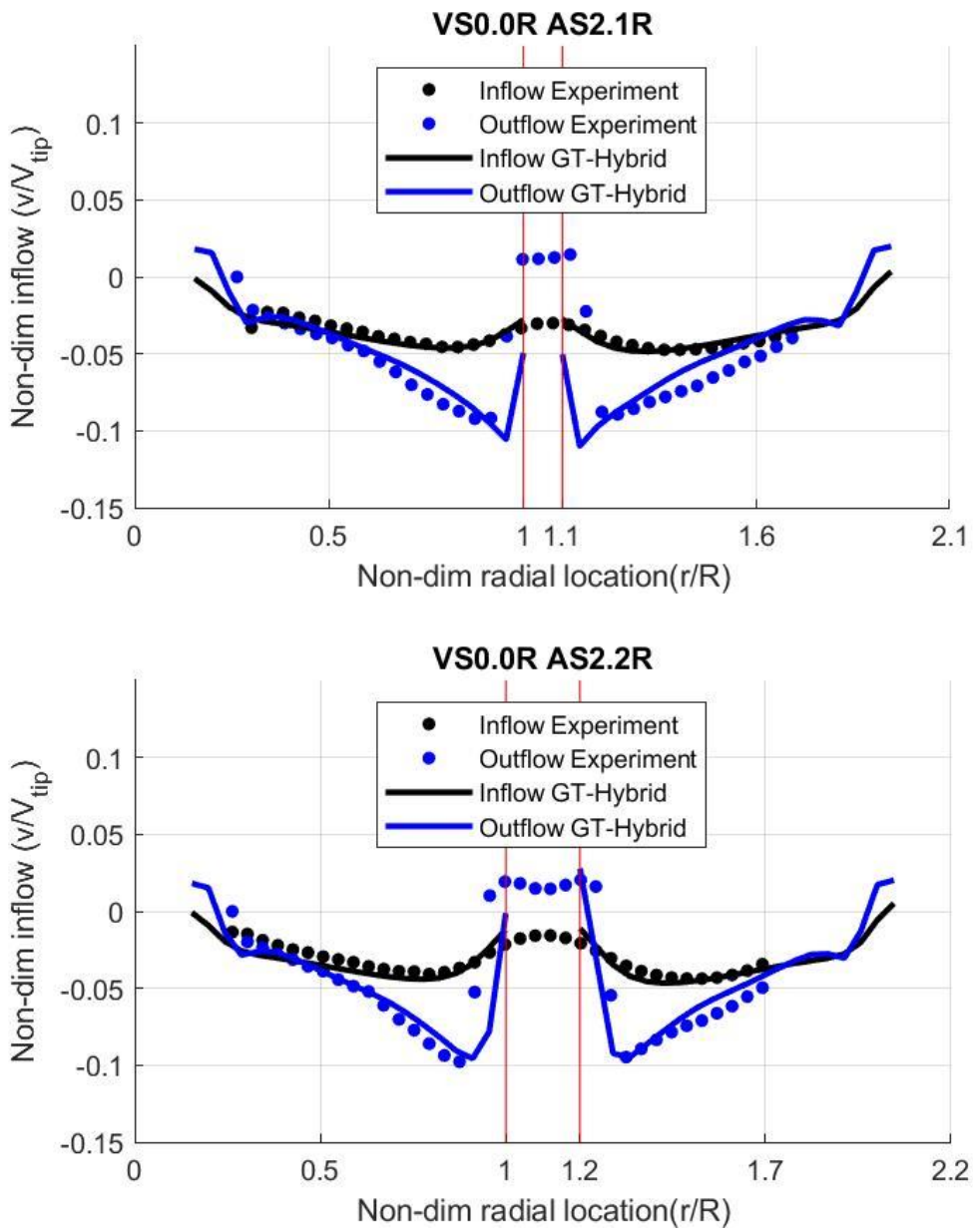

Figure 4-4 Inflow and outflow velocity profiles comparison for the side-by-side rotor (with an axial spacing of 2.1R and 2.2R)

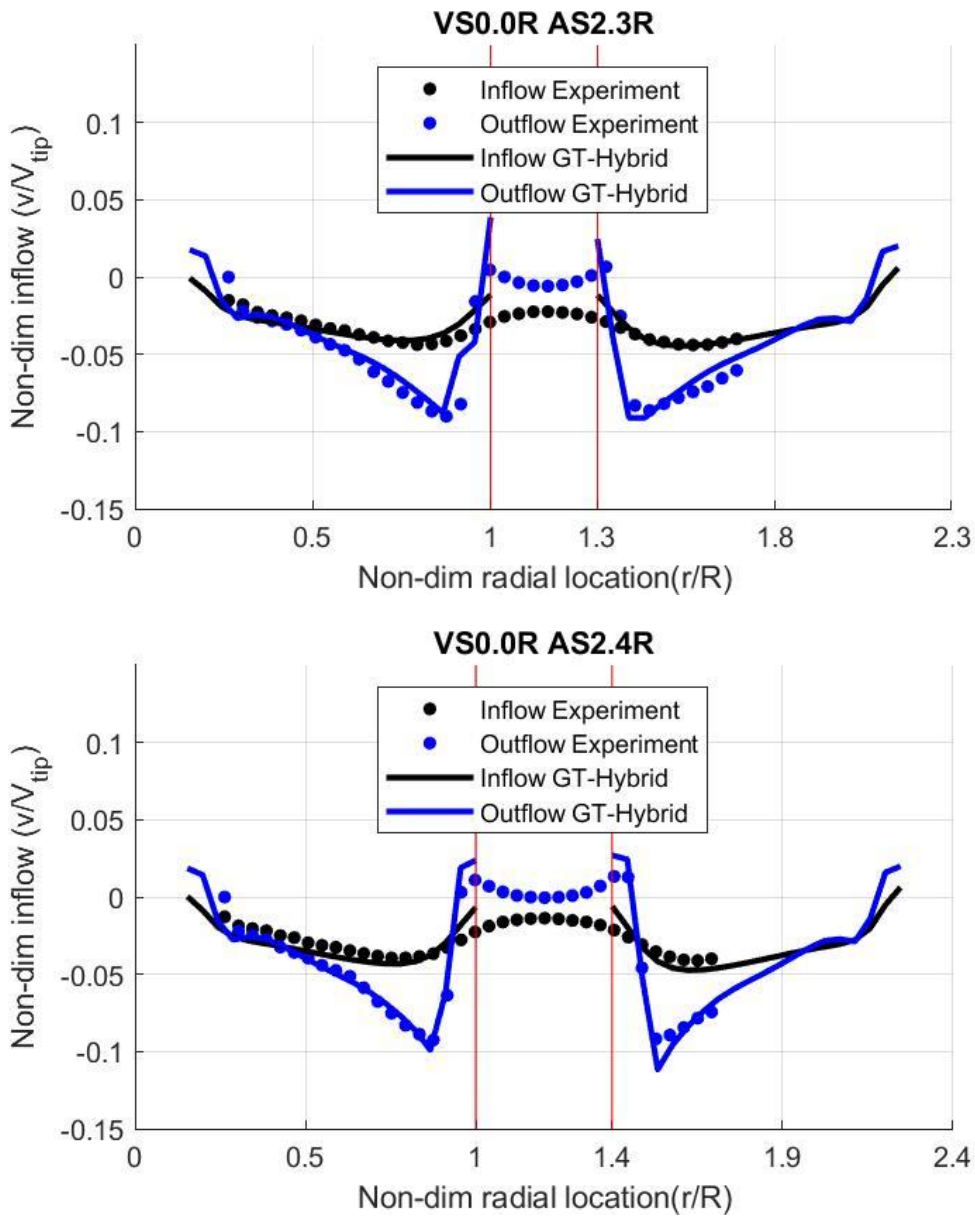

Figure 4-5 Inflow and outflow velocity profiles comparison for the side-by-side rotor (with an axial spacing of 2.3R and 2.4R)

4.2.3 Georgia Tech tandem rotor

The tandem rotor PIV and performance data were collected at two vertical spacing, and a range of axis spacing. The total thrust coefficient C_T of the two-rotor setup was kept constant at 0.008 for all cases. The rotors were trimmed in the experiments until the total target thrust was met and the rotor torques equalized. The calculations directly used the collective pitch sittings from the experiment, without additional trim.

In the experiments, the time-averaged flow fields were computed using 200 instantaneous PIV frames. The average velocity fields were found to be within 2% of those obtained using 150 frames and within 0.5% of those obtained using 175 frames for all cases.

Figure 4-6 and Figure 4-7 show comparisons of the computations with time averaged PIV data. The agreement is very good except in the immediate vicinity of the vortex blade interactions. The inflow and outflow data presented here are extracted from a distance of 0.1R above and below the rotors, respectively, for both rotors.

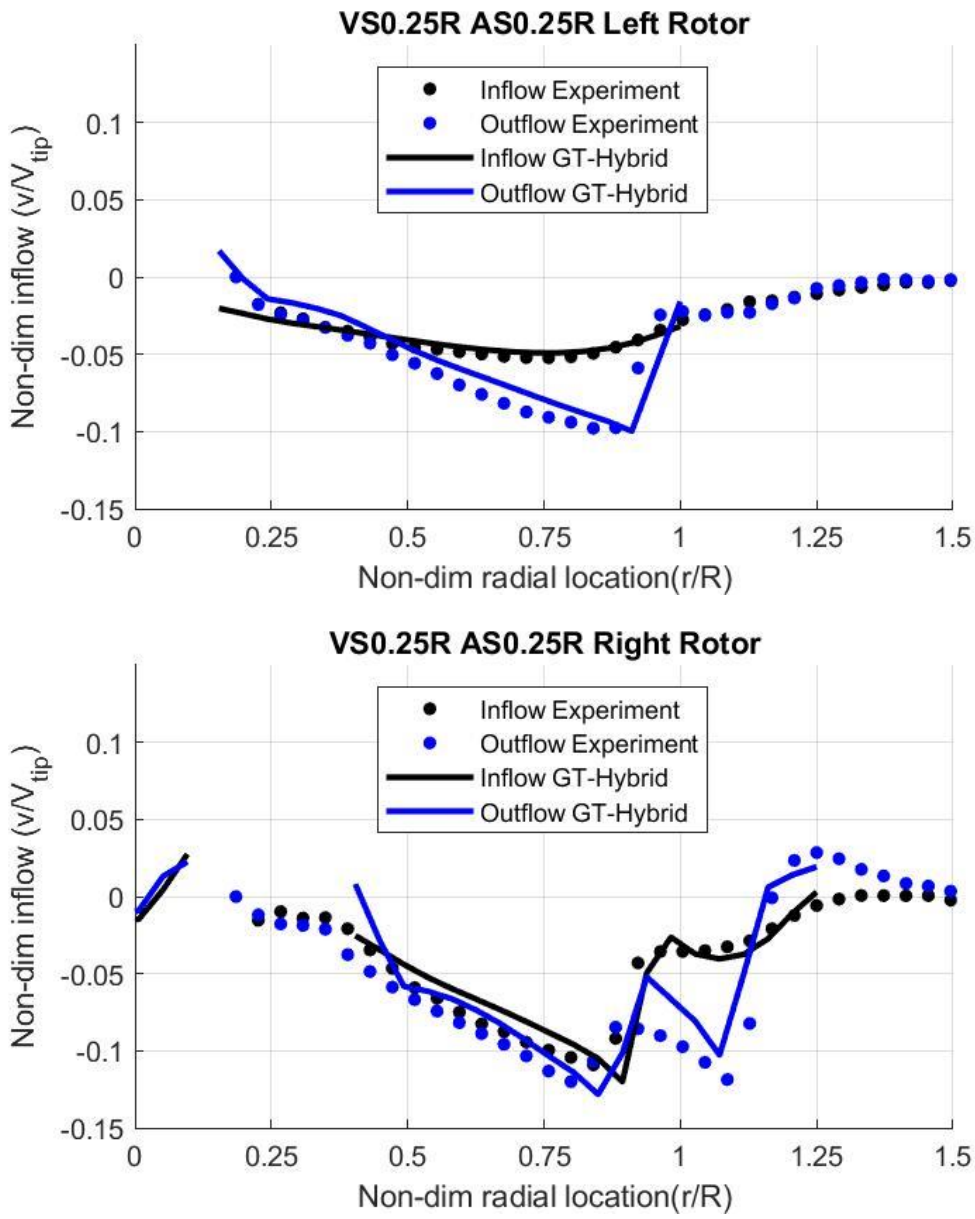

Figure 4-6 Inflow and outflow velocity profiles comparison for the tandem rotor with VS=0.25R AS=0.25R

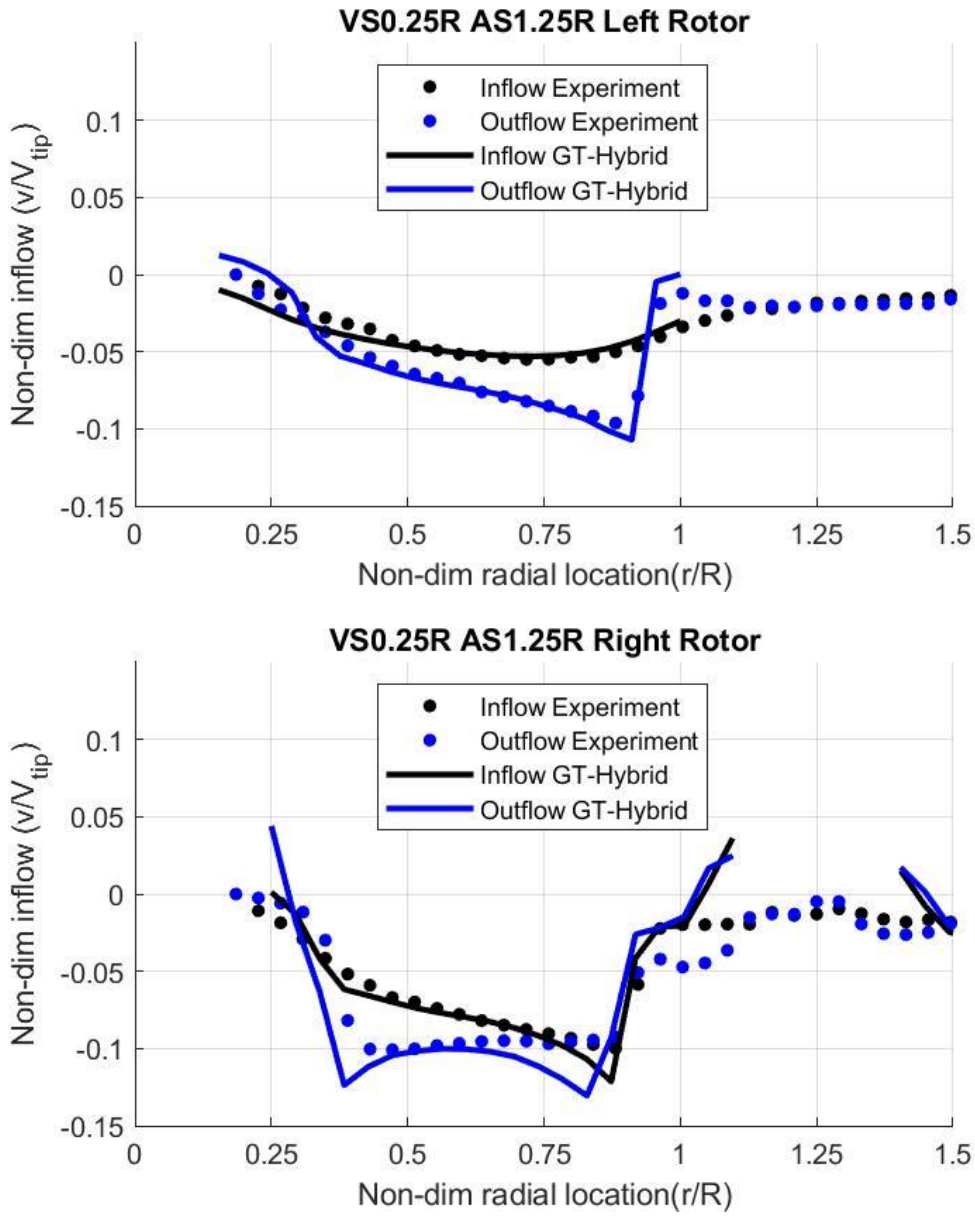

Figure 4-7 Inflow and outflow velocity profiles comparison for the tandem rotor with VS=0.25R AS=1.25R

VS=0.25R AS=0.25R **VS=0.25R AS=1.25R**

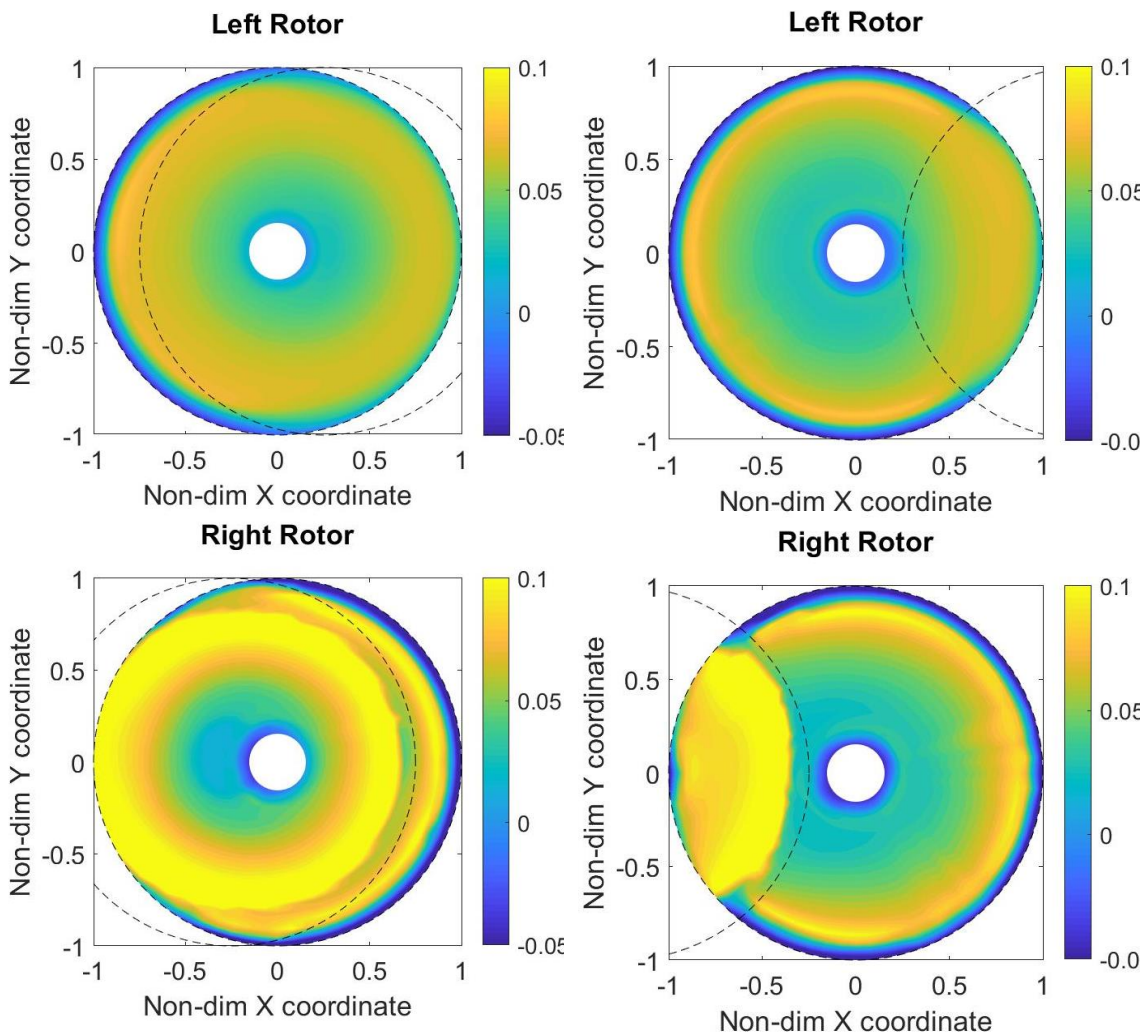

Figure 4-8 Induced velocity distribution at the rotor disk for the tandem rotor VS=0.25R AS=0.25R (left) and VS=0.25R AS=1.25R (right)

The numerical calculations give velocity field over the over the entire rotor disk as shown in Figure 4-8. It is seen that the inflow distribution is highly three dimensional and unsteady.

4.3 Extraction of Inflow Coefficients

The CFD simulations shown in the previous sections are functions of non-dimensional radial ($\vec{r}$) and azimuthal locations (ψ). They are not directly useful in flight simulations, which rely on efficient dynamic inflow models for rapid, real-time simulations. For this reason, the inflow field was post-processed to obtain the inflow coefficients as discussed in Chapter 2.

Figure 4-9 show the extracted λ_0, λ_{1c} and λ_{1s} as a function of the axial spacing, at a vertical spacing VS of 0.25R. For the left rotor, it is seen that the time averaged quantity λ_0 is nearly independent of the axial spacing. For the right rotor, λ_0 initially varies rapidly with the axial spacing due to the interaction of the left rotor wake with the right rotor disk. As the axial separation increases beyond 0.5R, λ_0 becomes less sensitive to axial separation. As may be expected, the rotor on the right, which operates partially in the outflow of the left rotor experiences a higher λ_0. This, in practice, would translate into higher induced power consumption for the right rotor compared to the left. It is also seen that λ_{1s} is nearly zero, indicating that inflow through the left and right rotors experiences very little lateral asymmetry for all the cases considered. As may be expected, there is significant fore and aft asymmetry, and λ_{1c} is nonzero. The aft rotor experiences an upward directed induced flow (upwash) rather than a downwash due to the interaction of the tip vortices from the left rotor interacting with the right rotor.

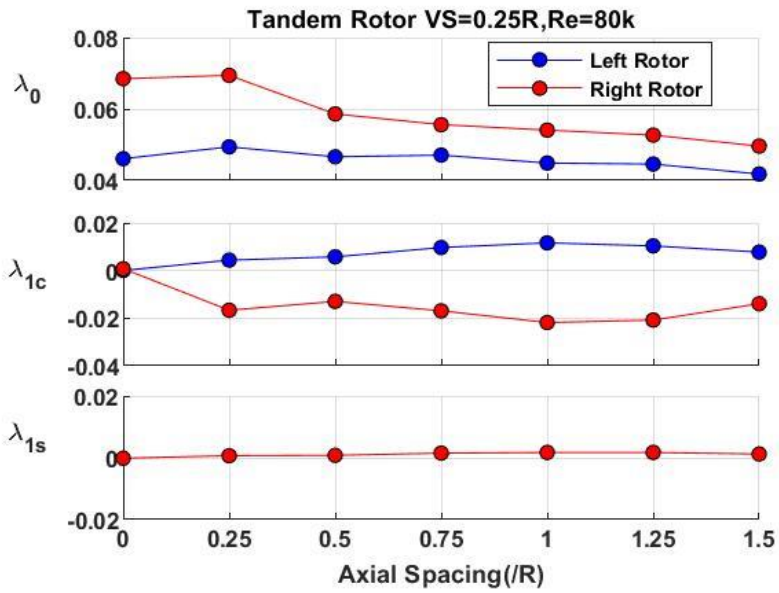

Figure 4-9 Inflow coefficients variation with axial spacing for the tandem rotor VS=0.25R

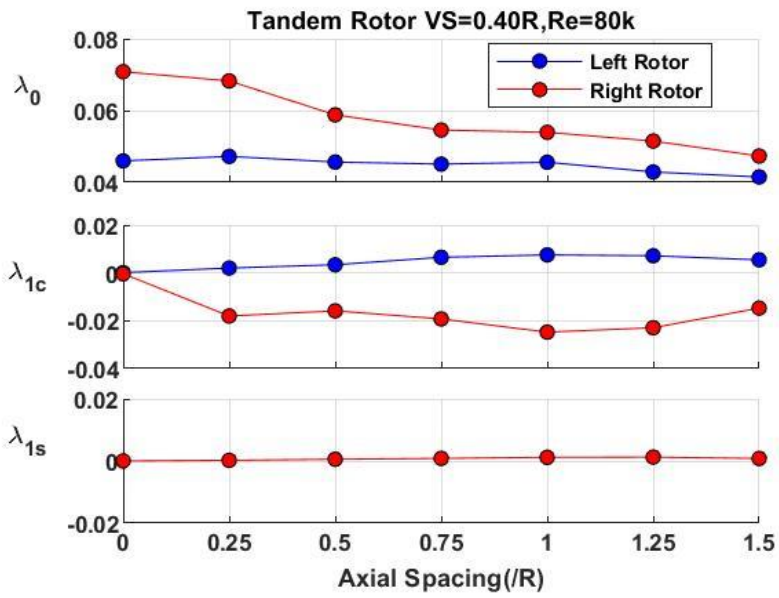

Figure 4-10 Inflow coefficients variation with axial spacing for the tandem rotor VS=0.40R

CHAPTER 5. Conclusions and Recommendations

A physics-based model for modeling helicopter and UAV rotor configurations, previously developed for isolated rotors and coaxial rotors in hover and forward flight has been extended to more general multi-rotor configurations. Simulations for coaxial, and tandem rotor configurations have been done for a number of low and high Reynolds number configurations, and comparisons with test data have been made. The physics behind the rotor interactions has been explored through visualization and analysis of vortex wake trajectories and inflow velocity distributions.

The contributions of this work to the state of the art are as follows.

1. The GT-Hybrid analysis, previously developed for single rotor and coaxial rotor configurations has been generalized for multi-rotor configurations. Any number of rotors may be considered. The rotor axes may be offset by user specified values. The angular velocity vectors for the individual rotors may also be pointing in different directions. The rotor angular velocity magnitude may be specified independently for each of the rotors. Thus, the present solver is capable of modeling other forms of interactions including main rotor-tail rotor, and main rotor-propulsor interactions.
2. In addition to performance data (thrust and power as a function of rotor settings), three-dimensional numerical simulations provide a wealth of information about the tip vortex structure, and the velocity field. A fast off-body velocity field analysis that employs GPU processors has been implemented. In addition to computation of inflow velocity field above or below the rotor disks, this approach is capable of rapidly computing and visualizing velocity field on any user specified plane. In many helicopters design

studies, the adverse interactions caused by the main rotor wake should be considered in the placement of horizontal and vertical stabilizers, as well as the tail rotors and pusher-propulsors. This capability for rapid calculation and visualization of the off-body flow field would greatly aid the designers in the placement of these components.

3. A previously developed algebraic transition model that regulates the magnitude of the production term in the Spalart-Allmaras one-equation turbulence model has been independently implemented in the present solver, and in the commercial CFD solver ANSYS Fluent as a user-defined function. Previous validation of this model was limited to 2-D flow over airfoils in the transitional Reynolds number regime. In the present work, this model has been also validated for large scale rotors in hover.

Low Reynolds number and high Reynolds number simulations for the multi-rotor configurations were analyzed. Inflow velocity field was examined, and the first three terms in the dynamic inflow (uniform component, and the lateral and longitudinal variations) were examined. Based on the studies reported in Chapters 3 and 4 of this work, the following conclusions may be drawn.

1. In the case of coaxial rotors, significant interference of the upper rotor downwash over the lower rotor may be captured and adequately quantified with the present hybrid Navier-Stokes/vortex wake model.
2. For the tandem rotor configuration, the effect of rotor interference on induced power variations has been captured. The tip vortex and inner wake structures have been examined to understand the flow physics that influences the inflow distribution. The effects of overlap on the inflow and on the wake geometry is captured in a physically

consistent fashion. In addition, the longitudinal variation of the inflow is properly captured for forward flight conditions.

3. For the upstream rotor of a tandem configuration, it is seen that the time averaged quantity λ_0 decreases slowly with increased axial spacing since the induction effects attributable to the rear rotor on the front rotor decrease with distance. For the downstream rotor, λ_0 initially varies rapidly with the axial spacing due to the interaction of the upstream rotor wake with the downstream rotor disk. As the axial separation increases beyond 0.5R, λ_0 becomes less sensitive to axial separation.
4. As may be expected, the rotor on the right, which operates partially in the outflow of the left rotor experiences higher λ_0. This, in practice, would translate into higher power consumption for the right rotor compared to the left. The coefficient λ_0 for the two rotors approaches each other as the axial separation as a fraction of the rotor radius R increases.

It is recommended that the following additional studies be done to further improve the predictions.

1. All the simulations in this work were done using a default body-fitted grid. The radial, chordwise, and normal spacing of the grid (as a function of rotor radius and local chord) were established from previous grid sensitivity studies done for large scale rotors such as UH-60A and S-76. The spacing needs to be reexamined for low Reynolds number configurations, since the boundary layers tend to be thicker, and the highly clustered grid spacing in the direction normal to the body required in high Reynolds number simulations may be relaxed to provide better resolution of the flow field elsewhere.

2. The hybrid Navier-Stokes/free wake solver has used the Spalart-Allmaras model, optionally with an algebraic transition model for high Reynolds number configurations. The solver includes other models (e.g. k-ω-SST two equation model). The computational structure of these two equation models also may be extended to add one- and two-equation transition models (for Reynolds number based on momentum thickness, and the intermittency factor).
3. The off-body velocity flow solver, implemented on GPU processors, is extremely fast and is capable of predicting velocity field on any 2-D plane specified by the user. There are several enhancements that could be done to speed up the computation. First, the memory on the host side may be allocated as pinned memory. This would shorten the data copying process between the host and the device. Secondly, using the technique of asynchronous memory copy operations, it should be possible to reduce the total runtime. The kernel processes would continue to execute the kernel, while the data is being copied from host to device and ready for the computation.
4. As stated earlier, the present solver is capable of modeling main rotor-tail rotor interactions, and main rotor-propulsor interactions. Ground effects may also be modeled using images of the main rotor(s) and the wake structures. These interesting applications should be pursued in future studies.
5. The present physics-based model provides a wealth of information on the rotor wake structure, and wake distortion. It is therefore possible to compare the inflow velocity distribution from the present simulation with a classical skewed helical wake model without contractions or distortion, and empirically improve the classical models. Empirical corrections to the dynamic inflow models should also be pursued, following

the pioneering work on wake curvature correction models developed by Prasad and his coworkers [113].

6. The present approach is capable of modeling helicopter rotors in autorotative flight. Vertical descent, and descent in forward flight both may be modeled. Companion versions of the GT-Hybrid have already been used to model horizontal axis wind turbines, with comparisons against test data and other simulations [114]. An interesting application of the present methodology would be to a study of yaw control of coaxial rotors in autorotative descent. As discussed earlier, rotor trim and yaw control (requiring generation of a net torque) is done in hover and forward flight by adjusting the collective pitch settings of the upper and lower rotor. In forward flight and hover, the inflow through the rotor is predominantly from above the rotor disk to the region below. In autorotative flight, there may be a net upward directed flow through much of the rotor disk. The trim logic should adjust the pitch setting for this upward directed flow. It is recommended that the present approach be extended to the modeling of coaxial rotor trim and yaw control under autorotative flight conditions.
7. A number of researchers, including Prasad and his coworkers, have explored the stability and control aspects of rotors in autorotative flight at high advance ratios [115]. These studies have used dynamic inflow model that are well validated only for conventional flight without autorotative effects. The present approach with its ability to model the inflow distribution through a free wake analysis provides a useful tool for exploring autorotative flight of rotors at high advance ratios.
8. As pointed out by Peters [113], the off-axis response of helicopters during pull-up maneuvers are not correctly predicted by classical dynamic inflow models. Prasad and

his coworkers were able to improve the predictions through the inclusion of wake curvature effects [116]. These corrections partially account for the closer stacking of the rotor wake on the aft side of the rotor disk compared to forward side. It is recommended that the present work be extended to address these important and interesting phenomena.

In summary, a computationally efficient Navier-Stokes/free wake model has been generalized for multirotor configurations and used to study multi-rotor interaction phenomena. It is hoped that this work would serve as a stepping stone for future work in this important and interesting field.

APPENDIX A. Transition Model Implementation

A.1 Spalart-Allmaras (SA-BCM) Transition Model

The formulation and the validation cases for the implementation of the Spalart-Allmaras (SA-BCM) transition model are described in this section.

A.1.1 Original Spalart-Allmaras 1-equatuin turbulence model

The Spalart-Allmaras 1-equation BCM transition model is modified based on the original Spalart-Allmaras turbulence model [117-119]. The original Spalart-Allmaras turbulence model is a classical eddy viscosity model that links the shear stresses to the strain rate as shown below.

$$\tau_{ij} = 2\mu_t \left(S_{ij} - \frac{1}{3}\frac{\partial u_k}{\partial x_k}\delta_{ij} \right) \tag{A-1}$$

Here S_{ij} is the mean rate of strain tensor, μ_t is the turbulent eddy viscosity, and δ_{ij} is the Kronecker delta.

A single equation is used to model turbulent viscosity transport in the Spalart-Allmaras turbulent model. The formulation for the turbulent viscosity transport equation can be decomposed into convection, production, dissipation, and diffusion terms which has the form below.

$$\frac{\partial \hat{\nu}}{\partial t} + u_j \frac{\partial \hat{\nu}}{\partial x_j} = c_{b1}(1 - f_{t2})\hat{S}\hat{\nu} - \left[c_{w1} f_w - \frac{c_{b1}}{\kappa^2} f_{t2}\right]\left(\frac{\hat{\nu}}{d}\right)^2 + \frac{1}{\sigma}\left[\frac{\partial}{\partial x_j}\left((\nu + \hat{\nu})\frac{\partial \hat{\nu}}{\partial x_j}\right) + c_{b2}\frac{\partial \hat{\nu}}{\partial x_i}\frac{\partial \hat{\nu}}{\partial x_i}\right] \tag{A-2}$$

The variable $\hat{\nu}$ in the equation above is related to the turbulent eddy viscosity by the equation below:

$$\mu_t = \rho \hat{\nu} f_{\nu 1}$$
$$f_{\nu 1} = \frac{\chi^3}{\chi^3 + {c_{\nu 1}}^3} \tag{A-3}$$
$$\chi = \frac{\hat{\nu}}{\nu}$$

Here ρ is density, $\nu = \frac{\mu}{\rho}$ is the molecular kinematic viscosity, and μ is the molecular dynamic viscosity. Other definition for the terms in the transport equation are shown below.

$$\hat{S} = \Omega + \frac{\hat{\nu}}{\kappa^2 d^2} f_{\nu 2} \qquad f_{t2} = c_{t3} e^{(-c_{t4}\chi^2)}$$

$$\Omega = \sqrt{2 W_{ij} W_{ij}} \qquad g = r + c_{w2}(r^6 - r)$$

$$W_{ij} = \frac{1}{2}\left(\frac{\partial u_i}{\partial x_j} - \frac{\partial u_j}{\partial x_i}\right) \qquad r = min\left[\frac{\hat{\nu}}{\hat{S}\kappa^2 d^2}, 10\right] \tag{A-4}$$

$$f_{\nu 2} = 1 - \frac{\chi}{1 + \chi f_{\nu 1}} \qquad f_w = g\left[\frac{1 + {c_{w3}}^6}{g^6 + {c_{w3}}^6}\right]^{1/6}$$

Here Ω is the magnitude of the vorticity, and d is the distance from the field point to the nearest wall. The constants used in the standard Spalart-Allmaras turbulent model are:

$$c_{b1} = 0.1355 \qquad \sigma = 2/3 \qquad c_{b2} = 0.622 \qquad \kappa = 0.41$$

$$c_{w2} = 0.3 \qquad c_{w3} = 2 \qquad c_{v1} = 7.1 \qquad c_{t3} = 1.2 \tag{A-5}$$

$$c_{t4} = 0.5 \qquad c_{w1} = \frac{c_{b1}}{\kappa^2} + \frac{1 + c_{b2}}{\sigma} = 3.2391$$

A.1.2 Spalart-Allmaras BCM transition model

The Spalart-Allmaras BCM transition model can be obtained by ignoring f_{t2} term [120, 121] and introducing the intermittency function γ_{BC} into the transport equation of the turbulent eddy viscosity [122-124]. The transport equation then becomes:

$$\frac{\partial \hat{\nu}}{\partial t} + u_j \frac{\partial \hat{\nu}}{\partial x_j} = \gamma_{BC} c_{b1} \hat{S} \hat{\nu} - c_{w1} f_w \left(\frac{\hat{\nu}}{d}\right)^2 + \frac{1}{\sigma}\left[\frac{\partial}{\partial x_j}\left((\nu + \hat{\nu})\frac{\partial \hat{\nu}}{\partial x_j}\right) + c_{b2}\frac{\partial \hat{\nu}}{\partial x_i}\frac{\partial \hat{\nu}}{\partial x_i}\right] \tag{A-6}$$

The intermittency distribution function γ_{BC} is added as a multiplier to the production term. The intermittency distribution function is designed such that there is no turbulent production ($\gamma_{BC} = 0.0$) before the transition onset criteria is achieved. After the flow has fully transitioned to turbulent flow, the turbulent flow is modeled with the intermittency distribution function set to unity ($\gamma_{BC} = 1.0$). The quantity γ_{BC} is computed as follows:

$$\gamma_{BC} = 1 - e^{\left(-\sqrt{Term1}-\sqrt{Term2}\right)} \tag{A-7}$$

There are two terms in formulation of the intermittency distribution function. The first term $Term1$ is responsible for checking the onset location of the transition by comparing the locally calculated critical momentum thickness Reynolds number (Re_θ) to the experimental correlation value ($Re_{\theta c}$).

$$Term1 = \frac{max(Re_\theta - Re_{\theta c}, 0.0)}{\chi_1 Re_{\theta c}}$$

$$\chi_1 = 0.002$$

$$Re_\theta = \frac{Re_\nu}{2.193} \tag{A-8}$$

$$Re_\nu = \frac{\rho d^2}{\mu}\Omega$$

$$Re_{\theta c} = 803.73(T_{u\infty} + 0.6067)^{-1.027}$$

Here $T_{u\infty}$ is the freestream turbulence intensity. The formulation for the $Re_{\theta c}$ is the result of curve fits from experimental observations [125].

Since the term Re_ν within the $Term1$ is a function of wall distance, which is very small inside the boundary layer, the second term, $Term2$, is designed to trigger transition within the boundary layer:

$$Term2 = max\left(\chi_2 \frac{\nu_t}{\nu}, 0.0\right) \tag{A-9}$$

$$\chi_2 = 50$$

$$\nu_t = \hat{\nu} f_{\nu 1}$$

The definition and the parameter used for the other terms is the same with the original Spalart-Allmaras turbulence model.

A.1.3 Validation of the SA-BCM transition model on the 2D airfoil (E387 airfoil)

The Spalart-Allmaras BCM transition model has been implemented first in a 2D compressible flow analysis called Dynamic Stall Solver version 2 (DSS2). The DSS2 is an in-house two-dimensional compressible Navier-Stokes solver which employs standard second order accurate central difference to approximate the spatial derivatives and first order accurate, backward difference to approximate the time derivative. The set of artificial dissipation terms which combined the second and the fourth order difference is used to control the high-frequency spatial oscillations [126, 127]. The Spalart-Allmaras BCM transition model has been implemented in DSS2 through the addition of the intermittency distribution function as a multiplier in the production term of the existing standard Spalart-Allmaras turbulence model, as discussed earlier.

Validation studies have been done for the Eppler E387 low Reynolds number airfoil, as shown in the Figure A-1, comparing the predictions with available experimental data at a Reynolds number of 200,000.

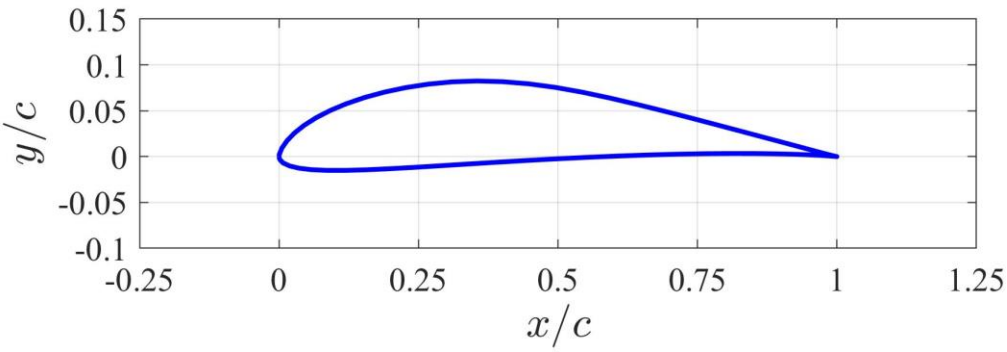

Figure A-1 E387 airfoil

A.1.3.1 Mesh sensitivity study

A two-dimensional C-type body fitted grid is generated with an in-house grid generator with user specified parameters including the number of points in both the wrap around (i-dir) and normal (j-dir) directions. The parameters and the total cells number for the three sets of the grid used in the mesh sensitivity study are shown in Table A-1.

Table A-1 Mesh sensitivity study

Mesh	# cells in i-direction	# cells in j-direction	# cells on airfoil surface	Total # cells
151×45	151	45	90	6,795
521×180	521	180	360	93,780
921×220	921	220	720	202,620

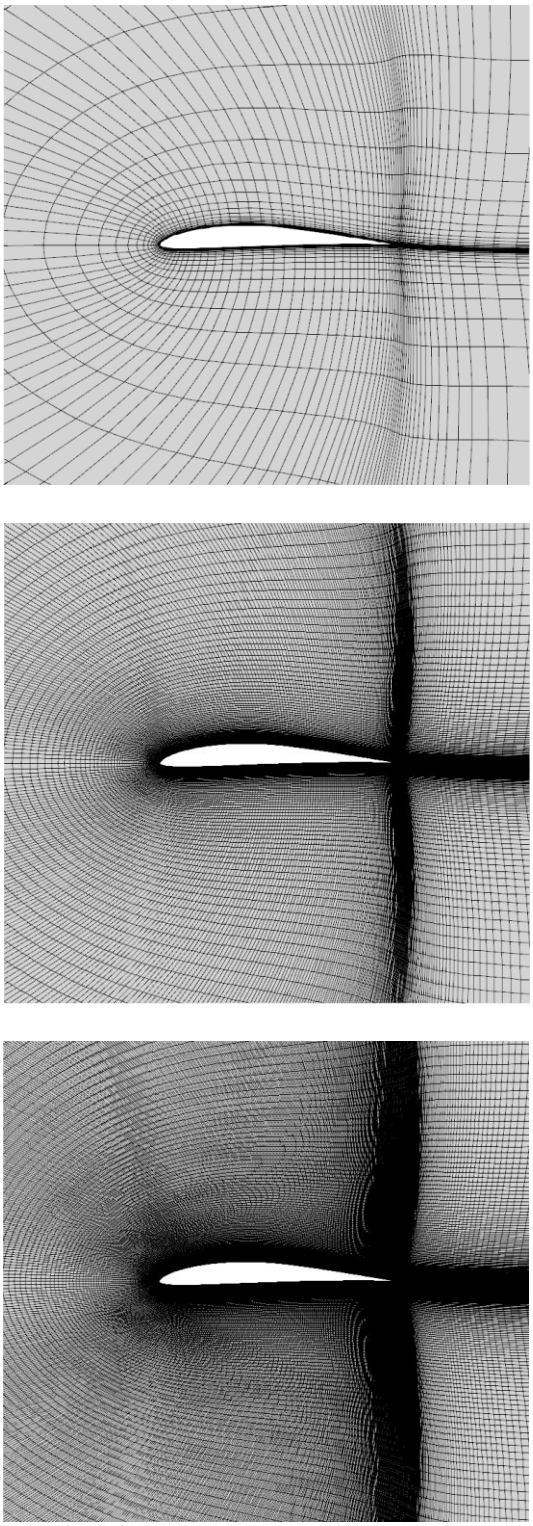

Figure A-2 Two-dimensional C-type grid top (151×45), middle (521×180), bottom (921×220) used in DSS2 for the E387 airfoil

As seen in the Figure A-3, the lift and drag values at an angle of attack of 2 degrees asymptotically converge to their final values as the grid is progressively refined. The finest grid (921×220) has been used for all other values of angles of attack, ensuring a good resolution of the transition location on the surface of the airfoil.

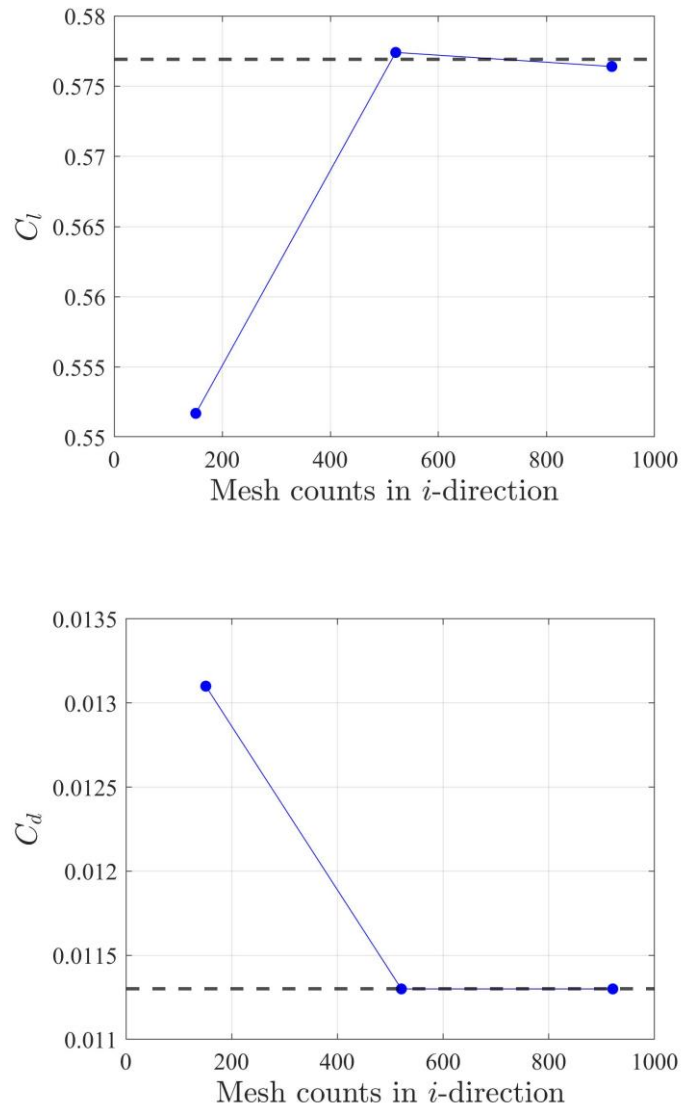

Figure A-3 Mesh sensitivity study for the E387 airfoil at a Reynolds number of 200,000 at 2° angle of attack

A.1.3.2 Comparison between simulation and experimental data

The Spalart-Allmaras turbulence model with and without the BCM transition model have been used to simulate E387 airfoil at a Reynolds number of 200,000 for angles of attack ranging from -3 to 8 degrees. The focus of this study is to capture the performance within the moderate lift coefficient range as shown in the Figure A-4. Both the baseline SA turbulence model and the SA-BCM transition model demonstrate reasonable agreement with experiment data for lift coefficient vs angle of attack. The use of the transition model gave rise to a somewhat higher lift coefficient compare to the baseline turbulence model, in closer agreement to the measurements.

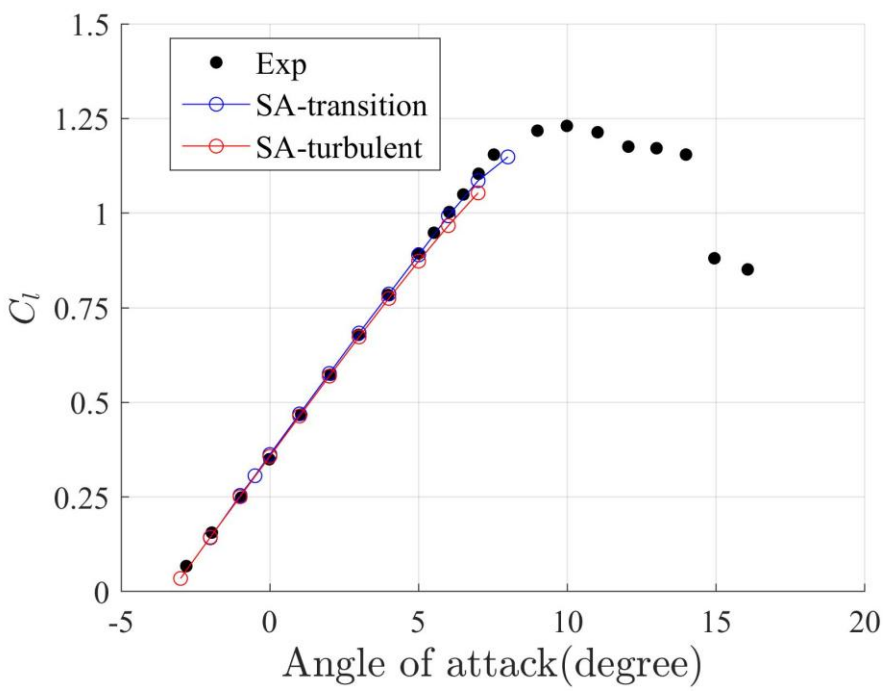

Figure A-4 Variation of the lift coefficient with angle of attack

As shown in the Figure A-5, at Reynolds number of 200,000 case, the drag polar is well captured by SA-BCM transition model on the moderate lift coefficient range.

However, this model performed poorly in the vicinity of airfoil stall. Further study is needed to understand the causes for the difference between numerical modeling and experimental measurements.

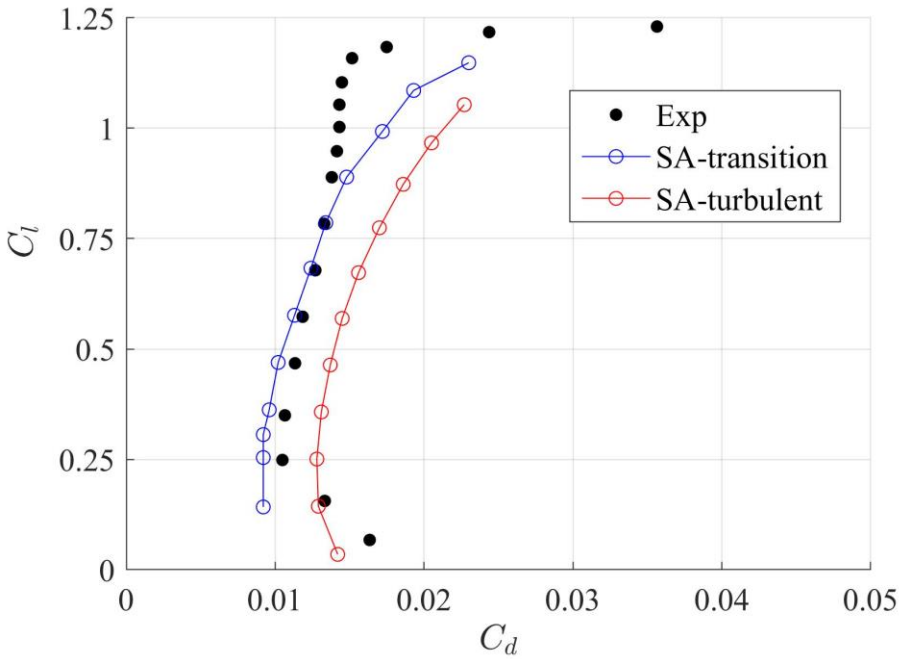

Figure A-5 E387 drag polar

A.1.4 Validation of the SA-BCM transition model on the single rotor (S-76 rotor)

The Spalart-Allmaras BCM transition model was next implemented into GT-Hybrid for 3-D applications. An intermittency distribution function was added to the subroutine for computing the turbulent eddy viscosity. With this implementation, the user may specify at run time whether a pure laminar, pure turbulent, or a transitional flow should be modeled.

A.1.4.1 S-76 rotor

The 3-D version of the solver has been validated against test data for a rotor in hover. This configuration is a 1/5.71 scaled model of the S-76 rotor [128]. The rotor radius is 1.423m (56.04 in.) in radius, and the chord length is 0.0787m (3.1in). The blade is made of SC1095 and SC1094 R8 airfoils with a -10° linear twist. The solidity of the rotor is 0.0704. The detail geometry and the planform of the S-76 rotor in shown in Figure A-6.

This configuration is one of the benchmark cases in AIAA Rotorcraft Hover Prediction Workshop (HPW) [129, 130]. Several CFD methodologies have been applied by numerous researchers to study this rotor including OVERFLOW [131], OVERTURNS [132], HPCMP CREATE^{TM}-AV Helios [95, 133], U^{2}NCLE [134], KAIST [135], STAR-CCM+ [136], and GT-Hybrid [137-139]. Promising results for the performance prediction have been obtained by coupling the $\gamma - \overline{Re_{\theta t}}$ transition model with Spalart-Allmaras turbulent model in the OVERFLOW solver [140].

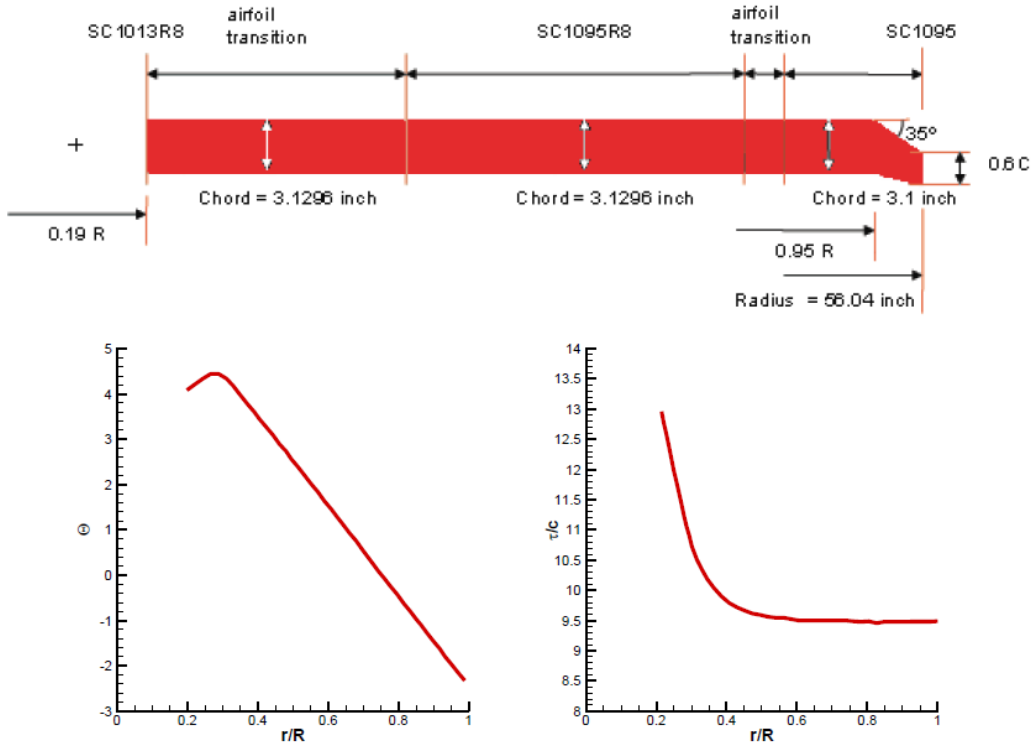

Figure A-6 S-76 rotor planform

A.1.4.2 Mesh of S-76 rotor

The computational domain in this study does not include the rotor hub since the effect of the hub on the S-76 rotor performance in hover is considered negligible [141]. The mesh used in the present study has 291 nodes in the wrap-around direction, 128 in the spanwise direction, and 45 in the normal direction. The C-type body fitted grid, generated with an in-house grid generator, is shown in Figure A-7.

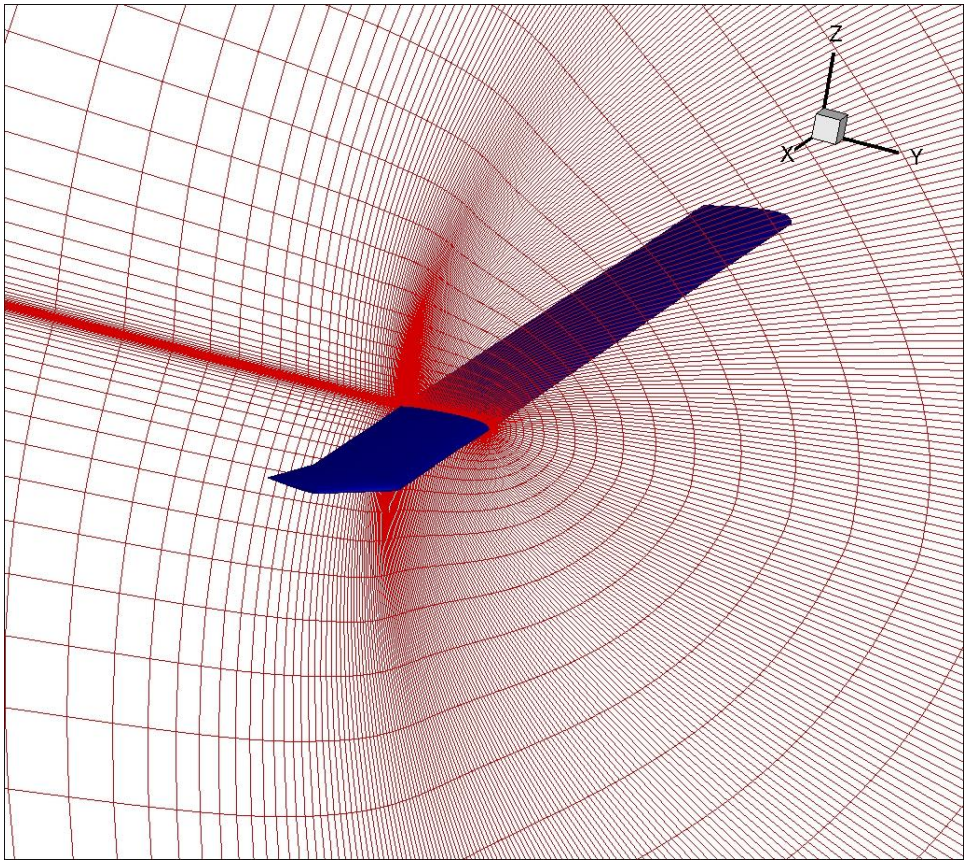

Figure A-7 Grid (291×128×45) used in GT-Hybrid

A.1.4.3 Comparison between simulation and experimental data

As shown in Figure A-8, the baseline Spalart-Allmaras turbulence model overpredicts the power coefficient, especially at the low thrust setting, resulting in lower figures of merit. On the other hand, a fully laminar flow underpredicts the power coefficient. The power coefficient as well as the figure of merit predicted by the present transition model agree well with experimental measurements over a broad range of thrust settings.

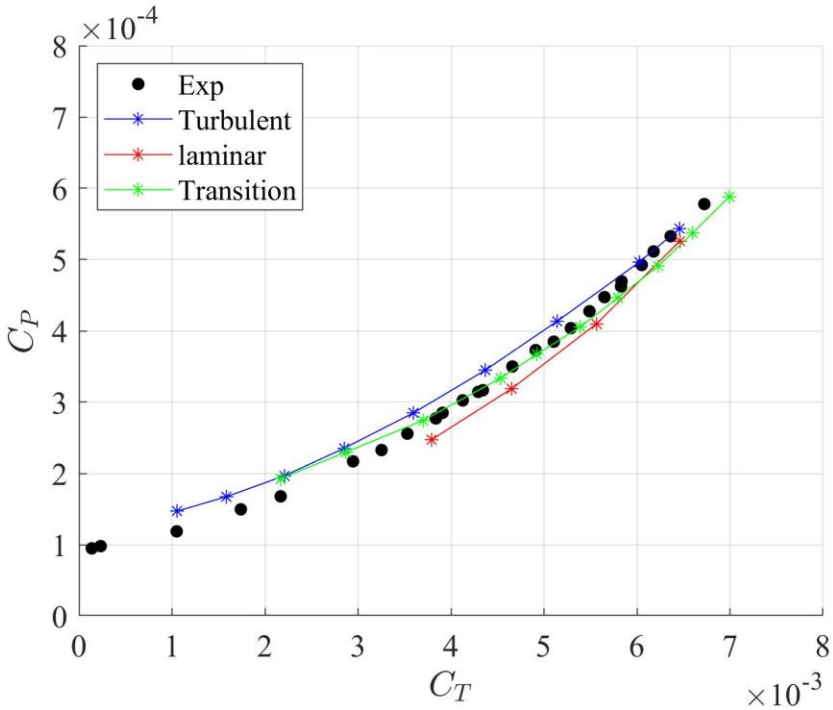

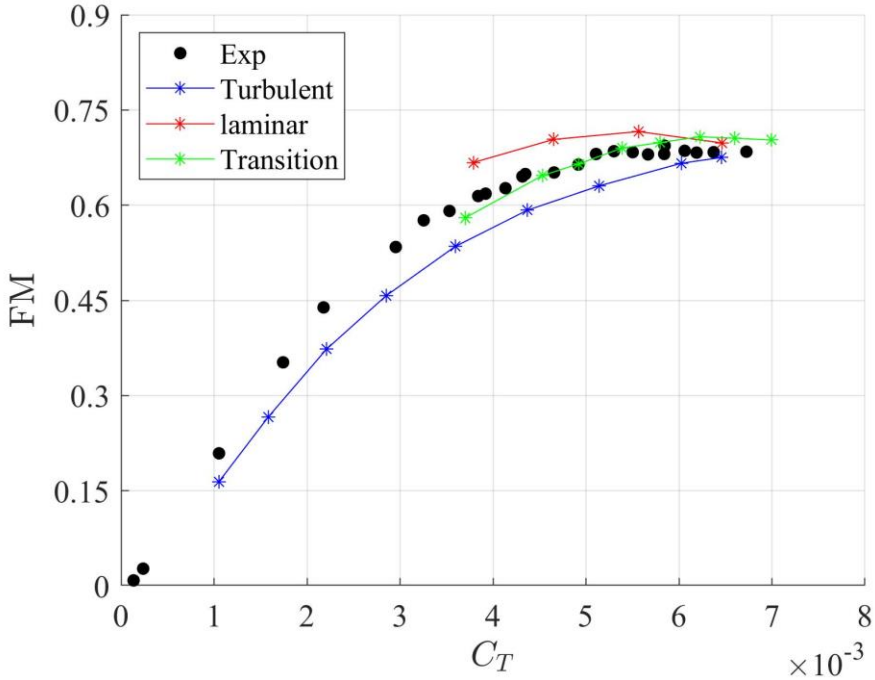

Figure A-8 Comparison between numerical simulations and experimental measurement for the S-76 rotor at M_{tip} = 0.65

APPENDIX B. Additional Inflow distribution plots

Chapter 4 of this document included comparisons of the predicted velocity field with test data at only a few conditions. For the sake of completeness, additional induced velocity contour plots and sectional velocity distribution plots are listed in this section.

These contour plots are listed in the following order: coaxial rotor, side-by-side rotor, and tandem rotor configuration.

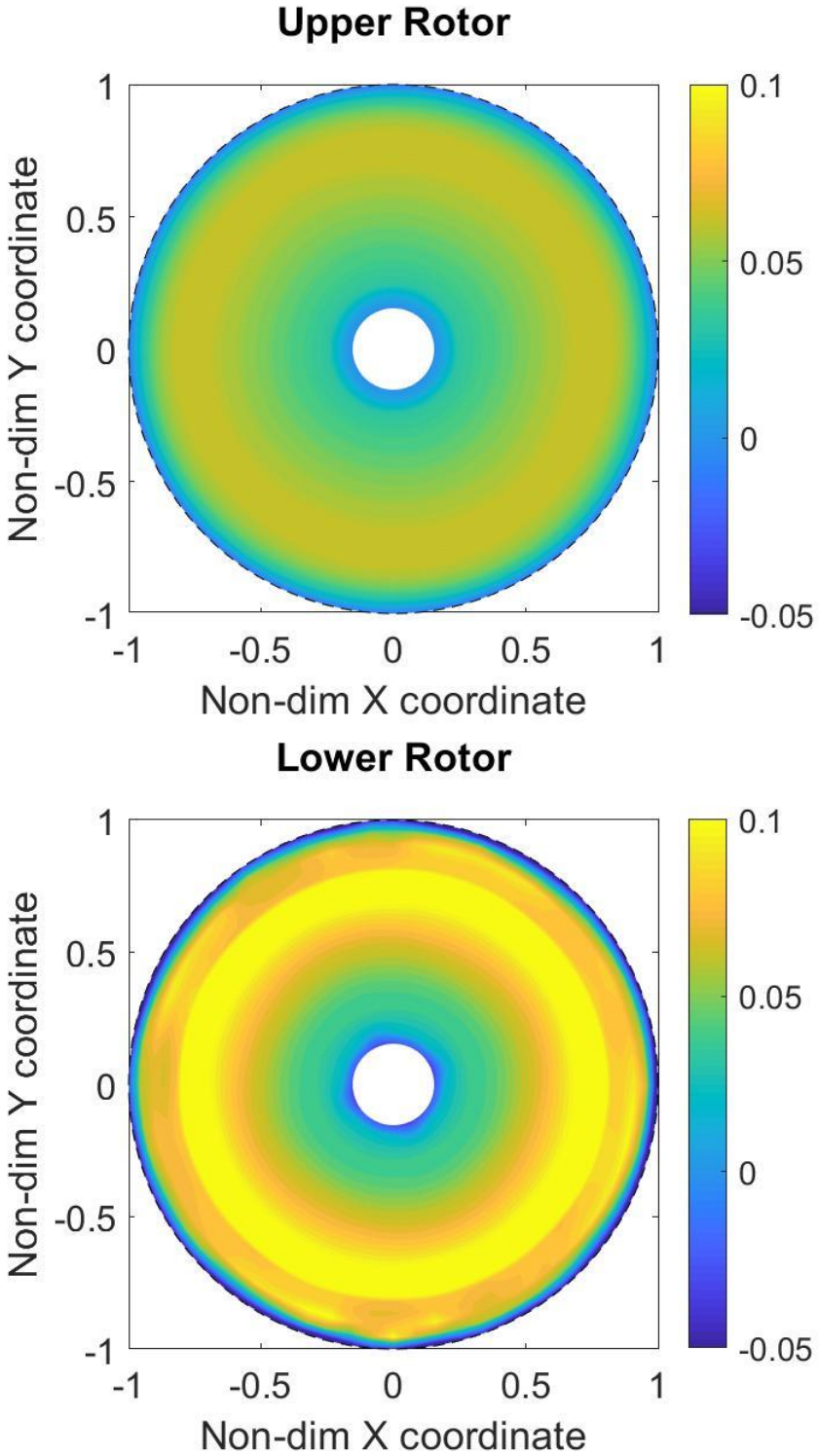

Figure B-1 Induced velocity contour plot on the rotor disk for VS=0.25R, AS=0.00R

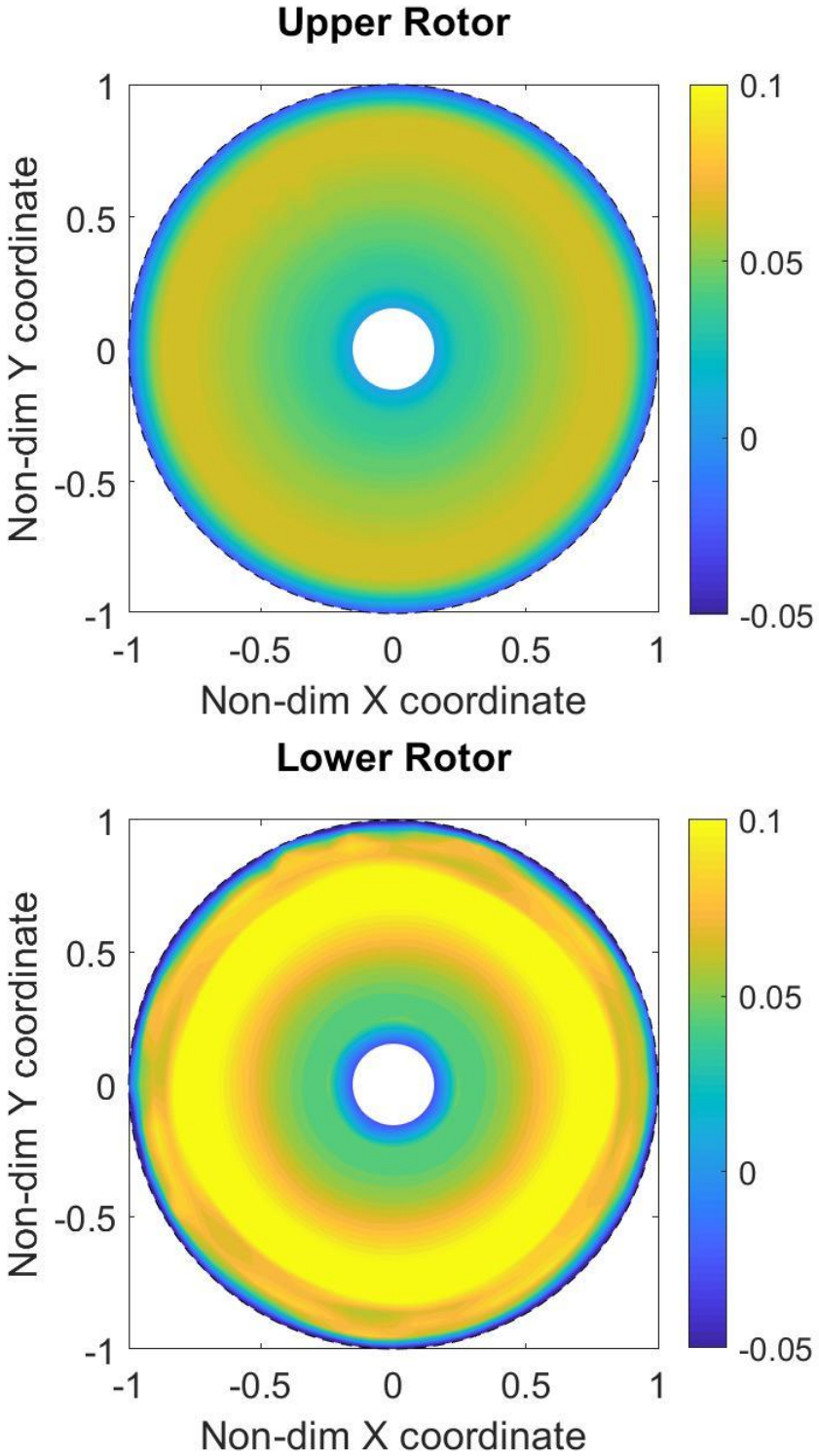

Figure B-2 Induced velocity contour plot on the rotor disk for VS=0.40R, AS=0.00R

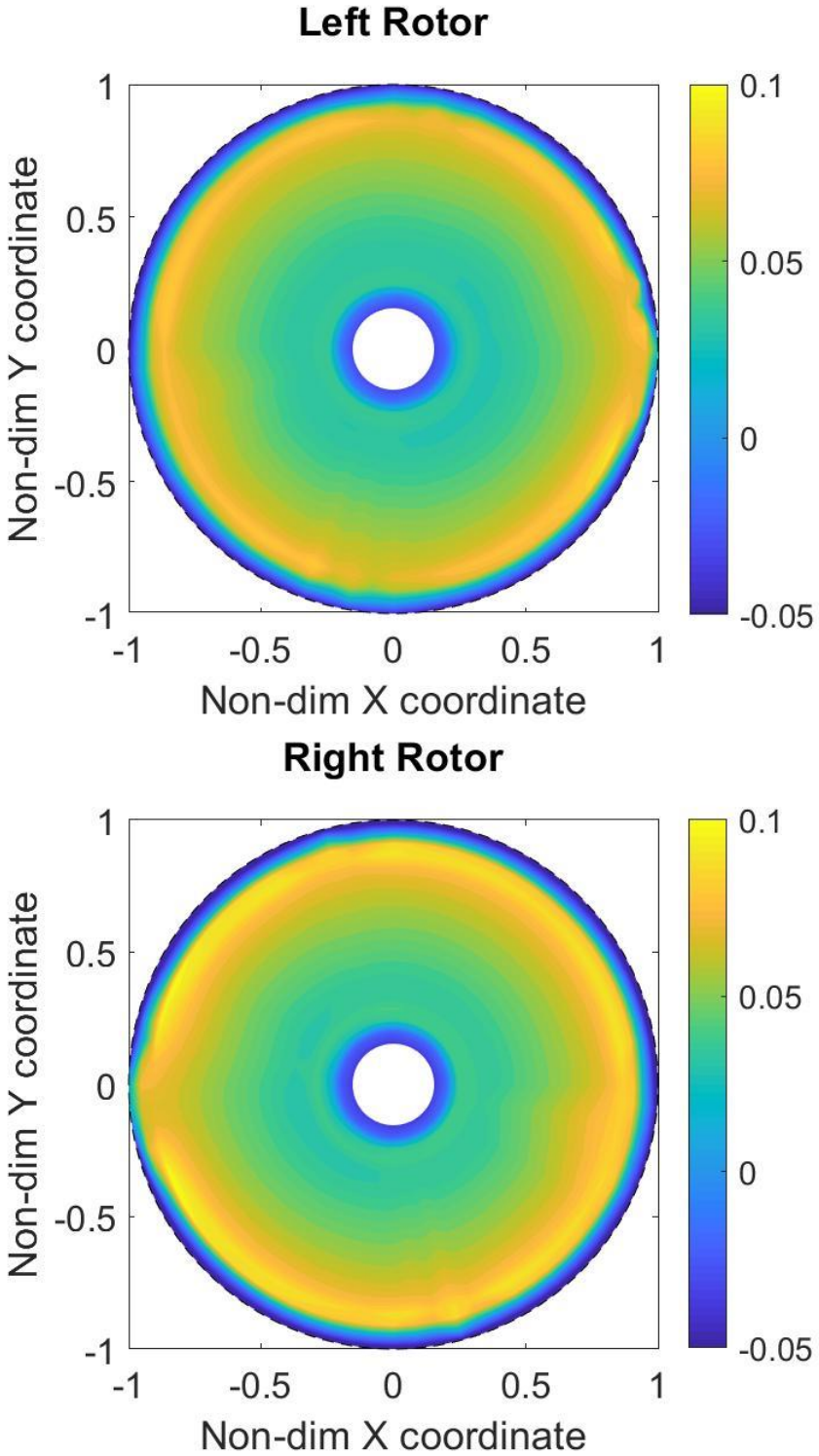

Figure B-3 Induced velocity contour plot on the rotor disk for VS=0.00R, AS=2.10R

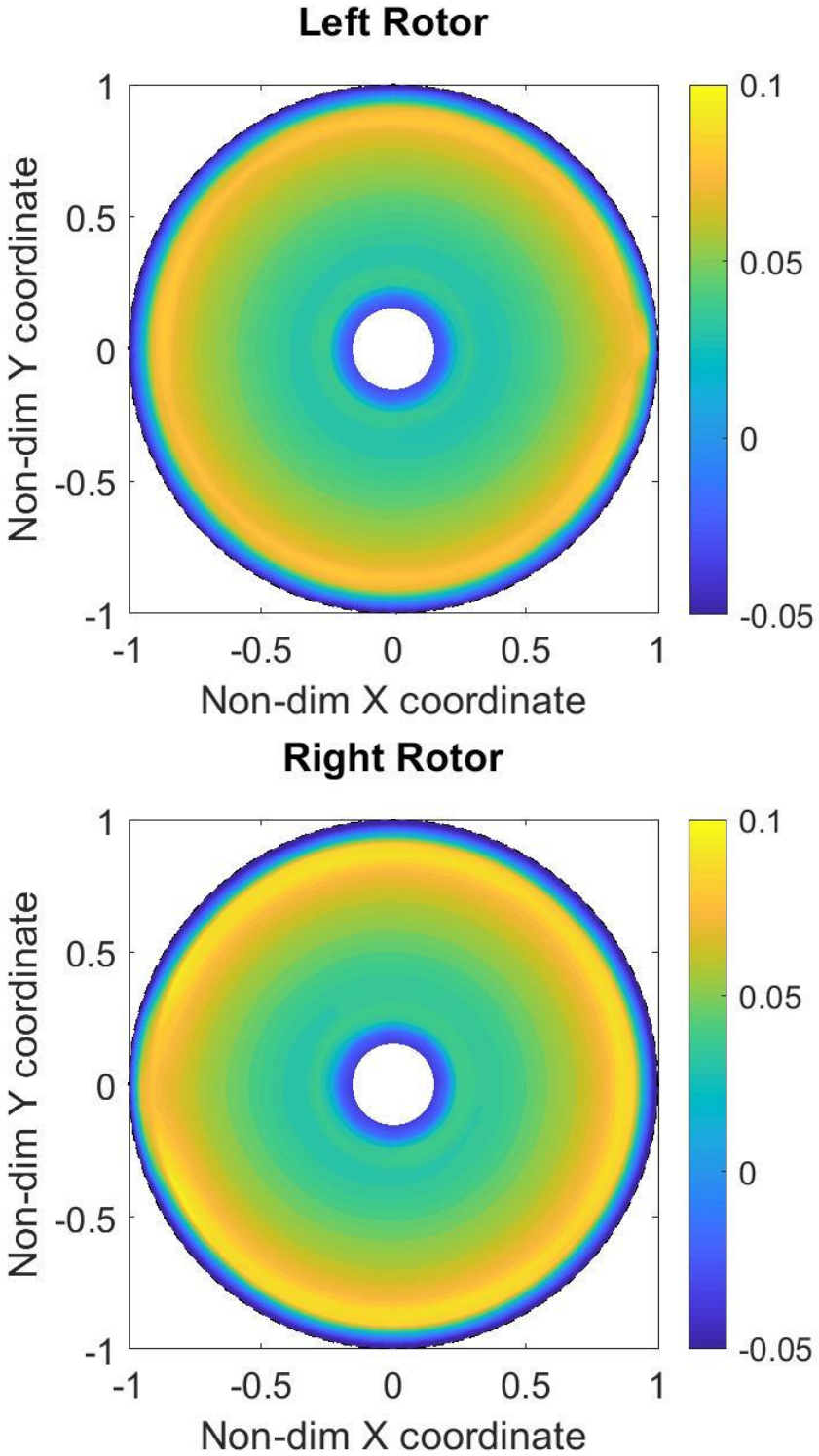

Figure B-4 Induced velocity contour plot on the rotor disk for VS=0.00R, AS=2.20R

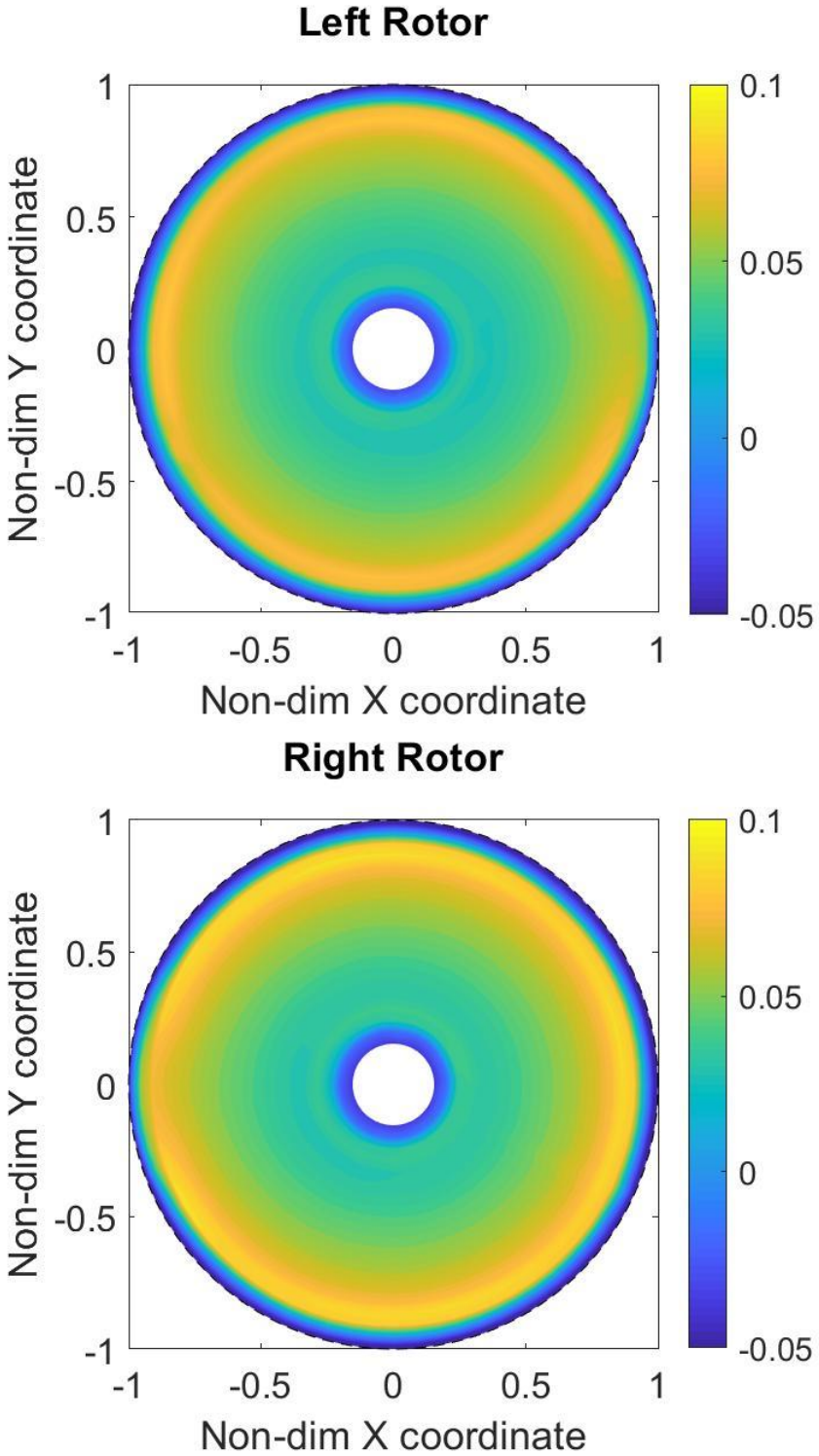

Figure B-5 Induced velocity contour plot on the rotor disk for VS=0.00R, AS=2.30R

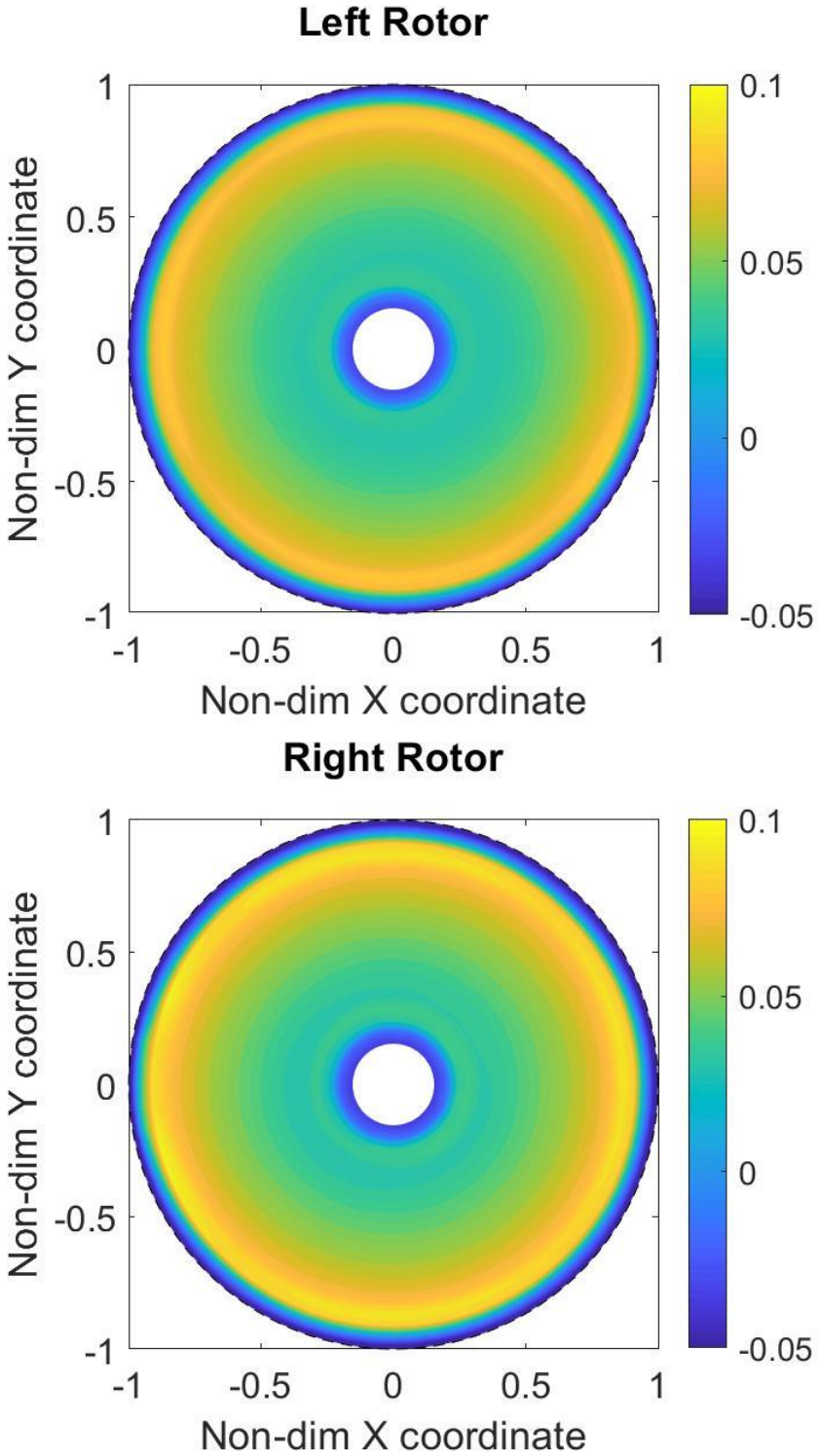

Figure B-6 Induced velocity contour plot on the rotor disk for VS=0.00R, AS=2.40R

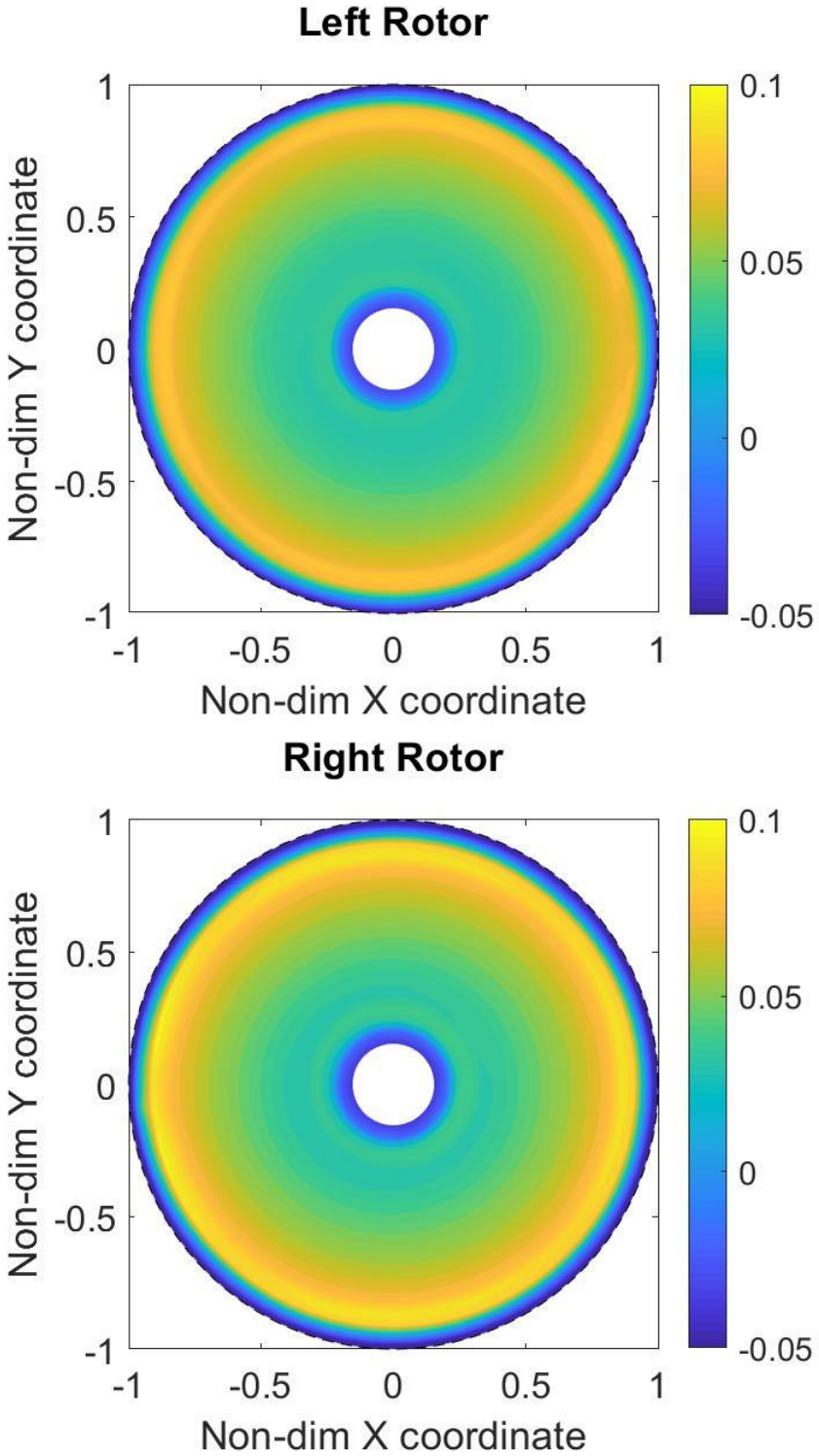

Figure B-7 Induced velocity contour plot on the rotor disk for VS=0.00R, AS=2.50R

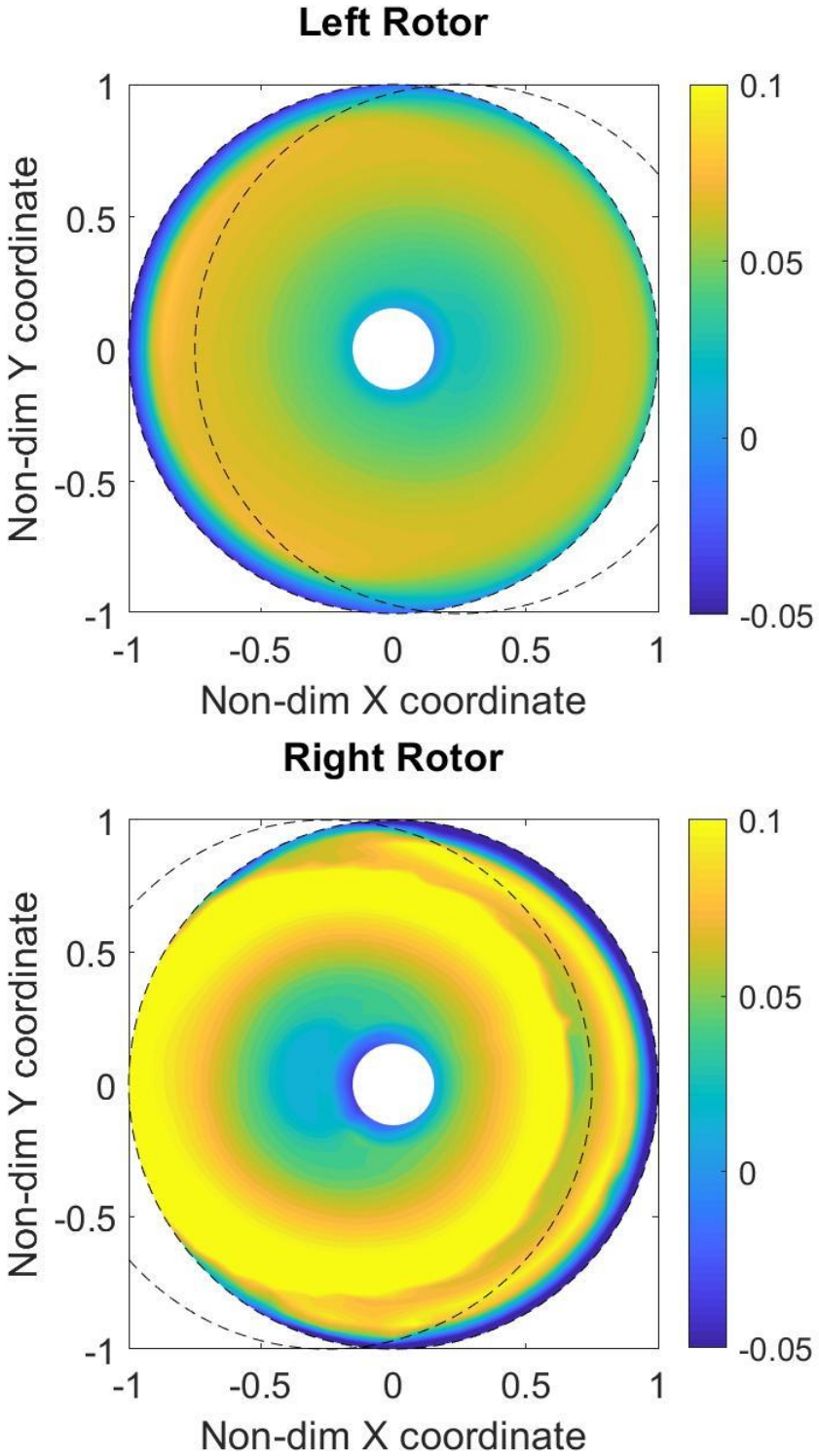

Figure B-8 Induced velocity contour plot on the rotor disk for VS=0.25R, AS=0.25R

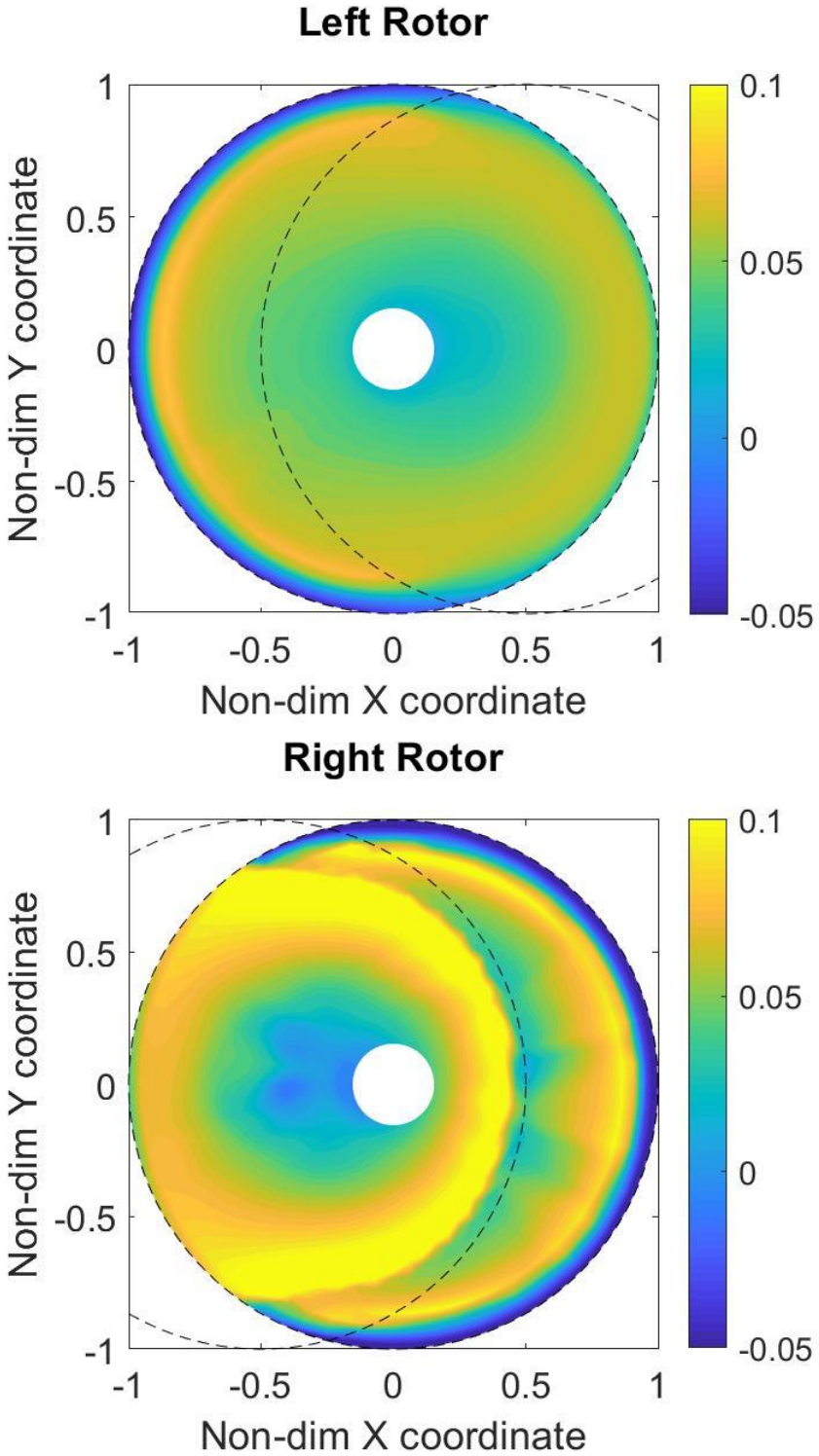

Figure B-9 Induced velocity contour plot on the rotor disk for VS=0.25R, AS=0.50R

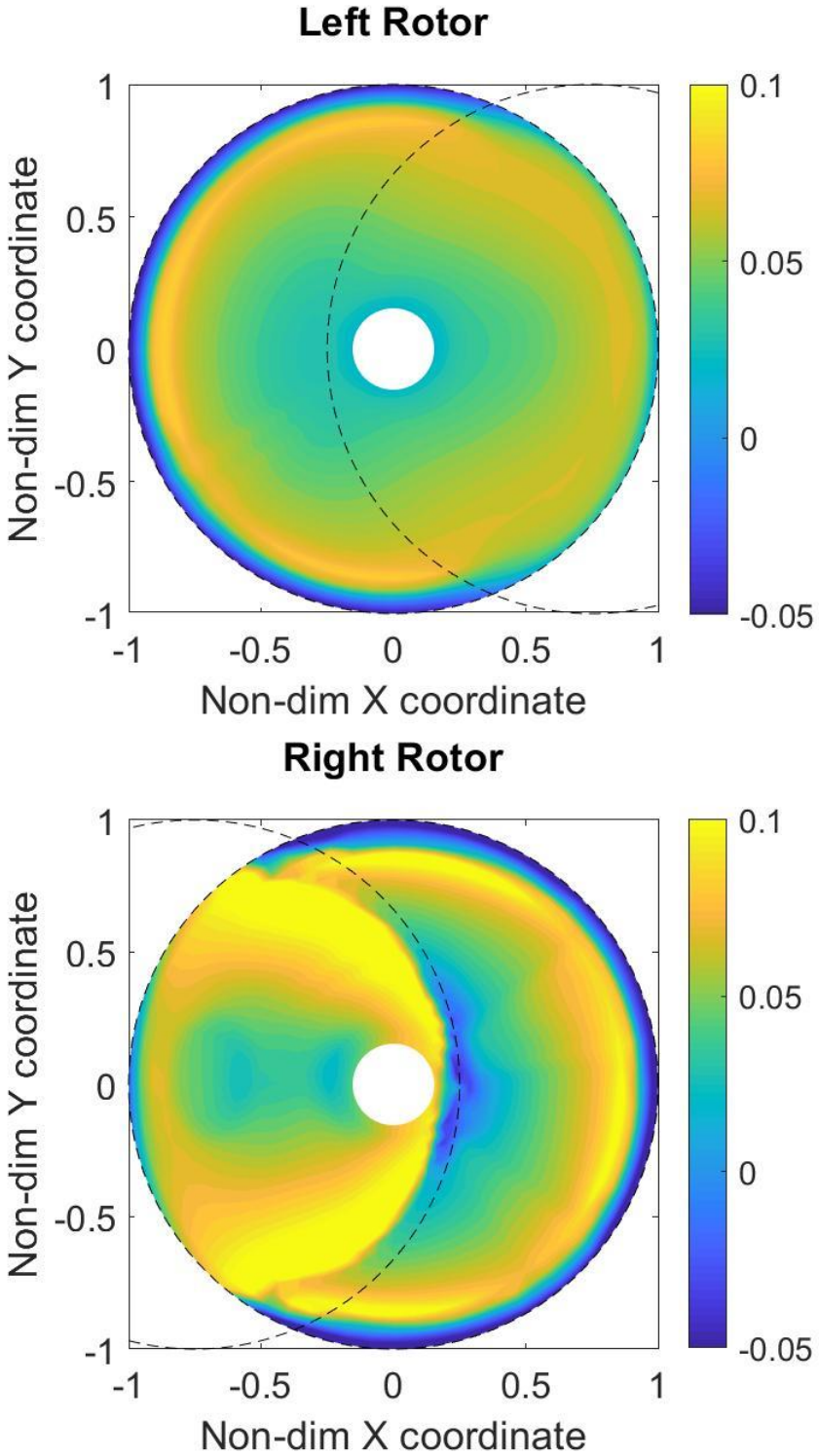

Figure B-10 Induced velocity contour plot on the rotor disk for VS=0.25R, AS=0.75R

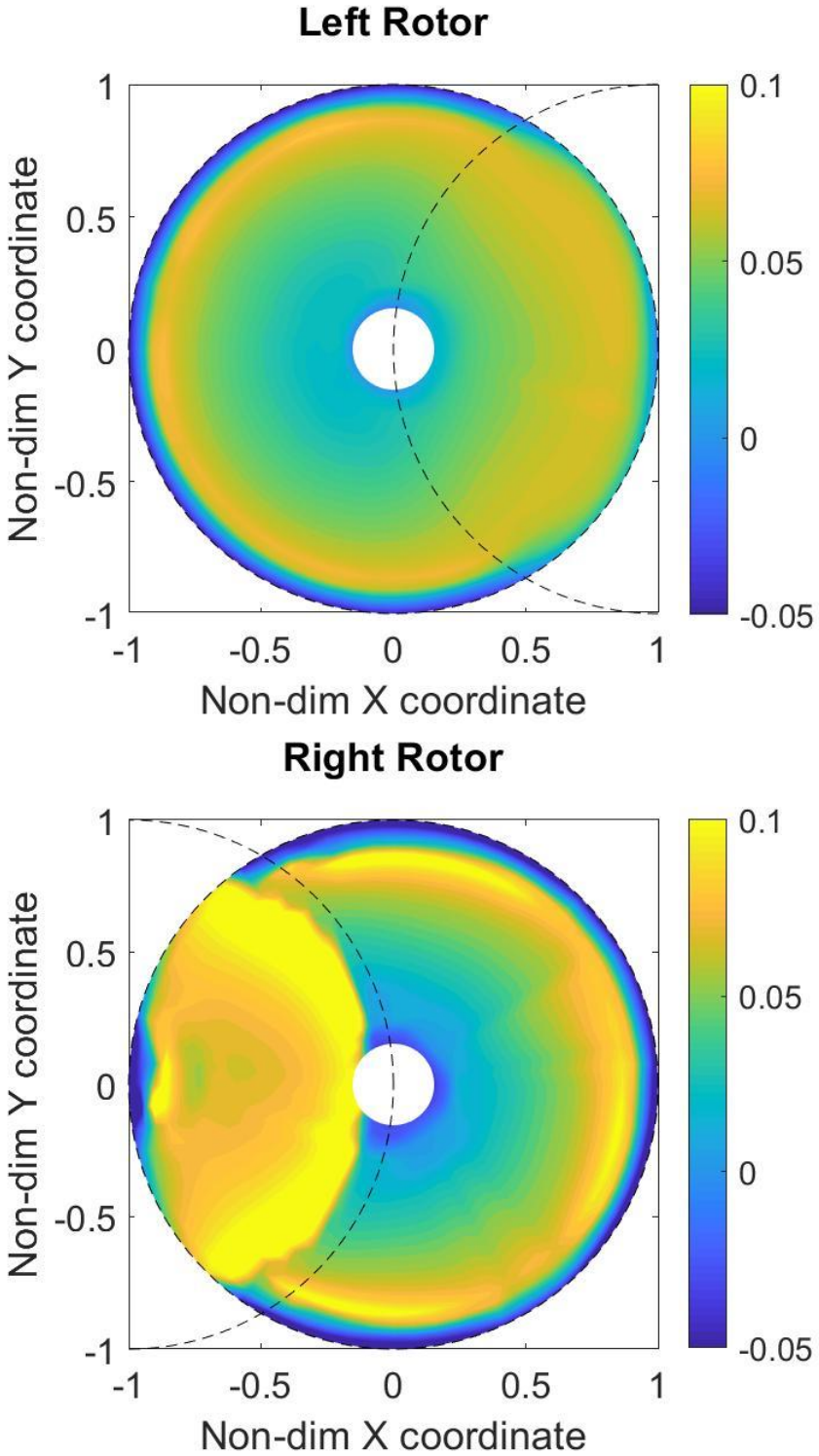

Figure B-11 Induced velocity contour plot on the rotor disk for VS=0.25R, AS=1.00R

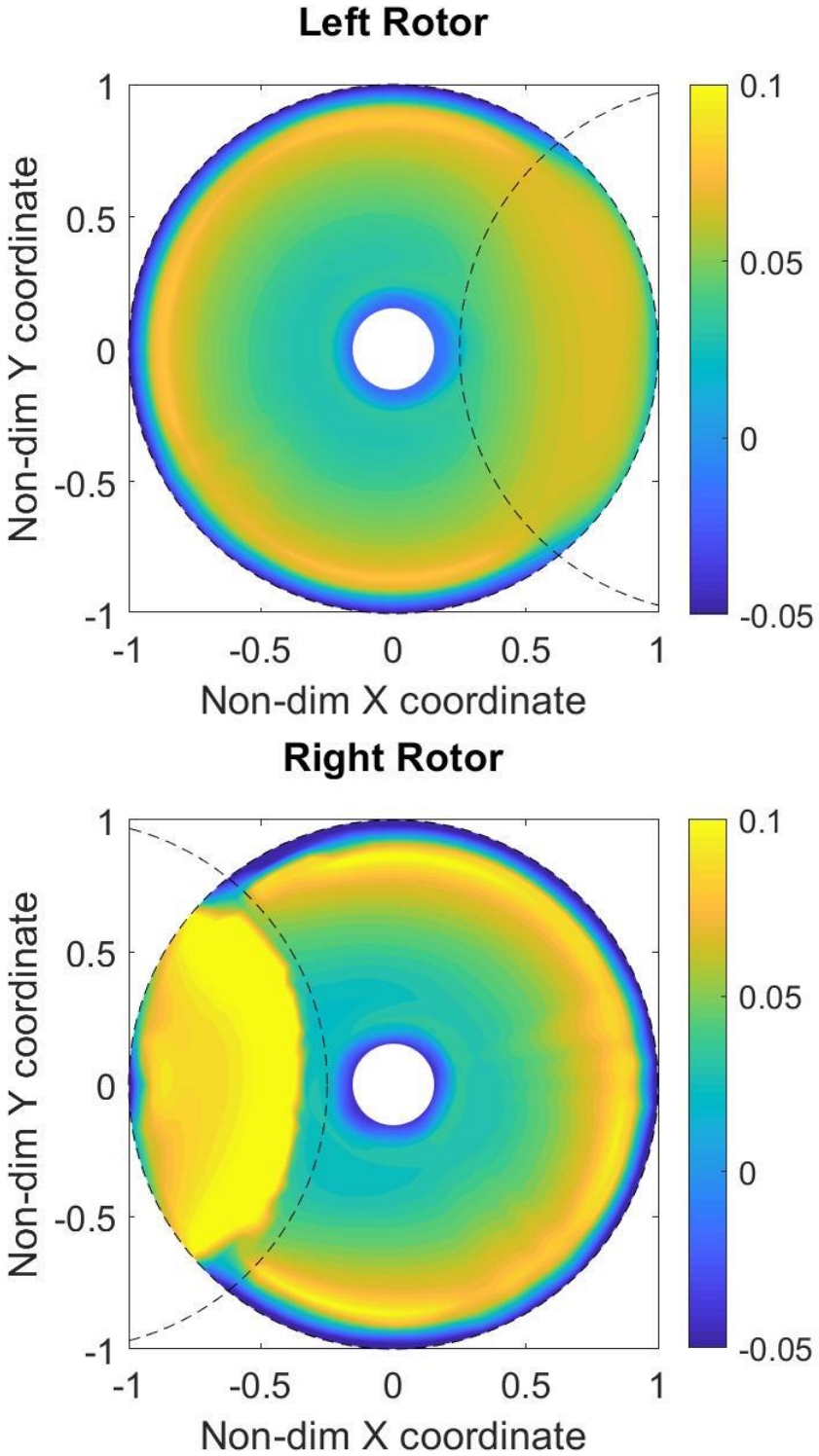

Figure B-12 Induced velocity contour plot on the rotor disk for VS=0.25R, AS=1.25R

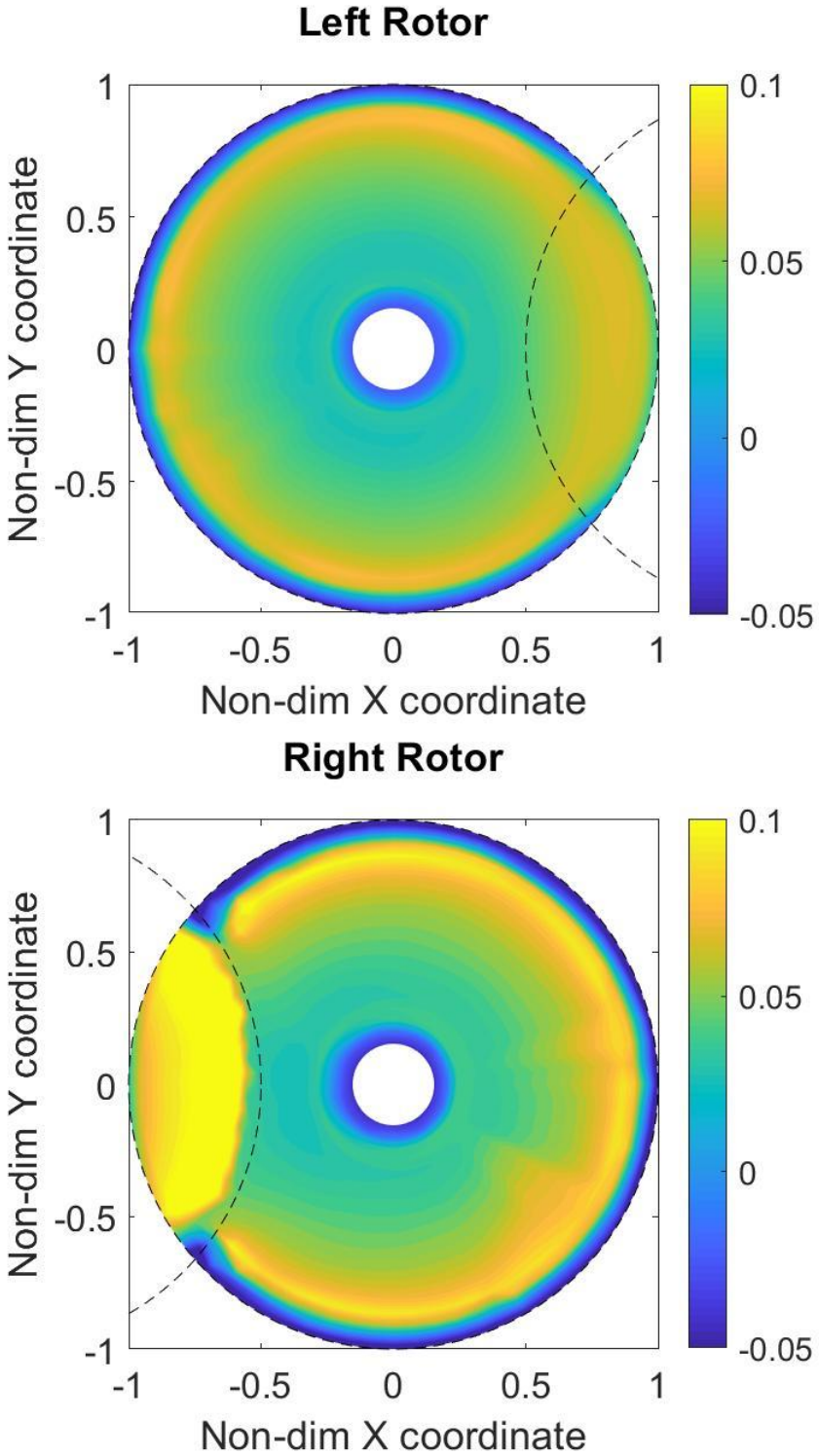

Figure B-13 Induced velocity contour plot on the rotor disk for VS=0.25R, AS=1.50R

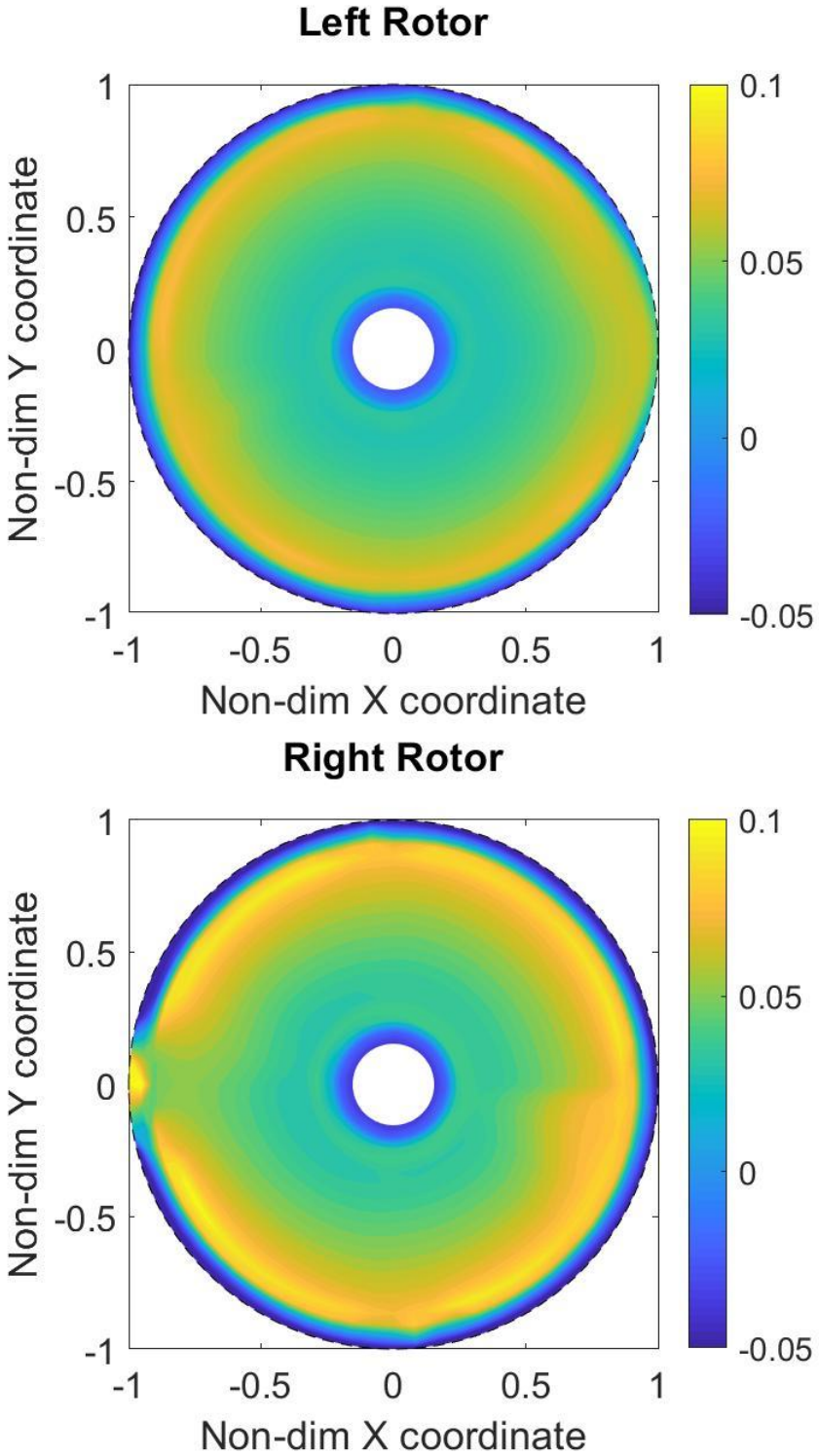

Figure B-14 Induced velocity contour plot on the rotor disk for VS=0.25R, AS=2.00R

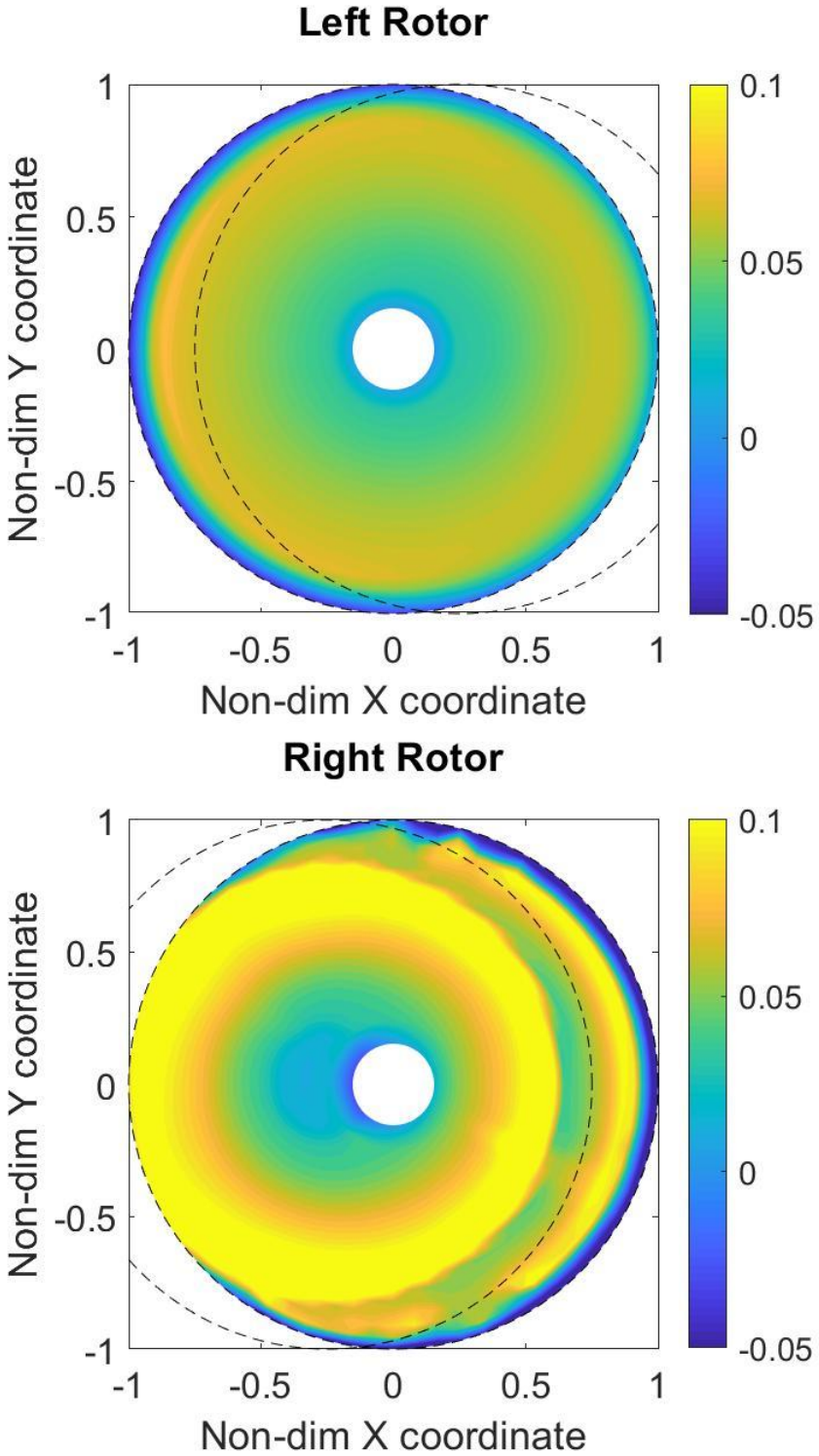

Figure B-15 Induced velocity contour plot on the rotor disk for VS=0.40R, AS=0.25R

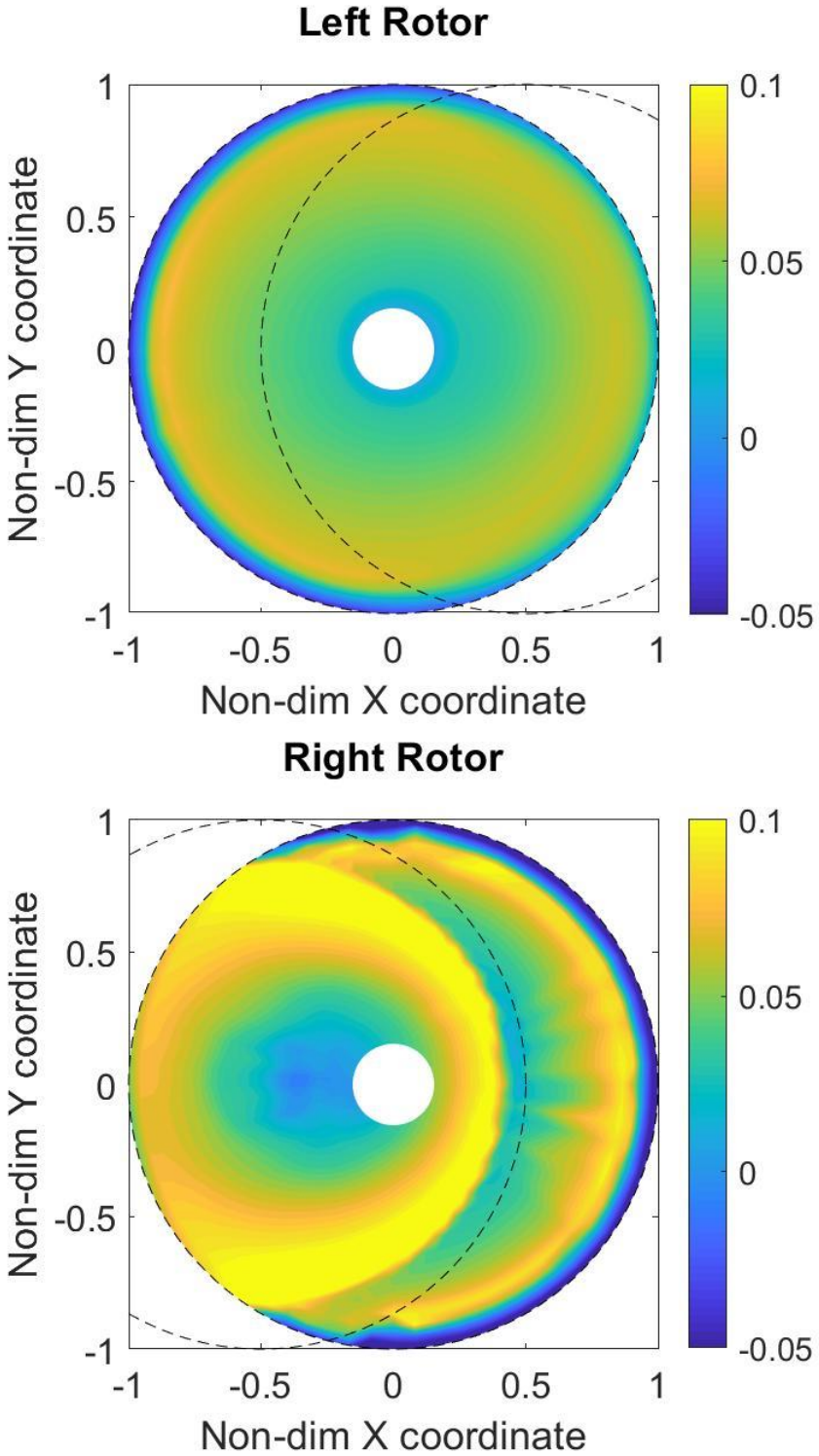

Figure B-16 Induced velocity contour plot on the rotor disk for VS=0.40R, AS=0.50R

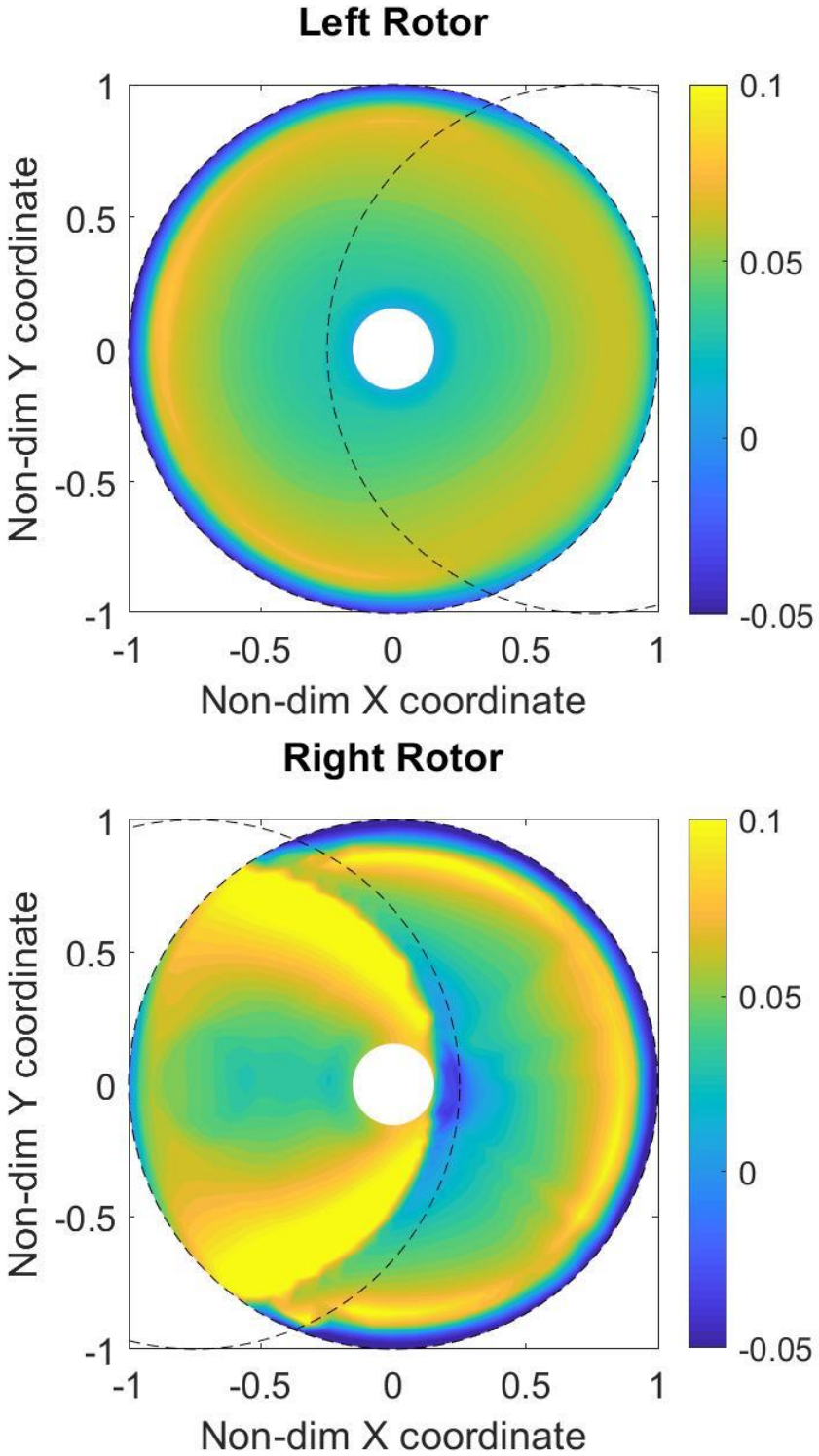

Figure B-17 Induced velocity contour plot on the rotor disk for VS=0.40R, AS=0.75R

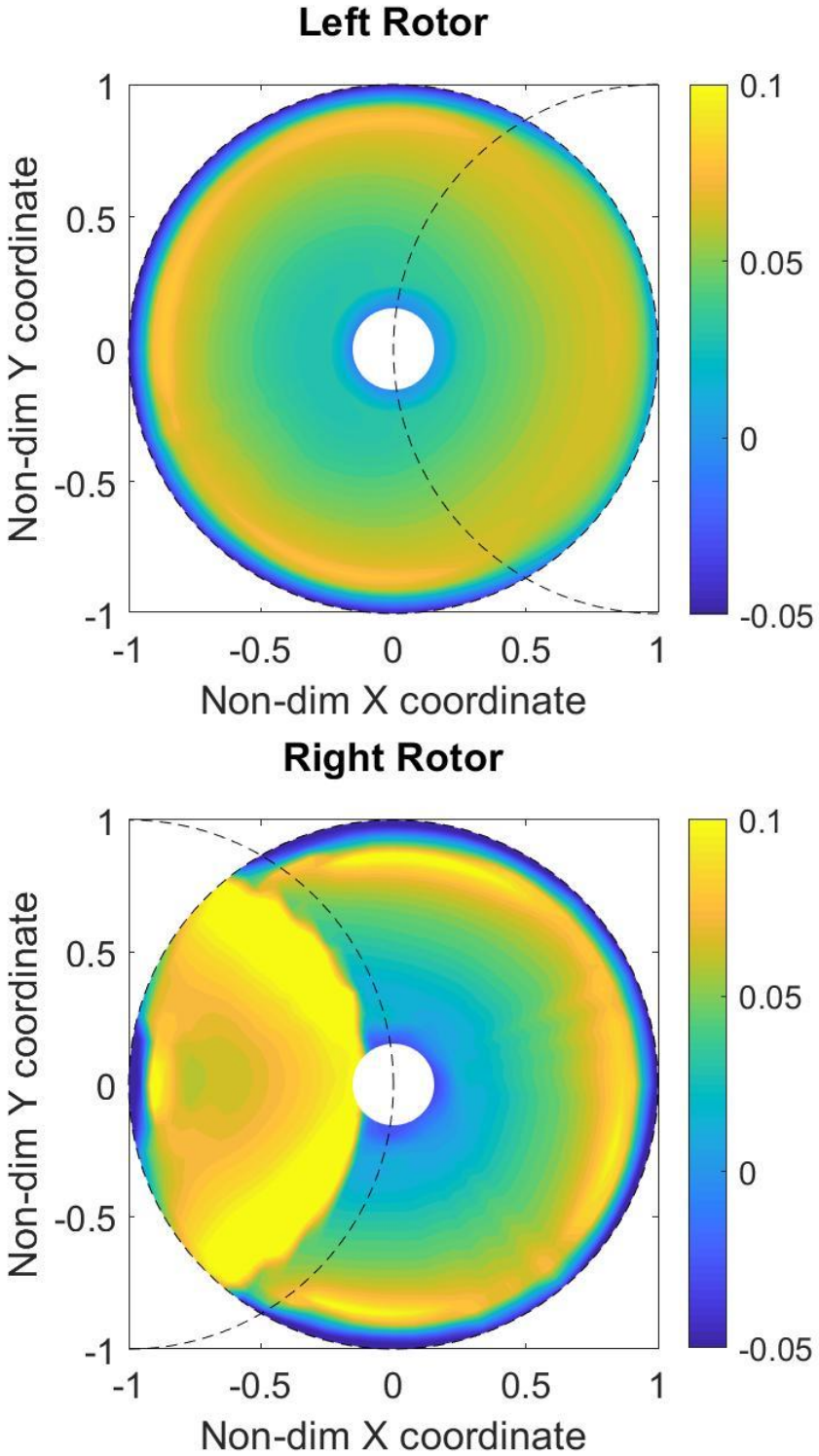

Figure B-18 Induced velocity contour plot on the rotor disk for VS=0.40R, AS=1.00R

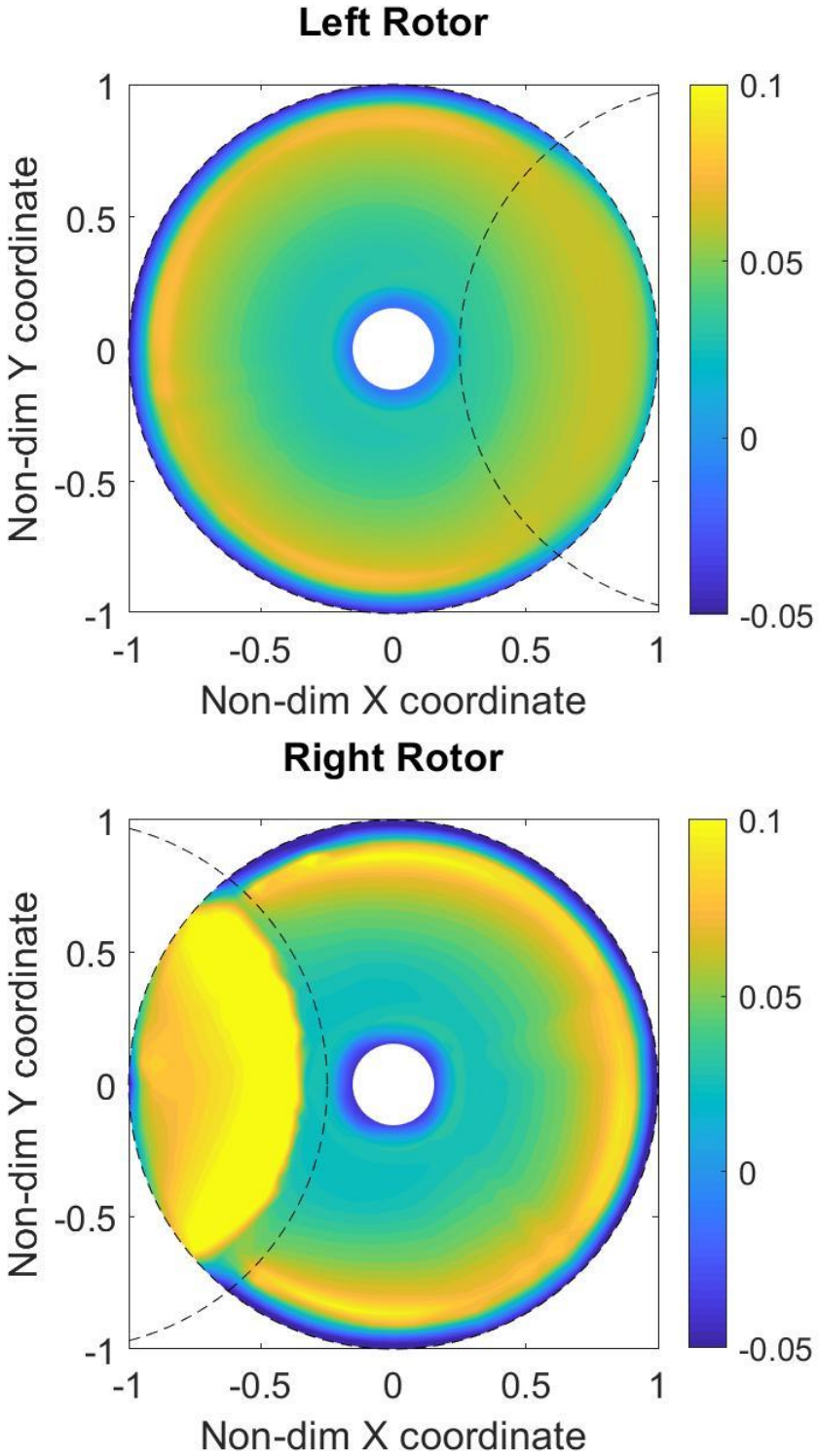

Figure B-19 Induced velocity contour plot on the rotor disk for VS=0.40R, AS=1.25R

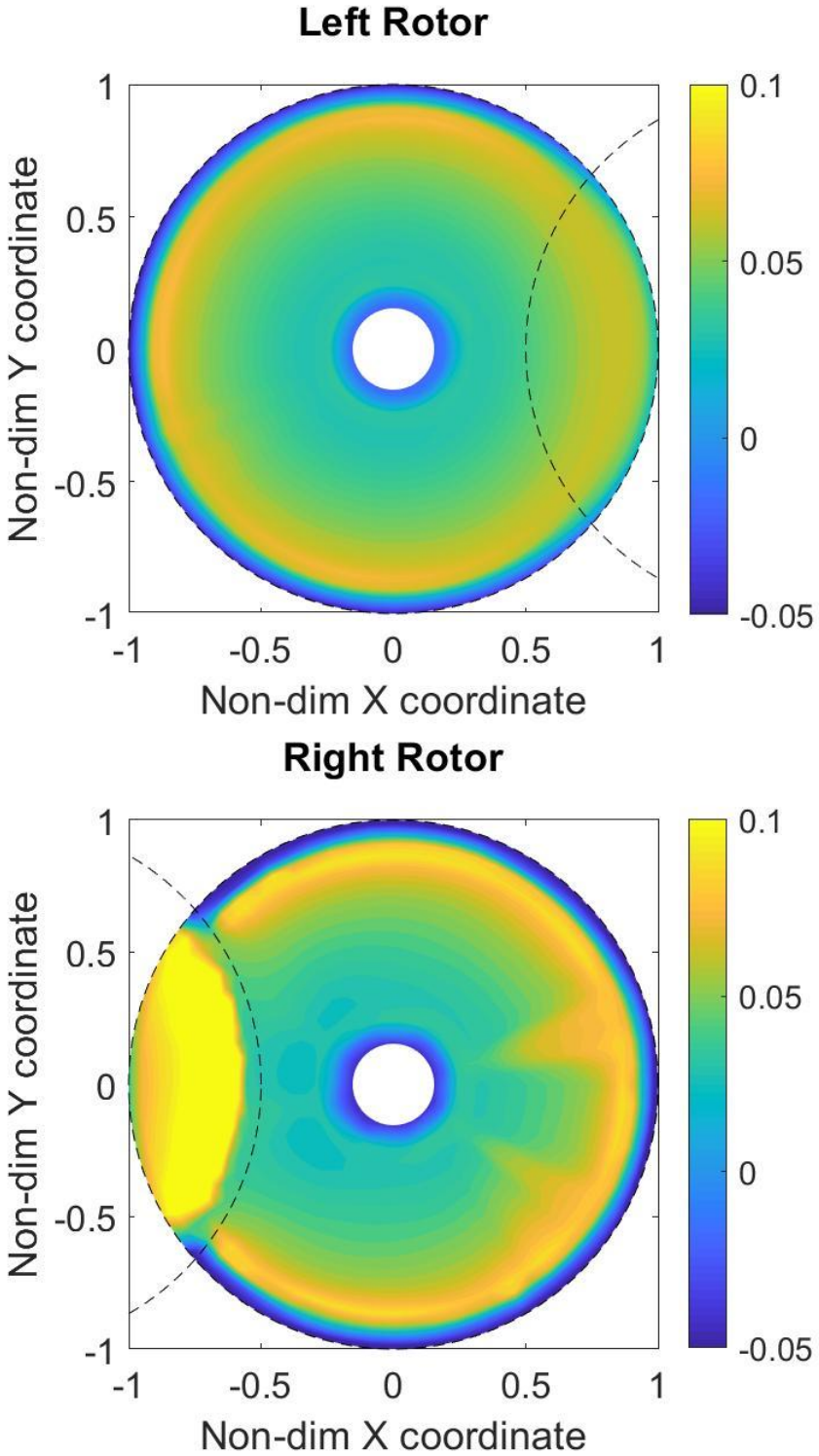

Figure B-20 Induced velocity contour plot on the rotor disk for VS=0.40R, AS=1.50R

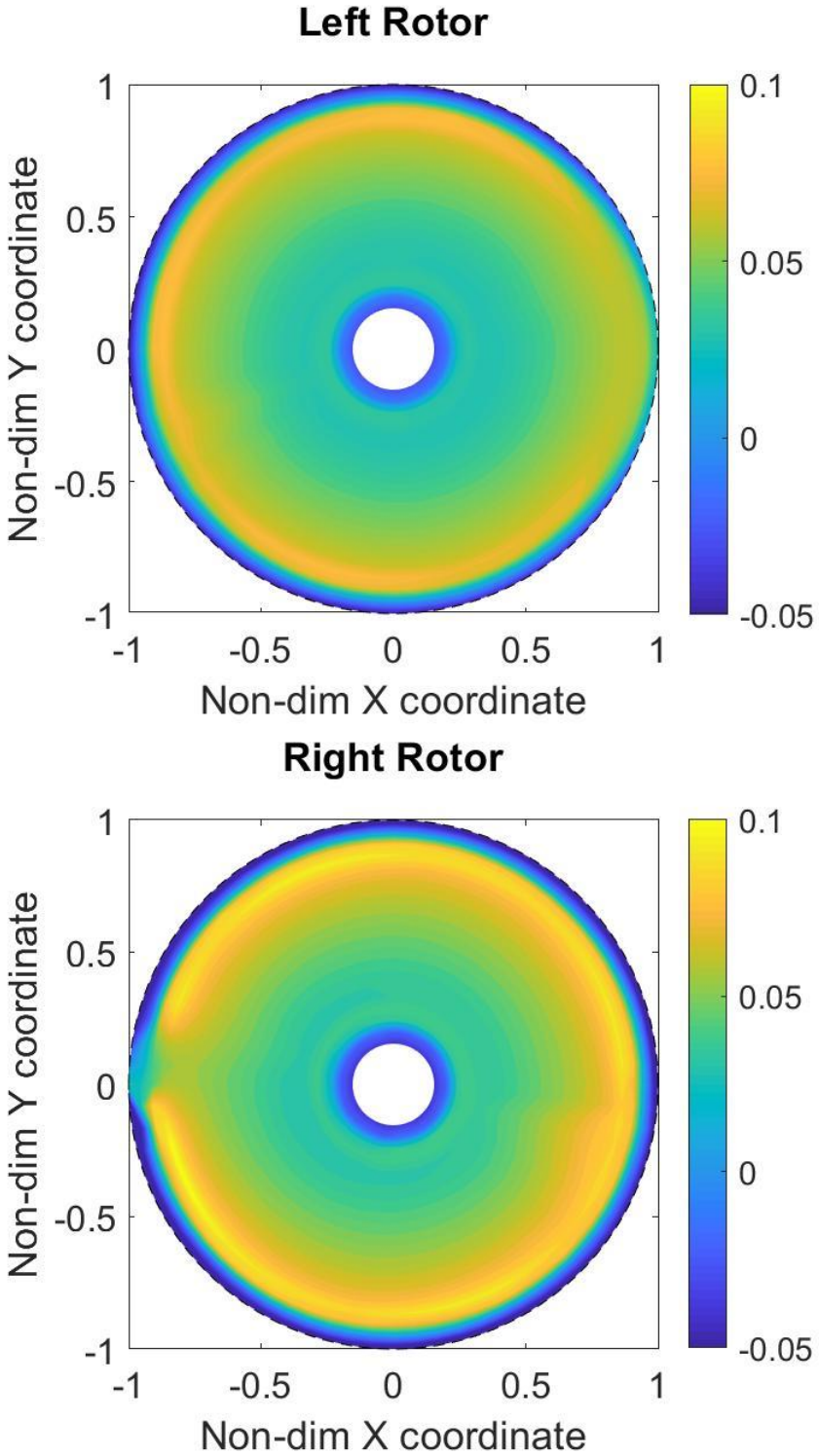

Figure B-21 Induced velocity contour plot on the rotor disk for VS=0.40R, AS=2.00R

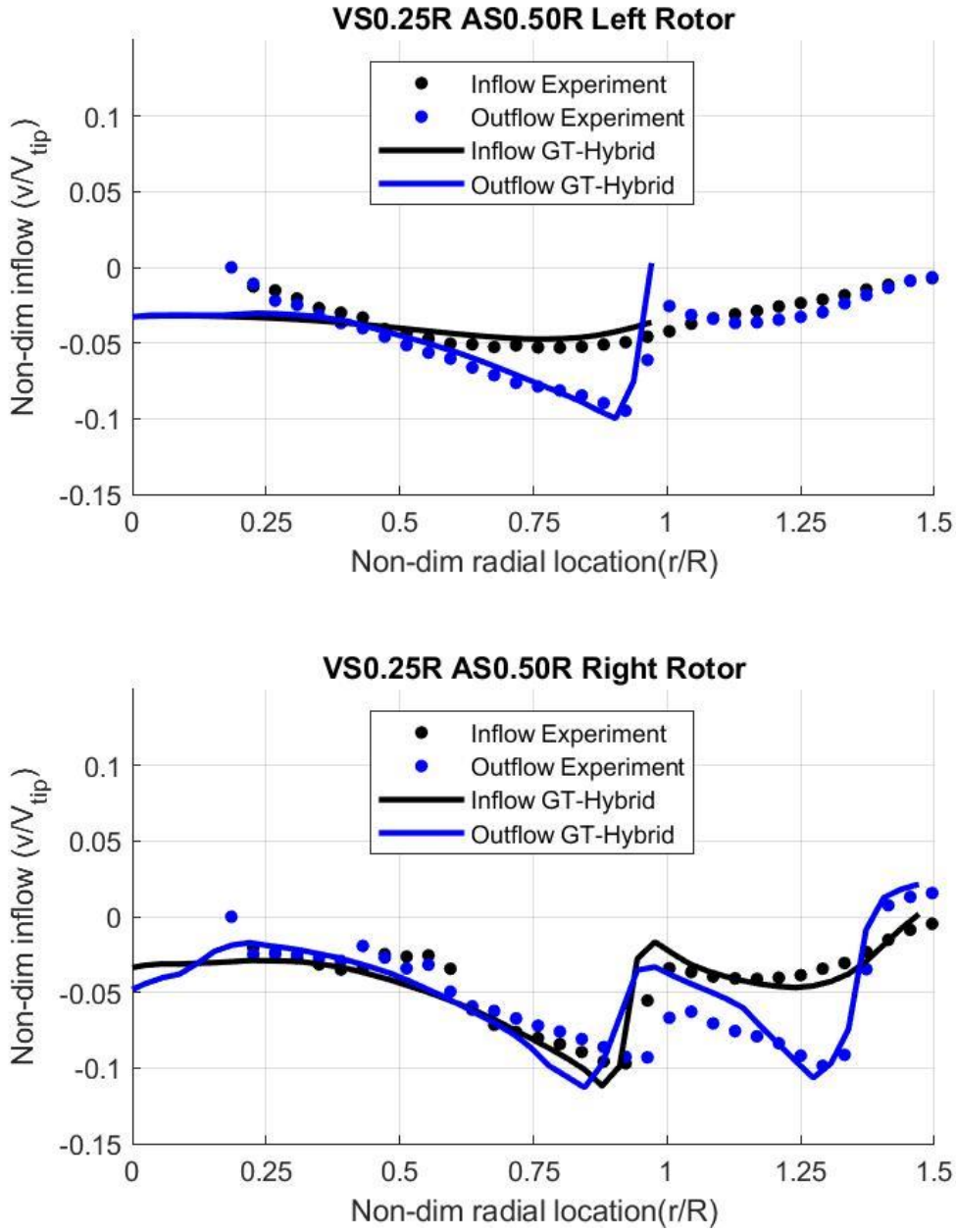

Figure B-22 Sectional induced velocity distribution plot for VS=0.25R, AS=0.50R

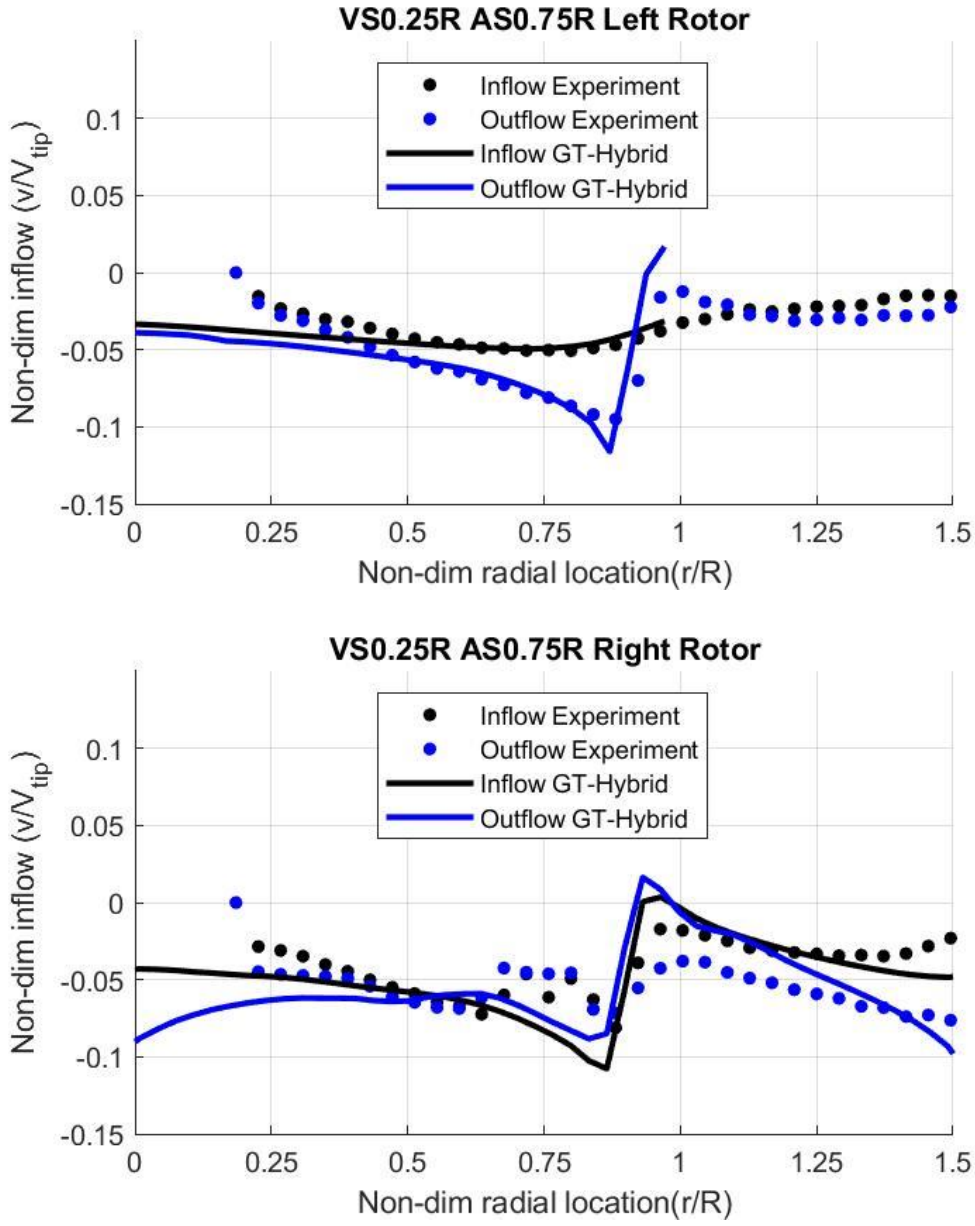

Figure B-23 Sectional induced velocity distribution plot for VS=0.25R, AS=0.75R

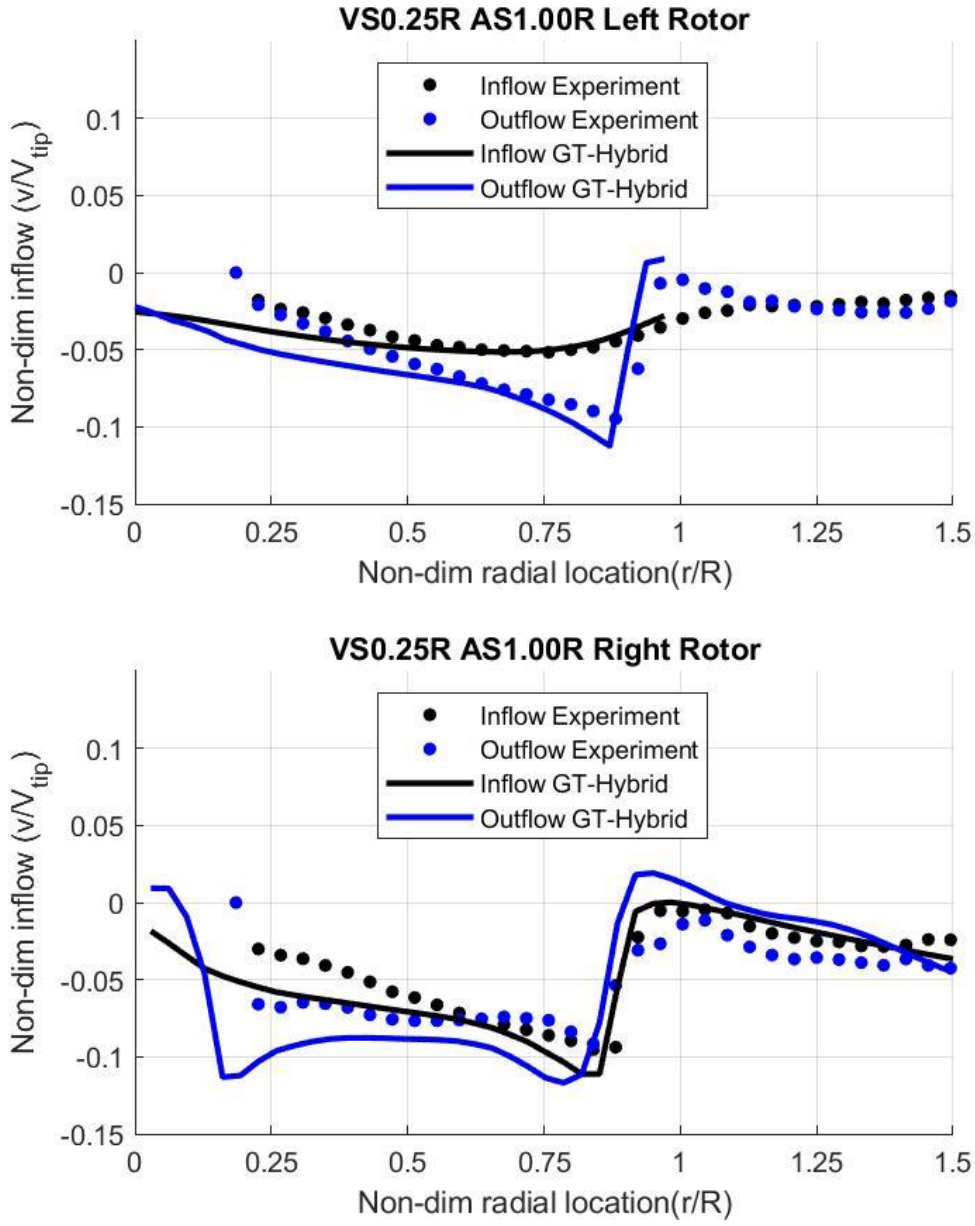

Figure B-24 Sectional induced velocity distribution plot for VS=0.25R, AS=1.00R

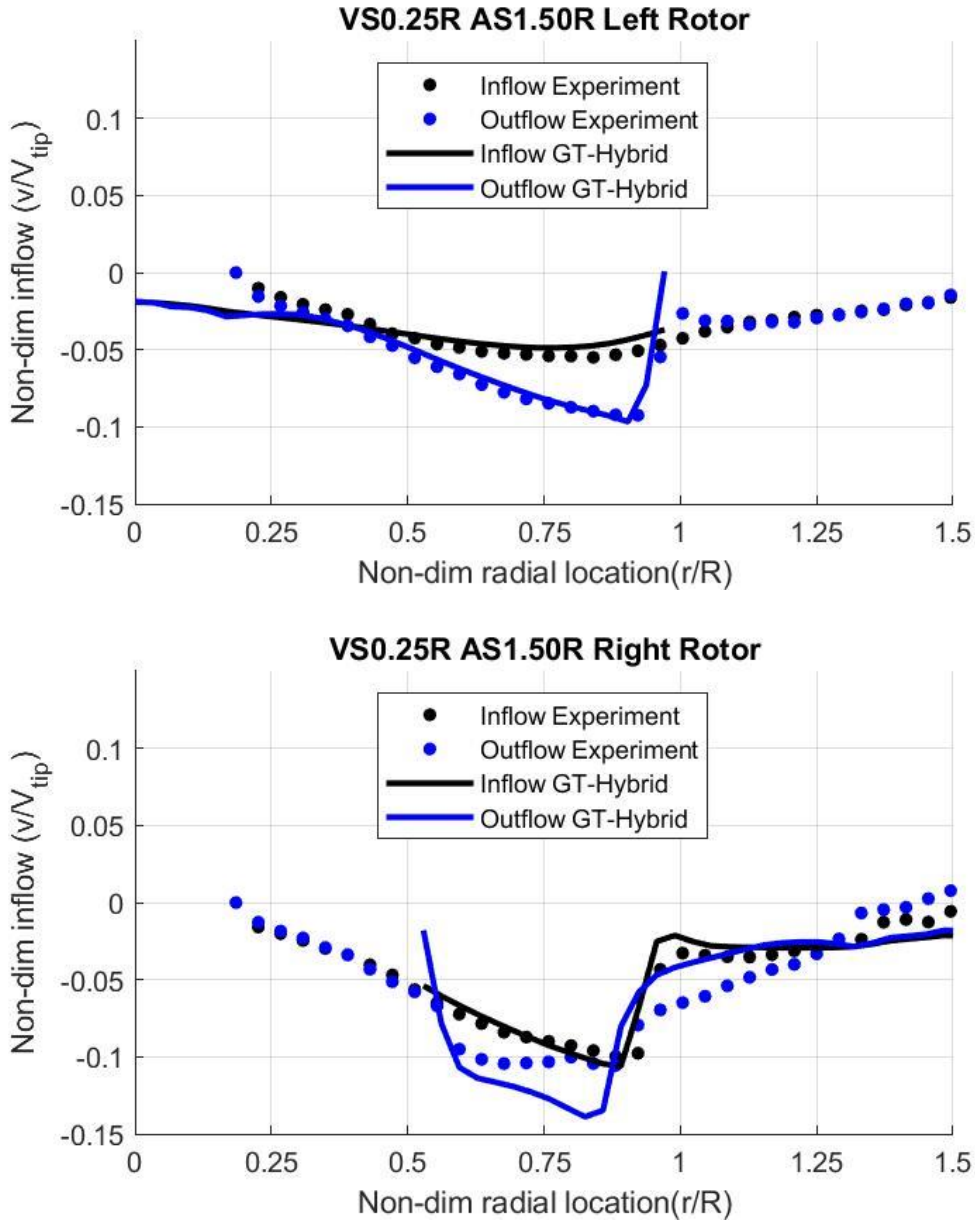

Figure B-25 Sectional induced velocity distribution plot for VS=0.25R, AS=1.5R

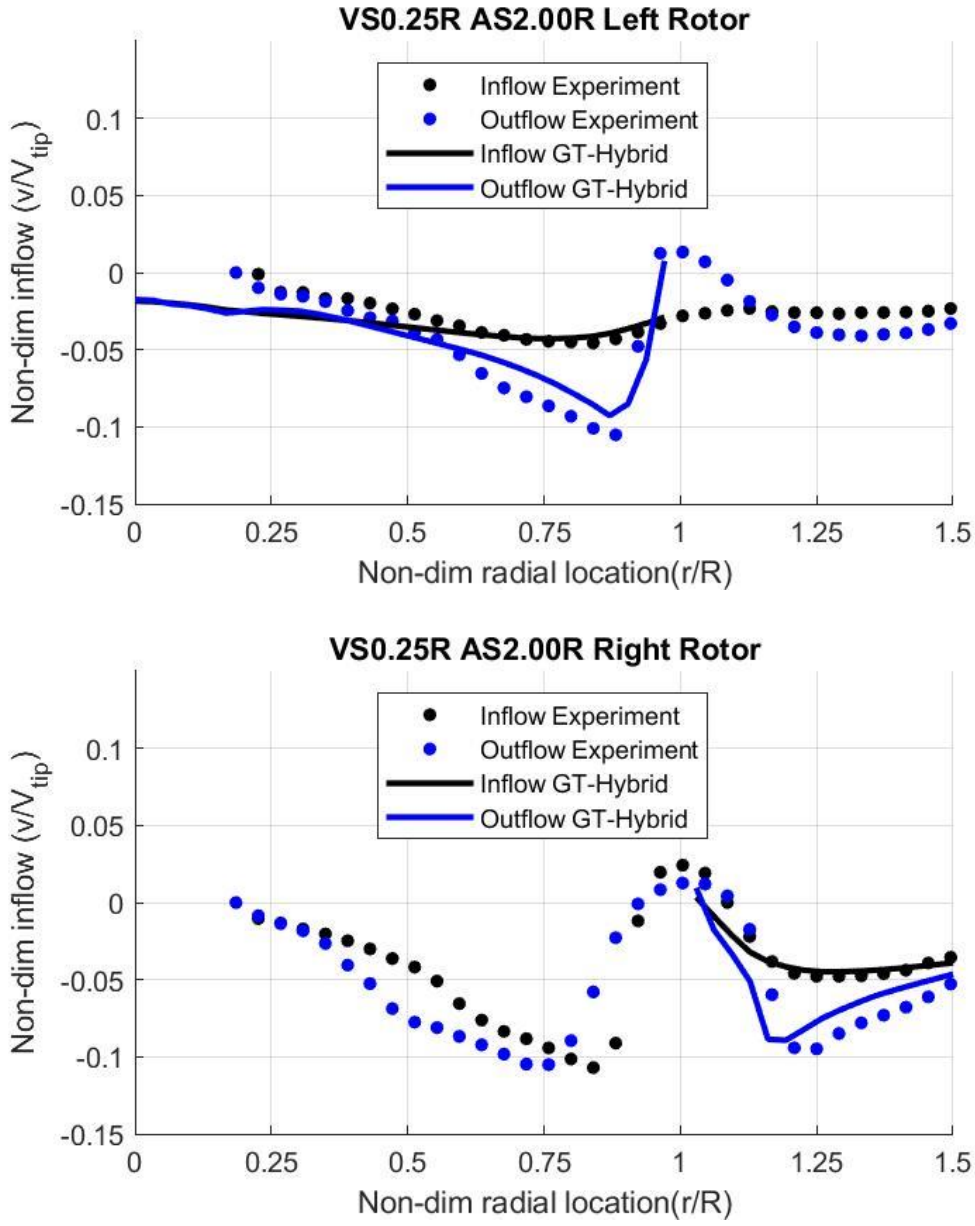

Figure B-26 Sectional induced velocity distribution plot for VS=0.25R, AS=2.00R

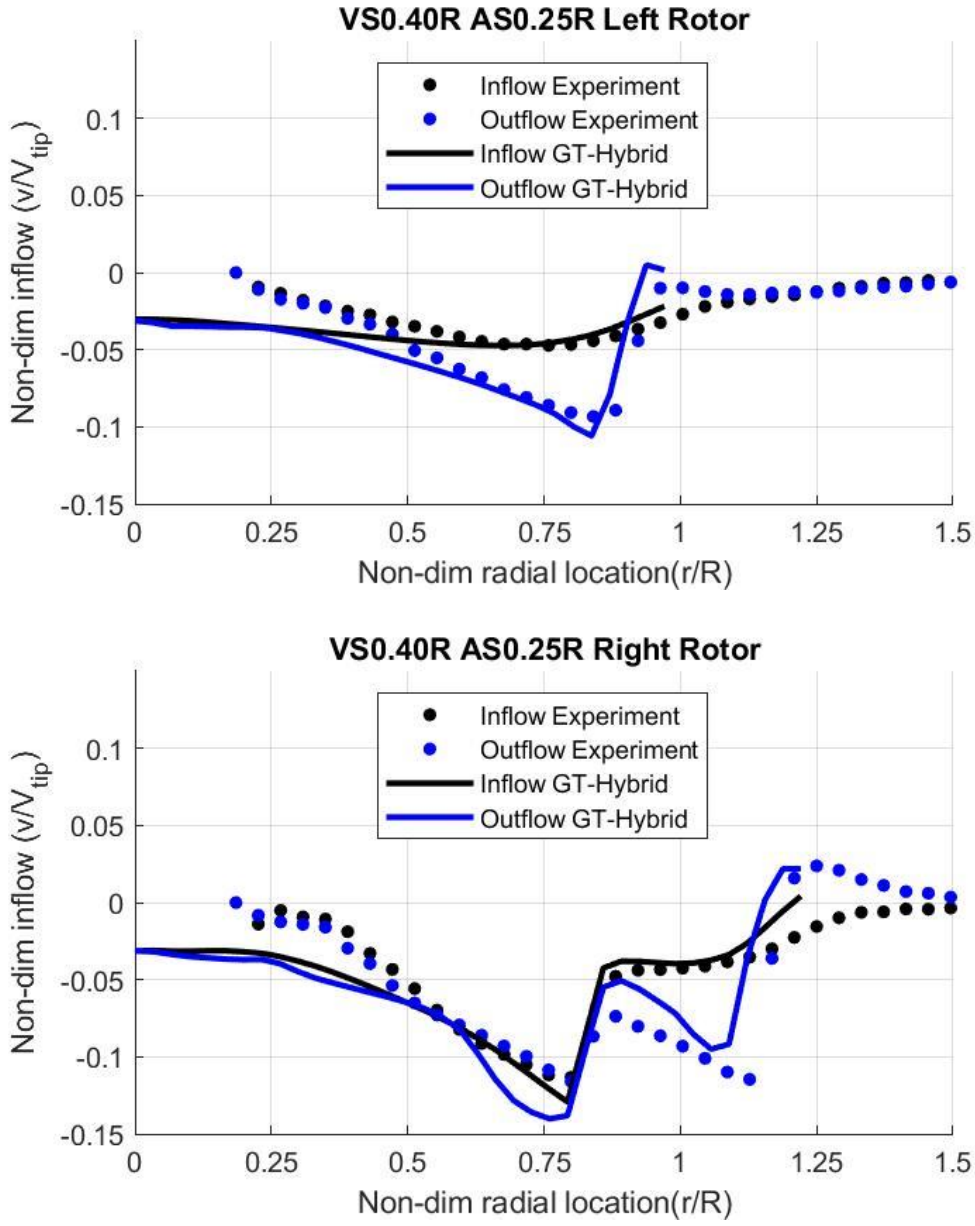

Figure B-27 Sectional induced velocity distribution plot for VS=0.40R, AS=0.25R

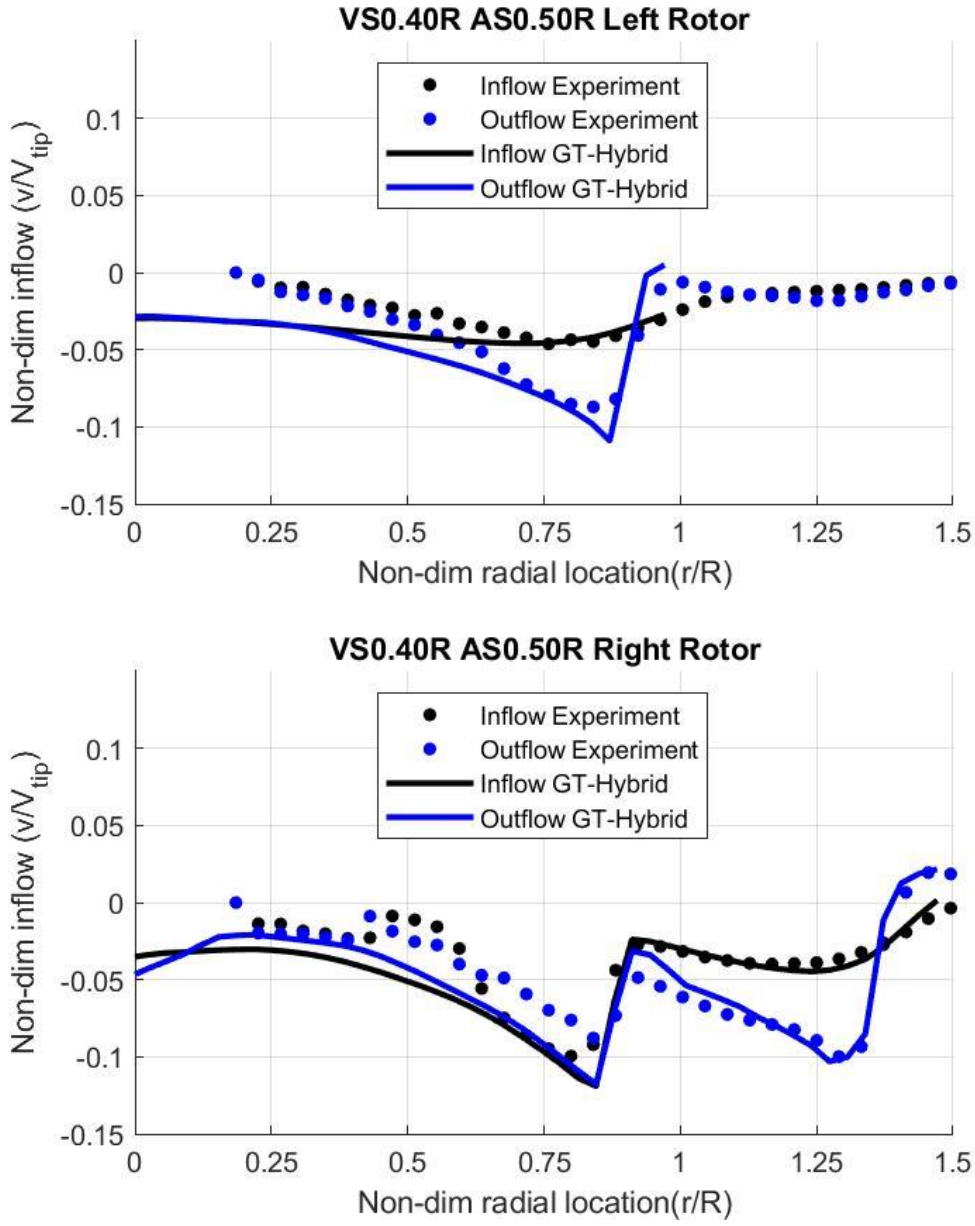

Figure B-28 Sectional induced velocity distribution plot for VS=0.40R, AS=0.50R

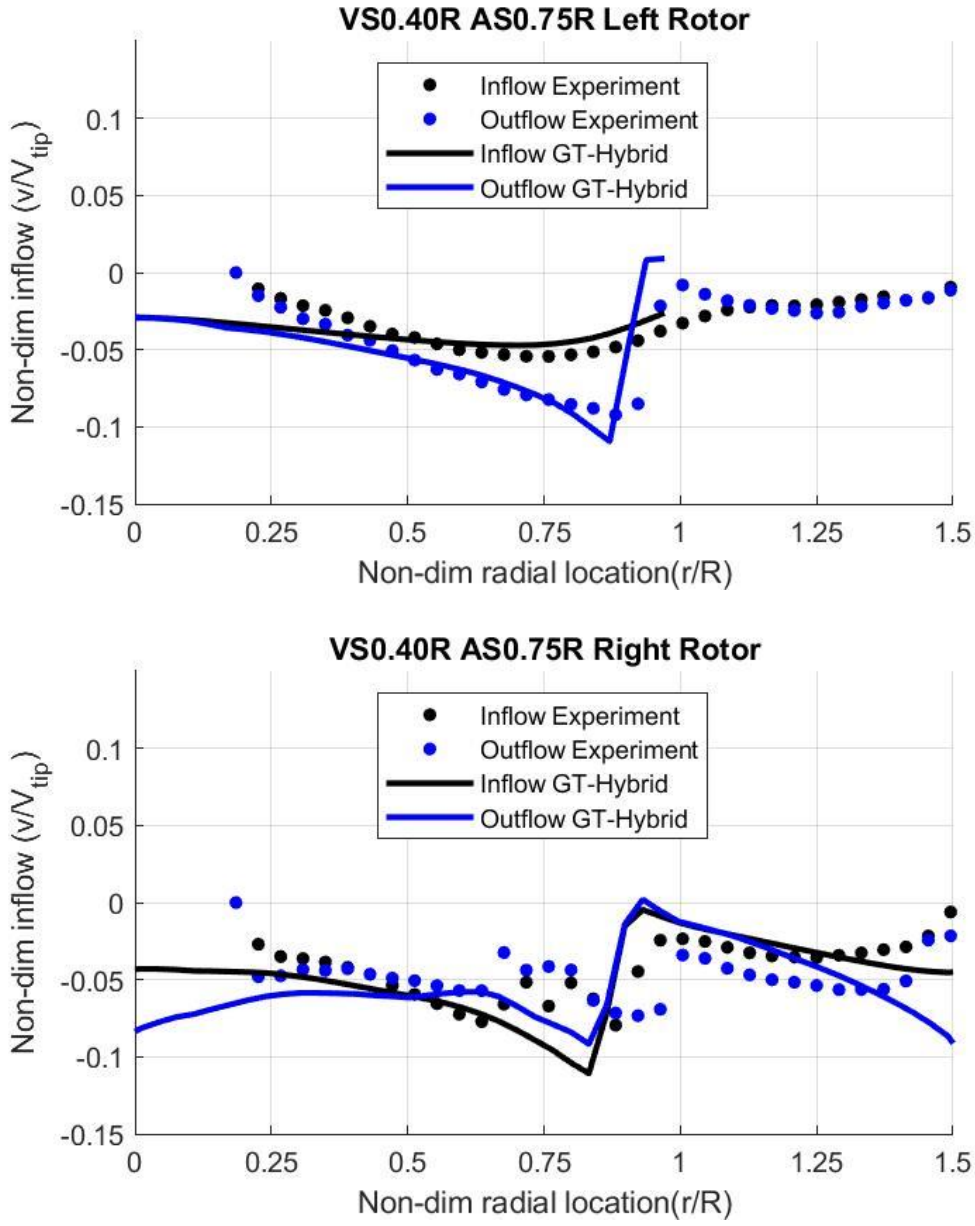

Figure B-29 Sectional induced velocity distribution plot for VS=0.40R, AS=0.75R

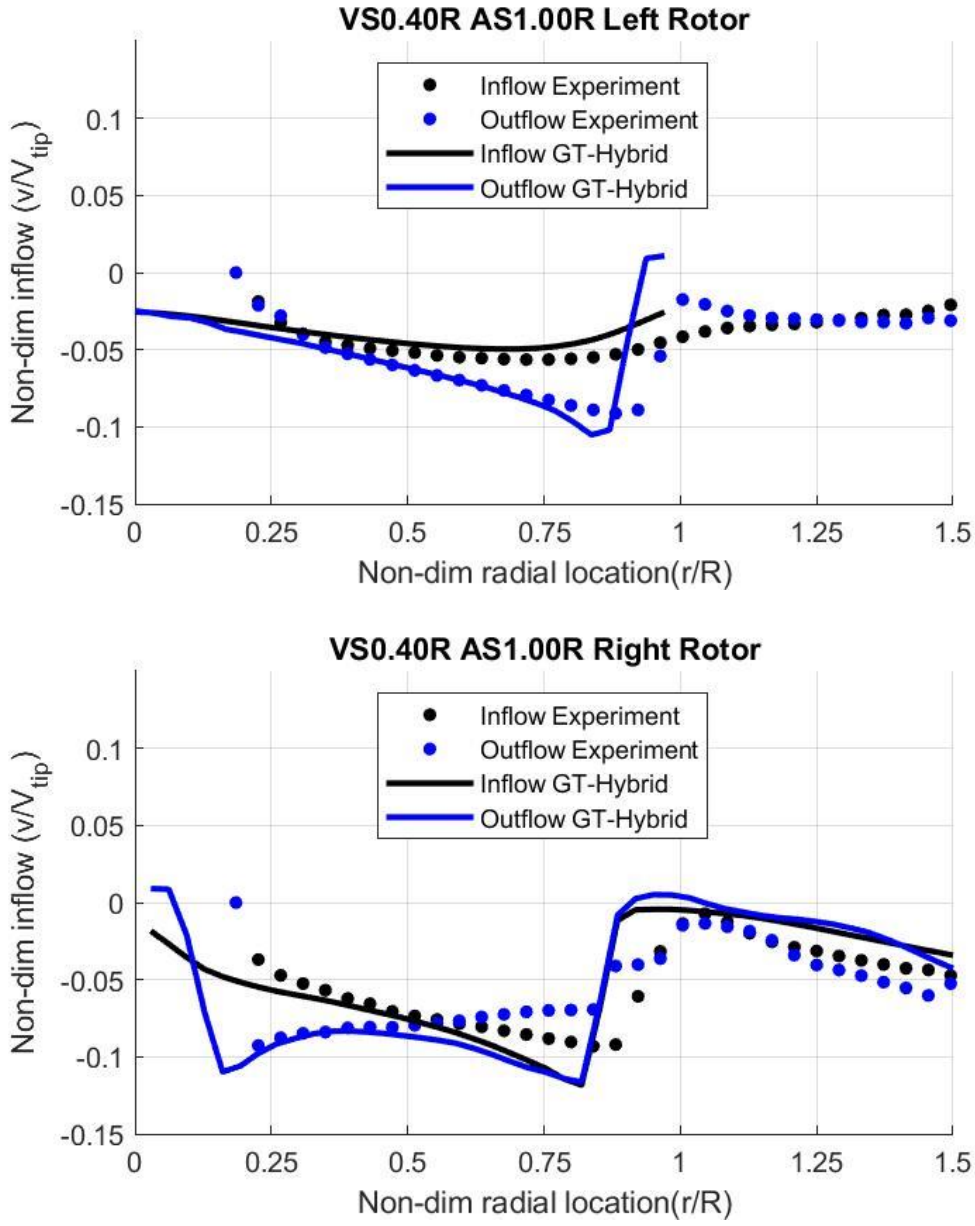

Figure B-30 Sectional induced velocity distribution plot for VS=0.40R, AS=1.00R

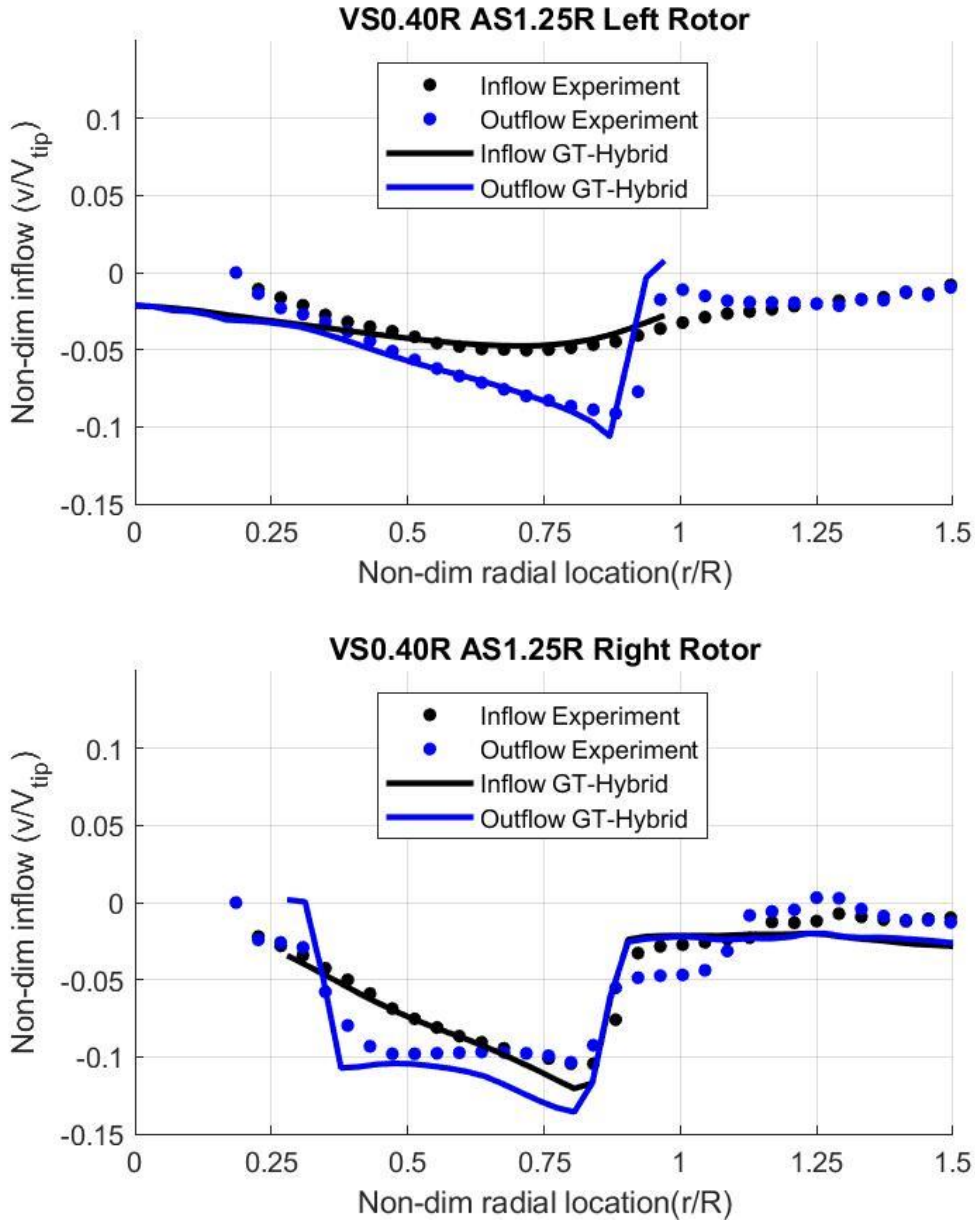

Figure B-31 Sectional induced velocity distribution plot for VS=0.40R, AS=1.25R

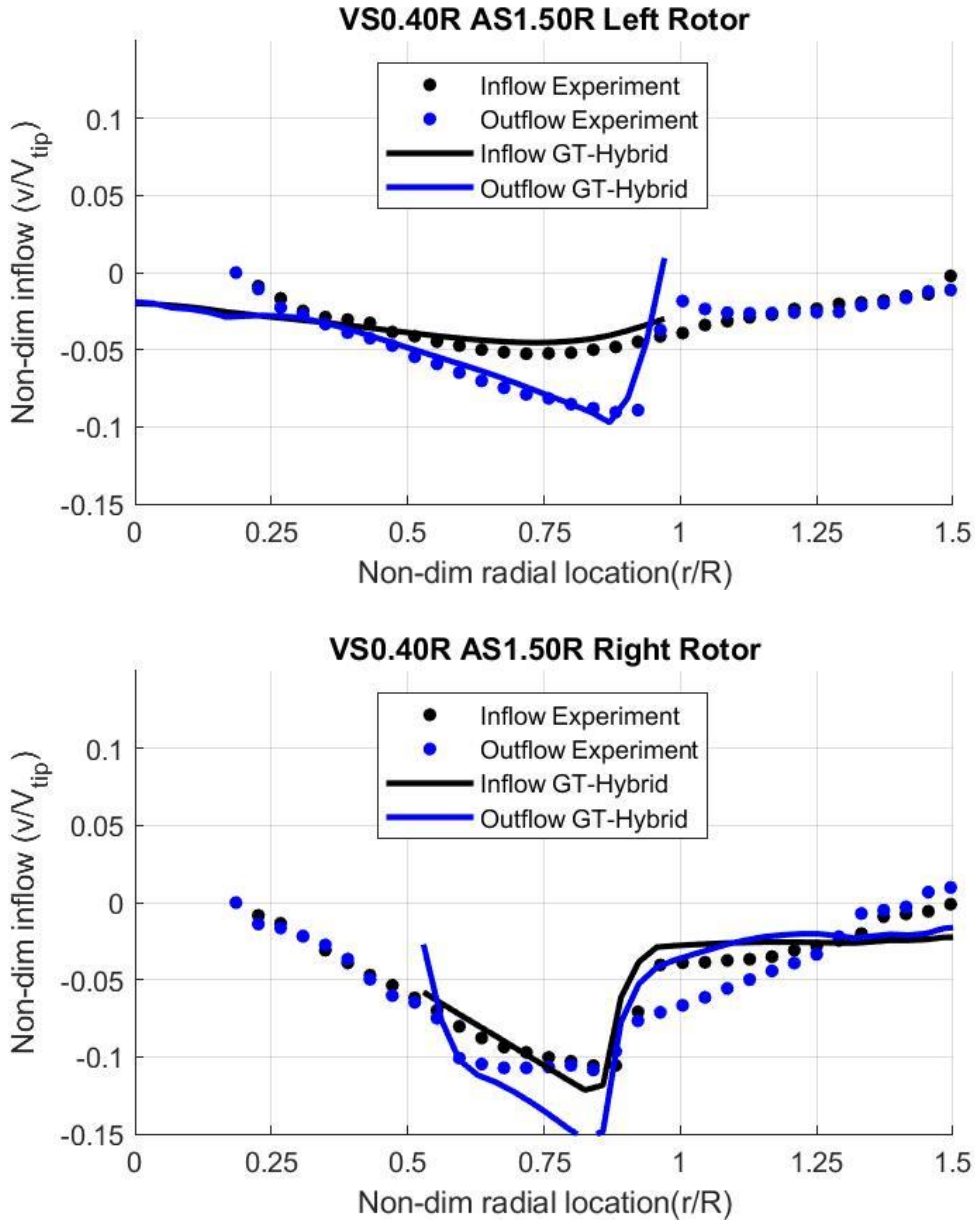

Figure B-32 Sectional induced velocity distribution plot for VS=0.40R, AS=1.50R

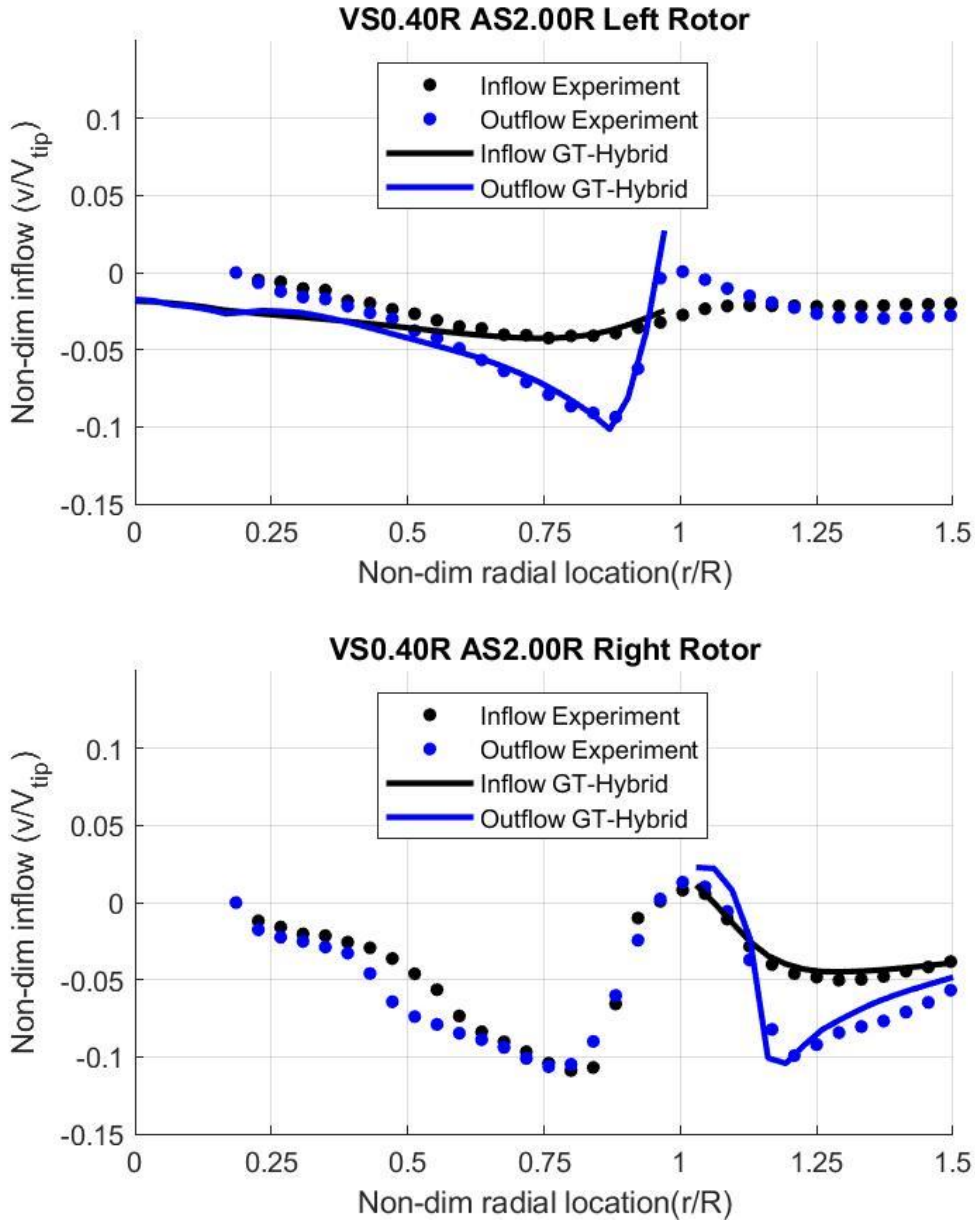

Figure B-33 Sectional induced velocity distribution plot for VS=0.40R, AS=2.00R

APPENDIX C. GPU Architecture

The GPU used in the present study is the NVIDIA GeForce RTX 2060 SUPER with a Turing architecture as shown in Figure C-1 [142]. This graphic card has a PCI Express 3.0×16 interface with a theoretical maximum bandwidth between GPU and CPU of nearly 16GB/s. There are 3 graphics processing clusters (GPC) on the GPU and each GPC has 34 streaming multiprocessors (SM). Two of these SM were disabled, and only 34 SMs were available for use. As shown in Figure C-1, each SM features 64 CUDA cores, responsible for the calculation. In total, this GPU card has a total of 2,176 CUDA cores. With the boost clock rate of 1.68 GHz, the NVIDIA GeForce RTX 2060 SUPER can achieve 7.2 TFLOPS (tera floating-point operations per second).

The memory architecture is as follows. The NVIDIA GeForce RTX 2060 SUPER features 8GB of GDDR6 VRAM and 4MB of L2 cache as shown in Figure C-1. In each SM, the unified shared memory and L1 cache provide a single partitionable memory block with a size of 96KB. While designing the GPU CUDA program, understanding the memory hierarchy of GPU is crucial for fully utilizing the capability of the GPU. More detail of the specification may be found in Figure C-2, generated from a CUDA device query (Runtime API).

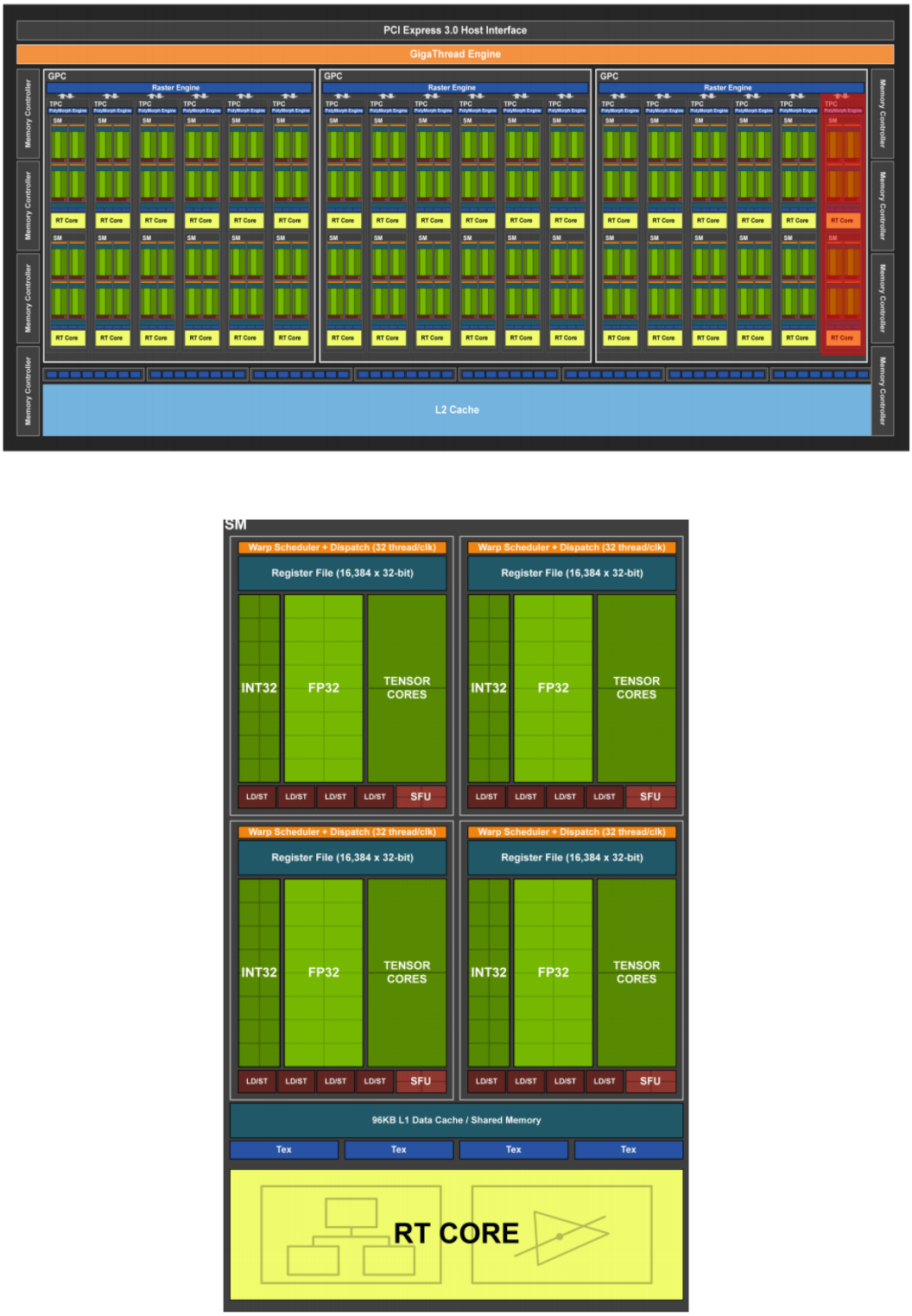

Figure C-1 Turing TU106 full chip diagram and streaming multiprocessor (SM)

```
Device 0: "GeForce RTX 2060 SUPER"
  CUDA Driver Version / Runtime Version          11.2 / 11.2
  CUDA Capability Major/Minor version number:    7.5
  Total amount of global memory:                 8192 MBytes (8589934592 bytes)
  (34) Multiprocessors, ( 64) CUDA Cores/MP:     2176 CUDA Cores
  GPU Max Clock rate:                            1680 MHz (1.68 GHz)
  Memory Clock rate:                             7001 Mhz
  Memory Bus Width:                              256-bit
  L2 Cache Size:                                 4194304 bytes
  Maximum Texture Dimension Size (x,y,z)         1D=(131072), 2D=(131072, 65536), 3D=(16384, 16384, 16384)
  Maximum Layered 1D Texture Size, (num) layers  1D=(32768), 2048 layers
  Maximum Layered 2D Texture Size, (num) layers  2D=(32768, 32768), 2048 layers
  Total amount of constant memory:               65536 bytes
  Total amount of shared memory per block:       49152 bytes
  Total shared memory per multiprocessor:        65536 bytes
  Total number of registers available per block: 65536
  Warp size:                                     32
  Maximum number of threads per multiprocessor:  1024
  Maximum number of threads per block:           1024
  Max dimension size of a thread block (x,y,z): (1024, 1024, 64)
  Max dimension size of a grid size    (x,y,z): (2147483647, 65535, 65535)
  Maximum memory pitch:                          2147483647 bytes
  Texture alignment:                             512 bytes
  Concurrent copy and kernel execution:          Yes with 6 copy engine(s)
  Run time limit on kernels:                     Yes
  Integrated GPU sharing Host Memory:            No
  Support host page-locked memory mapping:       Yes
  Alignment requirement for Surfaces:            Yes
  Device has ECC support:                        Disabled
  CUDA Device Driver Mode (TCC or WDDM):         WDDM (Windows Display Driver Model)
  Device supports Unified Addressing (UVA):      Yes
  Device supports Managed Memory:                Yes
  Device supports Compute Preemption:            Yes
  Supports Cooperative Kernel Launch:            Yes
  Supports MultiDevice Co-op Kernel Launch:      No
  Device PCI Domain ID / Bus ID / location ID:   0 / 9 / 0
  Compute Mode:
     < Default (multiple host threads can use ::cudaSetDevice() with device simultaneously) >

deviceQuery, CUDA Driver = CUDART, CUDA Driver Version = 11.2, CUDA Runtime Version = 11.2, NumDevs = 1
Result = PASS
```

Figure C-2 Device information for NVIDIA GeForce RTX 2060 SUPER

REFERENCES

[1] "Vought-Sikorsky VS-300," Wikipedia, https://en.wikipedia.org/wiki/Vought-Sikorsky_VS-300 (accessed May 7, 2021).

[2] Johnson, W., "Rotorcraft Aerodynamic Models for a Comprehensive Analysis," in *American Helicopter Society 54th Annual Forum*, vol. 54, pp. 71-94. Washington, D.C., May, 1998

[3] Johnson, W., "NDARC-NASA Design and Analysis of Rotorcraft," NASA/TP 2015-218751, April 2015.

[4] Johnson, W., "NDARC-NASA Design and Analysis of Rotorcraft Theoretical Basis and Architecture," in *American Helicopter Society Aeromechanics Specialists Conference*. San Francisco, CA, January 20-22, 2010

[5] Swartz, K. I., "Charging Forward. New eVTOL Concepts Advance," *Vertiflite,* vol. 4, pp. 24-29, 2017.

[6] Johnson, W., Silva, C., and Solis, E., "Concept Vehicles for VTOL Air Taxi Operations," in *AHS Technical Conference on Aeromechanics Design for Transformative Vertical Flight*. San Francisco, CA, January, 2018

[7] Narducci, R. P., Jain, R., Abras, J., and Hariharan, N. S., "HVAB Rotor Hover Computational Prediction: A Comparative Study Using OVERFLOW and HPCMP CREATE™-AV Helios," in *AIAA Scitech 2021 Forum*, p. 0617. January, 2021

[8] He, C., "Development and Application of a Generalized Dynamic Wake Theory for Lifting Rotors," Ph.D. Dissertation, School of Aerospace Engineering, Georgia Institute of Technology, 1989.

[9] Peters, D. A. and He, C., "Correlation of Measured Induced Velocities with a Finite-State Wake Model," *Journal of the American Helicopter Society,* vol. 36, (3), pp. 59-70, 1991, doi: 10.4050/JAHS.36.59.

[10] Morillo, J. A. and Peters, D. A., "Velocity Field above a Rotor Disk by a New Dynamic Inflow Model," *Journal of aircraft,* vol. 39, (5), pp. 731-738, 2002, doi: 10.2514/2.3019.

[11] Prasad, J. V. R., Nowak, M., and Xin, H., "Finite State Inflow Models for a Coaxial Rotor in Hover," in *38th European Rotorcraft Forum*. Amsterdam, The Netherlands, September 4-7, 2012

[12] Nowak, M., Prasad, J. V. R., Xin, H., and Peters, D. A., "A Potential Flow Model for Coaxial Rotors in Forward Flight," in *39th European Rotorcraft Forum*. Moscow, Russia, 2013

[13] Nowak, M., Prasad, J. V. R., and Peters, D. A., "Development of a Finite State Model for a Coaxial Rotor in Forward Flight," in *American Helicopter Society 70th Annual Forum*. Montreal, Quebec, May 20-22, 2014

[14] Kong, Y. B., Prasad, J. V. R., and He, C., "Analysis of a Finite State Coaxial Rotor Inflow Model," in *41st European Rotorcraft Forum*. Munich, Germany, September 1-4, 2015

[15] Kong, Y. B., Prasad, J. V. R., and Peters, D. A., "Analysis of a Finite State Multi-Rotor Dynamic In flow Model," in *43rd European Rotorcraft Forum*. Milan, Italy, 2017

[16] Guner, F., Kong, Y. B., Prasad, J. V. R., Peters, D. A., and He, C., "Development of Finite State Inflow Models for Multi-Rotor Configurations using Analytical Approach," in *74th Annual Forum of the American Helicopter Society*. Phoenix, AZ, May 14-17, 2018

[17] Guner, F., Prasad, J. V. R., Sankar, L. N., Peters, D. A., and He, C., "Correlation of Finite State Multi-rotor Dynamic Inflow Models with a High Fidelity Viscous Vortex Particle Method," in *44th European Rotorcraft Forum*. Delft, The Netherlands, September 18-20, 2018

[18] "Kamov Ka-27," Wikipedia, https://en.wikipedia.org/wiki/Kamov_Ka-27 (accessed May 7, 2021).

[19] "Kamov Ka-50," Wikipedia, https://en.wikipedia.org/wiki/Kamov_Ka-50 (accessed May 7, 2021).

[20] Burgess, R. K., "The ABCTM Rotor—A Historical Perspective," in *American Helicopter Society 60th Annual Forum Proceedings*. Baltimore, MD, June 7–10, 2004

[21] Hirschberg, M., "Sikorsky Pushes Forward with X2 Technology Demonstrator," *Vertiflite*, vol. 51, (3), pp. 12-14, Fall 2005.

[22] Bagai, A., "Aerodynamic Design of the X2 Technology Demonstrator™ Main Rotor Blade," in *American Helicopter Society 64th Annual Forum Proceedings*, vol. 64, (1), p. 29. Montreal, Canada, April 29–May 1, 2008

[23] Blackwell, R. and Millott, T., "Dynamics Design Characteristics of the Sikorsky X2 Technology™ Demonstrator Aircraft," in *American Helicopter Society 64th Annual Forum Proceedings*, vol. 64, (1), p. 886. Montreal, Canada, April 29–May 1, 2008

[24] Coleman, C. P., "A Survey of Theoretical and Experimental Coaxial Rotor Aerodynamic Research," NASA TP 3675, 1997.

[25] McAlister, K. W., Tung, C., Rand, O., Khromov, V., and Wilson, J. S., "Experimental and numerical study of a model coaxial rotor," in *American Helicopter Society 62nd Annual Forum Proceedings*. Phoenix, AZ, May 9–11, 2006

[26] Bagai, A. and Leishman, J. G., "Free-Wake Analysis of Tandem, Tilt-Rotor and Coaxial Rotor Configurations," *Journal of the American Helicopter Society,* vol. 41, (3), pp. 196-207, 1996, doi: 10.4050/JAHS.41.196.

[27] Lim, J. W., McAlister, K. W., and Johnson, W., "Hover Performance Correlation for Full-Scale and Model-Scale Coaxial Rotors," *Journal of the American Helicopter Society,* vol. 54, (3), pp. 32005-32005, 2009, doi: 10.4050/JAHS.54.032005.

[28] Wachspress, D. A. and Quackenbush, T. R., "Impact of Rotor Design on Coaxial Rotor Performance, Wake Geometry and Noise," in *American Helicopter Society 62nd Annual Forum Proceedings,* vol. 62, (1), p. 41. Phoenix, AZ, May 9–11, 2006

[29] Ho, J. C., Yeo, H., and Bhagwat, M., "Validation of Rotorcraft Comprehensive Analysis Performance Predictions for Coaxial Rotors in Hover," *Journal of the American Helicopter Society,* vol. 62, (2), pp. 1-13, 2017, doi: 10.4050/JAHS.62.022005.

[30] Schmaus, J. and Chopra, I., "Aeromechanics for a High Advance Ratio Coaxial Helicopter," in *American Helicopter Society 71st Annual Forum*. Virginia Beach, VA, May 4-7, 2015

[31] Schmaus, J. and Chopra, I., "Performance and Loads Prediction for a High Advance Ratio Coaxial Rotor," in *56th AIAA/ASCE/AHS/ASC Structures, Structural Dynamics, and Materials Conference*, p. 1413. Kissimmee, FL, January 5-9, 2015

[32] Kim, H. W. and Brown, R. E., "A Comparison of Coaxial and Conventional Rotor Performance," *Journal of the American Helicopter Society,* vol. 55, (1), pp. 12004-12004, 2010, doi: 10.4050/JAHS.55.012004.

[33] Kim, H. W., Duraisamy, K., and Brown, R. E., "Effect of Rotor Stiffness and Lift Offset on the Aeroacoustics of a Coaxial Rotor in Level Flight," in *American Helicopter Society 65th Annual Forum Proceedings*. Grapevine, TX, May 27-29, 2009

[34] Zhao, J. and He, C., "Real-Time Simulation of Coaxial Rotor Configurations with Combined Finite State Dynamic Wake and VPM," in *American Helicopter Society 70th Annual Forum Proceedings*. Montreal, Canada, May 20-22, 2014

[35] Kim, H. W. and Brown, R. E., "Coaxial Rotor Performance and Wake Dynamics in Steady and Maneuvering Flight," in *American Helicopter Society 62nd Annual Forum Proceedings*. Phoenix, AZ, May 9–11, 2006

[36] Ruzicka, G. C. and Strawn, R. C., "Computational Fluid Dynamics Analysis of a Coaxial Rotor Using Overset Grids," in *Proceedings of the AHS Specialists' Conference on Aeromechanics*. San Francisco, CA, January 23–25, 2008

[37] Lakshminarayan, V. K. and Baeder, J. D., "High-Resolution Computational Investigation of Trimmed Coaxial Rotor Aerodynamics in Hover," in *Proceedings of the AHS International Specialists Conference on Aeromechanics*. San Francisco, CA, January, 2008

[38] Egolf, T. A., Rajmohan, N., Reed, E., and Sankar, L. N., "A Hybrid CFD Method for Coaxial Rotor Performance Prediction in Forward Flight," in *Proceedings of the AHS Aeromechanics Specialist's Conference*. San Francisco, CA, January, 2010

[39] Lakshminarayan, V. K. and Baeder, J. D., "High-Resolution Computational Investigation of Trimmed Coaxial Rotor Aerodynamics in Hover," *Journal of the American Helicopter Society,* vol. 54, (4), pp. 42008-42008, 2009, doi: 10.4050/JAHS.54.042008.

[40] Lakshminarayan, V. K. and Baeder, J. D., "Computational Investigation of Microscale Coaxial-Rotor Aerodynamics in Hover," *Journal of aircraft,* vol. 47, (3), pp. 940-955, 2010, doi: 10.2514/1.46530.

[41] Juhasz, O., Syal, M., Celi, R., Khromov, V., Rand, O., Ruzicka, G. C., and Strawn, R. C., "Comparison of Three Coaxial Aerodynamic Prediction Methods Including Validation with Model Test Data," *Journal of the American Helicopter Society,* vol. 59, (3), pp. 1-14, 2014, doi: 10.4050/JAHS.59.032006.

[42] Singh, R., Kang, H., and Sirohi, J., "Computational Investigations of Transient Loads and Blade Deformations on Coaxial Rotor Systems," in *33rd AIAA Applied Aerodynamics Conference*, p. 2884. Dallas, TX, June 22-26, 2015

[43] Barbely, N. L., Komerath, N. M., and Novak, L. A., "A Study of Coaxial Rotor Performance and Flow Field Characteristics," in *The 2016 AHS Technical Meeting on Aeromechanics Design for Vertical Lift*. San Francisco, CA, January 20–22, 2016

[44] Marpu, R. P., Sankar, L. N., Makinen, S. M., Egolf, T. A., Baeder, J. D., and Wasikowski, M., "Physics-Based Modeling of Maneuver Loads for Rotor and Hub Design," *Journal of Aircraft,* vol. 51, (2), pp. 377-389, 2014, doi: 10.2514/1.C031843.

[45] Kim, J., Sankar, L. N., and Prasad, J. V. R., "Application of a Navier-Stokes Free Wake Hybrid Methodology to the Harrington Coaxial Rotor," in *American Helicopter Society Specialists Conference on Aeromechanics Design for Vertical Lift*, pp. 1-7. San Francisco, CA, January 20-22, 2016

[46] Harrington, R. D., "Full-Scale-Tunnel Investigation of the Static-Thrust Performance of a Coaxial Helicopter Rotor," NACA-TN-2318, March 1951.

[47] "Boeing CH-47 Chinook," Wikipedia, https://en.wikipedia.org/wiki/Boeing_CH-47_Chinook (accessed May 7, 2021).

[48] Stepniewski, W. Z. and Keys, C. N., "Rotary-Wing Aerodynamics." Dover, New York, 1984.

[49] Dingeldein, R. C., "Wind-Tunnel Studies of the Performance of Multirotor Configurations," NACA-TN-3236, 1954.

[50] Sweet, G. E., "Hovering Measurements for Twin-Rotor Configurations with and without Overlap," NASA-TN-D-534, 1960.

[51] Huston, R. J., "Wind-tunnel Measurements of Performance, Blade Motions, and Blade Air Loads for Tandem-Rotor Configurations With and Without Overlap," NASA-TN-D-1971, 1963.

[52] Ramasamy, M., "Hover Performance Measurements Toward Understanding Aerodynamic Interference in Coaxial, Tandem, and Tilt Rotors," *Journal of the American Helicopter Society,* vol. 60, (3), pp. 1-17, 2015, doi: 10.4050/JAHS.60.032005.

[53] Yeo, H. and Johnson, W., "Aeromechanics Analysis of a Heavy Lift Slowed-Rotor Compound Helicopter," *Journal of Aircraft,* vol. 44, (2), pp. 501-508, March-April 2007.

[54] Lee, J., Yee, K., and Oh, S., "Numerical Investigation of Dual Rotors Using a Time-Marching Free-Wake Method," in *American Helicopter Society 64th Annual Forum*, vol. 64, (1), p. 71. Montreal, Canada, May, 2008

[55] Lee, J.-W., Oh, S.-J., Yee, K.-J., and Kim, D.-K., "Numerical Investigation on Overlap Effects of Tandem Rotors in Forward Flight," *International Journal of Aeronautical and Space Sciences,* vol. 10, (2), pp. 63-76, 2009, doi: 10.5139/IJASS.2009.10.2.063.

[56] Griffiths, D. A. and Leishman, J. G., "A Study of Dual-Rotor Interference and Ground Effect Using a Free-Vortex Wake Model," in *American Helicopter Society 58th Annual Forum*. Montreal, Canada, June 11-13, 2002

[57] Dimanlig, A. C., Saberi, H.-A., Meadowcroft, E. T., Strawn, R., and Bagwhat, M., "Multidisciplinary Modeling of the CH-47 Helicopter with CFD/CSD Coupling and Trim," in *2008 DoD HPCMP Users Group Conference*: IEEE, pp. 143-149. Seattle, WA, July 14-17, 2008

[58] Meadowcroft, E. T. and Jain, R., “Improvements to Tandem-Rotor CH-47 Helicopter Coupled CFD-CSD Full Aircraft Model,” in *American Helicopter Society 72nd Annual Forum*. West Palm Beach, Florida, 2016

[59] Shukla, D. and Komerath, N., “Low Reynolds Number Multirotor Aerodynamic Wake Interactions,” *Experiments in Fluids,* vol. 60, (4), p. 77, 2019, doi: 10.1007/s00348-019-2724-3.

[60] Shukla, D. and Komerath, N., “Multirotor Drone Aerodynamic Interaction Investigation,” *Drones,* vol. 2, (4), p. 43, 2018, doi: 10.3390/drones2 040043.

[61] Shukla, D. and Komerath, N., “Drone Scale Coaxial Rotor Aerodynamic Interactions Investigation,” *Journal of Fluids Engineering,* vol. 141, (7), 2019, doi: 10.1115/1.4042162.

[62] Shukla, D., "Experimental Study of Low Reynolds Number Multiple rotor Interactions," Ph.D. Dissertation, School of Aerospace Engineering, Georgia Institute of Technology, 2019.

[63] Shukla, D., Hiremath, N., and Komerath, N. M., “Low Reynolds Number Aerodynamics Study on Coaxial and Quad-Rotor,” in *2018 Applied Aerodynamics Conference,* p. 4118. 2018

[64] Chen, P.-W., Sankar, L. N., and Prasad, J. V. R., “A Hybrid Navier Stokes-Free Wake Method for Modeling Tandem Rotors,” in *Proceedings of the 7th Asian/Australian Rotorcraft Forum*. Jeju Island, Korea, October 30 - November 1, 2018

[65] Chen, P.-W., Sankar, L. N., and Prasad, J. V. R., “Rotor Wake and Inflow Characteristics of multirotor Drone Configurations,” in *45th European Rotorcraft Forum*. Warsaw, Poland, September 17-20, 2019

[66] Chen, P.-W., Sankar, L. N., Prasad, J. V. R., Schatzman, N. L., and Rajagopalan, R. G., “Extraction of Dynamic Inflow Models for Coaxial and Tandem Rotors from CFD Simulations,” in *Vertical Flight Society's 75th Annual Forum & Technology Display,* pp. 13-16. Philadelphia, PA, May 13-16, 2019

[67] Chen, P.-W., Guner, F., Sankar, L. N., Prasad, J. V. R., and He, C., “Calibration of Velocity Potential Superposition Inflow Model using Computational Fluid Dynamics Data,” *Proceedings of the VFS Aeromechanics for Advanced Vertical Flight,* January 21-23 2020.

[68] Xin, H., Goss, J., and Parkes, C., “Development of a Three-State Rotor Interference Model and Application to Coaxial Rotor Inflow Modeling,” in *Fifth Decennial AHS Aeromechanics Specialists’ Conference*. San Francisco, CA, January, 2014

[69] Rand, O., Khromov, V., Hersey, S., Celi, R., Juhasz, O., and Tischler, M., “Linear Inflow Model Extraction from High-Fidelity Aerodynamic Models for Flight

Dynamics Applications," in *American Helicopter Society 71st Annual Forum*. Virginia Beach, VA, May, 2015

[70] Rand, O. and Khromov, V., "Free-Wake–Based Dynamic Inflow Model for Hover, Forward, and Maneuvering Flight," *Journal of the American Helicopter Society,* vol. 63, (1), pp. 1-16, 2018, doi: 10.4050/JAHS.63.012008.

[71] Rand, O. and Khromov, V., "Parametric Study of Dynamic Inflow for Single and Coaxial Rotor Systems," *Journal of the American Helicopter Society,* vol. 63, (4), pp. 1-14, 2018, doi: 10.4050/JAHS.63.042007.

[72] He, C., Syal, M., Tischler, M. B., and Juhasz, O., "State-Space Inflow Model Identification from Viscous Vortex Particle Method for Advanced Rotorcraft Configurations," in *American Helicopter Society 73rd Annual Forum*. Fort Worth, TX, May, 2017

[73] Prasad, J. V. R., Kong, Y.-B., and Peters, D. A., "Analytical Methods for Modeling Inflow Dynamics of a Coaxial Rotor System," in *Proceedings of the 42nd European Rotorcraft Forum*. Lille, France, September, 2016

[74] Kong, Y.-b., Prasad, J. V. R., Sankar, L. N., and Kim, J., "Finite State Coaxial Rotor Inflow Model Improvements via System Identification," in *American Helicopter Society 72nd Annual Forum*. West Palm Beach, FL, May, 2016

[75] Kong, Y. B., Prasad, J. V. R., and Peters, D. A., "Development of a Finite State Dynamic Inflow Model for Coaxial Rotor using Analytical Methods," in *American Helicopter Society 73rd Annual Forum*. Fort Worth, TX, May, 2017

[76] Guner, F., Prasad, J. V. R., and He, C., "Finite State Multi-Rotor Wake Models Based on Superposition Approaches: PPSIM and VPSIM," in *Proceedings of the 8th Asian/Australian Rotorcraft Forum*. Ankara, Turkey, October 30-November 2, 2019

[77] Guner, F., Prasad, J. V. R., He, C., and Miller, D. G., "Tandem Rotor Inflow Modeling and its Effect on Vehicle Dynamics," in *Vertical Flight Society's 75th Annual Forum & Technology Display*. Philadelphia, PA, May 13-16, 2019

[78] Prasad, J. V. R., Kong, Y.-B., and He, C., "Reduced Order Inflow Models for Multi-Rotor Configurations," in *Proceedings of the 7th Asian/Australian Rotorcraft Forum*. Jeju Island, Korea, October 30 - November 1, 2018

[79] Sankar, L. N. and Tang, W., "Numerical Solution of Unsteady Viscous Flow Past Rotor Sections," in *23rd Aerospace Sciences Meeting*, p. 129. Reno, NV, January 14-17, 1985

[80] Rajagopalan, R. G., Baskaran, V., Hollingsworth, A., Lestari, A., Garrick, D., Solis, E., and Hagerty, B., "RotCFD-A tool for Aerodynamic Interference of Rotors:

Validation and Capabilities," in *Future Vertical Lift Aircraft Design Conference*. San Francisco, CA, January 18-20, 2012

[81] Novak, L. A., Guntupalli, K., and Rajagopalan, R. G., "RotCFD: Advancements in Rotorcraft Modeling and Simulation," in *Proceedings of the 4th Asian-Australian Rotorcraft Forum*. Bangalore, India, November 16-18, 2015

[82] Rajmohan, N., "Application of Hybrid Methodology to Rotors in Steady and Maneuvering Flight," Ph.D. Dissertation, School of Aerospace Engineering, Georgia Institute of Technology, 2010.

[83] Marpu, R., "Physics Based Prediction of Aeromechanical Loads for Uh-60a Rotor," Ph.D. Dissertation, School of Aerospace Engineering, Georgia Institute of Technology, 2013.

[84] Kim, J., "Development of A Physics Based Methodology for the Prediction of Rotor Blade Ice Formation," Ph.D. Dissertation, School of Aerospace Engineering, Georgia Institute of Technology, 2015.

[85] Zhou, C., "Assessment of Tip Planform Effects on the Hover Characteristics of Helicopter Rotors," Ph.D. Dissertation, School of Aerospace Engineering, Georgia Institute of Technology, 2019.

[86] Yeo, H. and Shinoda, P. M., "Investigation of Rotor Loads and Vibration at Transition Speed," in *American Helicopter Society 58th Annual Forum*. Montreal, Canada, June 11-13, 2002

[87] Liou, M.-S. and Steffen Jr, C. J., "A new flux splitting scheme," NASA TM-104404, 1991.

[88] Godunov, S. and Bohachevsky, I., "Finite Difference Method for Numerical Computation of Discontinuous Solutions of the Equations of Fluid Dynamics," *Matematičeskij sbornik,* vol. 47, (3), pp. 271-306, 1959.

[89] Roe, P. L., "The Use of the Riemann Problem in Finite Difference Schemes," in *Seventh International Conference on Numerical Methods in Fluid Dynamics*, vol. 141: Springer, pp. 354-359. New York, 1989

[90] Roe, P. L., "Approximate Riemann Solvers, Parameter Vectors, and Difference Schemes," *Journal of computational physics,* vol. 43, (2), pp. 357-372, 1981.

[91] Roe, P. and Pike, J., "Efficient Construction and Utilisation of Approximate Riemann Solutions," in *Computing Methods in Applied Sciences and Engineering*, pp. 499-518. R. Glowinski and J. L. Lions, eds., North Holland, Amsterdam, 1985

[92] Van Leer, B., "Upwind-Difference Methods for Aerodynamic Problems Governed by the Euler Equations," *Large-scale computations in fluid mechanics,* pp. 327-336, 1985.

[93] Vinokur, M. and Liu, Y., “Equilibrium Gas Flow Computations. II-An Analysis of Numerical Formulations of Conservation Laws,” in *26th Aerospace Sciences Meeting*, p. 127. 1988

[94] Yoon, S. and Jameson, A., “Lower-Upper Symmetric-Gauss-Seidel Method for the Euler and Navier-Stokes Equations,” *AIAA journal*, vol. 26, (9), pp. 1025-1026, 1988, doi: 10.2514/3.10007.

[95] Jain, R. K. and Potsdam, M. A., “Hover Predictions on the Sikorsky S-76 Rotor using Helios,” in *52nd Aerospace Sciences Meeting*, p. 0207. National Harbor, MD, January 13-17, 2014

[96] Owens, J. D., Houston, M., Luebke, D., Green, S., Stone, J. E., and Phillips, J. C., “GPU computing,” *Proceedings of the IEEE*, vol. 96, (5), pp. 879-899, 2008.

[97] Nickolls, J. and Dally, W. J., “The GPU computing era,” *IEEE micro*, vol. 30, (2), pp. 56-69, 2010.

[98] Barbely, N. L. and Komerath, N., “Coaxial Rotor Flow Phenomena in Forward Flight,” in *SAE 2016 Aerospace Systems and Technology Conference*, pp. 01-2009. Hartford, CT, September 27-29, 2016

[99] Barbely, N. L., Komerath, N. M., and Novak, L. A., “A Study of Coaxial Rotor Performance and Flow Field Characteristics,” in *American Helicopter Society Aeromechanics Specialists Conference*. San Francisco, CA, 2016

[100] Schatzman, N. L., "Aerodynamics and Aeroacoustic Sources of a Coaxial Rotor," Ph.D. Dissertation, School of Aerospace Engineering, Georgia Institute of Technology, 2018.

[101] Qi, H., Xu, G., Lu, C., and Shi, Y., “A Study of Coaxial Rotor Aerodynamic Interaction Mechanism in Hover with High-Efficient Trim Model,” *Aerospace Science and Technology*, vol. 84, pp. 1116-1130, 2019, doi: 10.1016/j.ast.2018.11.053.

[102] Kunze, P., “Evaluation of an Unsteady Panel Method for the Prediction of Rotor-Rotor and Rotor-Body Interactions in Preliminary Design,” in *41st European Rotorcraft Forum*. Munich, Germany, September 1-4, 2015

[103] Fernandes, S. D., "Performance Analysis of a Coaxial Helicopter in Hover and Forward Flight," Master's Thesis, Aerospace Engineering, Embry-Riddle Aeronautical University, Daytona Beach, FL, 2017.

[104] Gray, R. B., "An Aerodynamic Anlysis of a Single Bladed Rotor in Hovering and Low-Speed Forward Flight as Determined from Smoke Studies of the Vorticity Distribution in the Wake," Ph.D. Dissertation, Aeronautical Engineering Department, Princeton University, Princeton, NJ, 1956.

[105] Landgrebe, A. J., "The Wake Geometry of a Hovering Helicopter Rotor and its Influence on Rotor Performance," *Journal of the American Helicopter society,* vol. 17, (4), pp. 3-15, 1972, doi: 10.4050/JAHS.17.3.

[106] Hein, B. R. and Chopra, I., "Hover performance of a micro air vehicle: rotors at low Reynolds number," *Journal of the American Helicopter Society,* vol. 52, (3), pp. 254-262, 2007, doi: 10.4050/JAHS.52.254.

[107] Kunz, P. and Stawn, R., "Analysis and Design of Rotors at Ultra-Low Reynolds Numbers," in *40th AIAA aerospace sciences meeting & exhibit*, p. 99. Reno, NV, 2003

[108] Lakshminarayan, V. K. and Baeder, J. D., "Computational Investigation of Micro Hovering Rotor Aerodynamics," *Journal of the American Helicopter Society,* vol. 55, (2), pp. 22001-22001, 2010, doi: 10.4050/JAHS.55.022001.

[109] Gupta, V. and Baeder, J. D., "Low Mach Number Preconditioning for Tiltrotor Rotor-Wing Interaction," in *AHS 4th Decennial Specialists Conference on Aeromechanics*. San Francisco, CA, 2004

[110] Schroeder, E. and Baeder, J. D., "Using Computational Fluid Dynamics for Micro-Air Vehicle Airfoil Validation and Prediction," in *23rd AIAA applied aerodynamics conference*, p. 4841. Toronto, Ontario, Canada, 2005

[111] Ramasamy, M., "Measurements Comparing Hover Performance of Single, Coaxial, Tandem, and Tilt-Rotor Configurations," in *American Helicopter Society 69th Annual Forum*, vol. 31, p. 32. Phoenix, AZ, 2013

[112] Ma, Y., Chen, M., Zhang, X., and Wang, Q., "Scale-Model Tests of Coaxial Rotors in Water Tunnel via Particle Image Velocimetry Technique," *Proceedings of the Institution of Mechanical Engineers, Part G: Journal of Aerospace Engineering,* vol. 230, (3), pp. 426-443, 2016.

[113] Peters, D. A., "How dynamic inflow survives in the competitive world of rotorcraft aerodynamics," *Journal of the American Helicopter Society,* vol. 54, (1), pp. 11001-11001, 2009.

[114] Tongchitpakdee, C., Benjanirat, S., and Sankar, L. N., "Numerical simulation of the aerodynamics of horizontal axis wind turbines under yawed flow conditions," *Journal of Solar Energy Engineering,* vol. 127, pp. 464-474, 2005.

[115] Rigsby, J. M., "Stability and Control Issues Associated with Lightly Loaded Rotors Autorotating in High Advance Ratio," presented at the American Helicopter Society 64th Annual Forum Proceedings, Montreal, Canada, 2008

[116] Zhao, J., Prasad, J. V. R., and Peters, D. A., "Rotor dynamic wake distortion model for helicopter maneuvering flight," *Journal of the American Helicopter Society,* vol. 49, (4), pp. 414-424, 2004.

[117] Spalart, P. R. and Allmaras, S. R., "A One-Equation Turbulence Model for Aerodynamic Flows," in *30th aerospace sciences meeting and exhibit*, p. 439. 1992

[118] Spalart, P. R., "Trends in Turbulence Treatments," in *Fluids 2000 conference and exhibit*, p. 2306. 2000

[119] Spalart, P. R. and Rumsey, C. L., "Effective Inflow Conditions for Turbulence Models in Aerodynamic Calculations," *AIAA journal,* vol. 45, (10), pp. 2544-2553, 2007, doi: 10.2514/1.29373.

[120] Eca, L., Hoekstra, M., Hay, A., and Pelletier, D., "A Manufactured Solution for a Two-Dimensional Steady Wall-Bounded Incompressible Turbulent Flow," *International Journal of Computational Fluid Dynamics,* vol. 21, (3-4), pp. 175-188, 2007, doi: 10.1080/10618560701553436.

[121] Aupoix, B. and Spalart, P. R., "Extensions of the Spalart–Allmaras Turbulence Model to Account for Wall Roughness," *International Journal of Heat and Fluid Flow,* vol. 24, (4), pp. 454-462, 2003, doi: 10.1016/S0142-727X(03)00043-2.

[122] Cakmakcioglu, S. C., Bas, O., and Kaynak, U., "A Correlation-Based Algebraic Transition Model," *Proceedings of the Institution of Mechanical Engineers, Part C: Journal of Mechanical Engineering Science,* vol. 232, (21), pp. 3915-3929, 2018, doi: 10.1177/0954406217743537.

[123] Cakmakcioglu, S. C., Bas, O., Mura, R., and Kaynak, U., "A Revised One-Equation Transitional Model for External Aerodynamics," in *AIAA AVIATION 2020 FORUM*, p. 2706, doi: 10.2514/6.2020-2706. 2020

[124] Mura, R. and Cakmakcioglu, S. C., "A Revised One-Equation Transitional Model for External Aerodynamics-Part i: Theory, Validation and Base Cases," in *AIAA Aviation 2020 Forum*, p. 2714. 10.2514/6.2020-2714, 2020

[125] Menter, F. R., Langtry, R. B., Likki, S. R., Suzen, Y. B., Huang, P. G., and Vo¨lker, S., "A Correlation-Based Transition Model Using Local Variables: Part I—Model Formulation," in *Turbo Expo: Power for Land, Sea, and Air,* vol. 41693, pp. 57-67. June 2004, 2004

[126] Wu, J.-C., Huff, D. L., and Sankar, L. N., "Evaluation of Three Turbulence Models in Static Air Loads and Dynamic Stall Predictions," *Journal of Aircraft,* vol. 27, (4), pp. 382-384, 1990.

[127] Sahin, M., Sankar, L. N., Chandrasekhara, M. S., and Tung, C., "Dynamic stall alleviation using a deformable leading edge concept-a numerical study," *Journal of aircraft,* vol. 40, (1), pp. 77-85, 2003, doi: 10.2514/2.3060.

[128] Yamakawa, G. M., Winn, A. L., Smith, R. B., Anderson Jr, R. J., and Griffith, W. E., "Attack Helicopter Evaluation, Blackhawk S-67 Helicopter," National Technical Information Service, Edwards Air Force Base, CA, July 1972.

[129] Hariharan, N. S., Egolf, T. A., and Sankar, L. N., "Simulation of Rotor in Hover: Current State, Challenges and Standardized Evaluation," in *52nd Aerospace Sciences Meeting*, p. 0041. National Harbor, MD, January 13-17, 2014

[130] Hariharan, N. S., Egolf, T. A., Narducci, R., and Sankar, L. N., "Helicopter Rotor Aerodynamic Modeling in Hover: AIAA Standardized Hover Evaluations," in *53rd AIAA Aerospace Sciences Meeting*, p. 1242. Kissimmee, Florida, January 5-9, 2015

[131] Narducci, R., "Simulations of Rotor in Hover: Boeing Philadelphia," in *Proceedings of SciTech 2014*, vol. 2014, p. 0208. National Harbor, MD, January 13-17, 2014

[132] Baeder, J. D., Medida, S., and Kalra, T. S., "OVERTURNS Simulation of S-76 Rotor in Hover," in *52nd Aerospace Sciences Meeting*, p. 0045. National Harbor, MD, January 13-17, 2014

[133] Tadghighi, H., "Simulations of Rotor in Hover: Boeing Mesa," in *Proceedings of SciTech 2014*, vol. 2014, p. 0209. National Harbor, MD, January 13-17, 2014

[134] Sheng, C., Zhao, Q., and Wang, J., "S-76 Rotor Hover Prediction Using U2NCLE Solver," in *Proceedings of SciTech 2014*, doi: 10.2514/6.2014-0044. [Online]. Available: https://arc.aiaa.org/doi/abs/10.2514/6.2014-0044, National Harbor, MD, January 13-17,

[135] Jung, M. K., Hwang, J. Y., and Kwon, O. J., "Assessment of Rotor Aerodynamic Performances in Hover using an Unstructured Mixed Mesh Method," in *Proceedings of SciTech 2014*, p. 0042. National Harbor, MD, January 13-17, 2014

[136] Marpu, R., Dewan, Y., Zhou, C., and Sankar, L. N., "Numerical Design Optimization of the S-76 Rotor for Hover Performance," in *Proceedings of SciTech 2014*. National Harbor, MD, January 13-17, 2014

[137] Marpu, R., Sankar, L. N., Egolf, T., and Hariharan, N., "Simulation of S-76 Rotor in Hover Using a Hybrid Methodology," in *Proceedings of SciTech 2014*, vol. 2014, p. 0210. National Harbor, MD, January 13-17, 2014

[138] Kim, J., Sankar, L. N., Marpu, R., Egolf, T. A., and Hariharan, N., "A Parametric Study of Planform Effects on Rotor Hover Performance Using a Hybrid Navier Stokes-Free Wake Methodology," in *Proceedings of SciTech 2014*. National Harbor, MD, January 13-17, 2014

[139] Sankar, L. N. and Hariharan, N. S., "High Order Evaluation of S-76 in Hover," in *53rd AIAA Aerospace Sciences Meeting*, doi: 10.2514/6.2015-1714. Kissimmee, Florida, January 5-9, 2015

[140] Min, B.-Y., Reimann, C. A., Wake, B., Jee, S. K., and Baeder, J. D., "Hovering Rotor Simulation Using OVERFLOW with Improved Turbulence Model," in *2018 AIAA Aerospace Sciences Meeting*, p. 1779. 2018

[141] Abras, J. and Hariharan, N. S., “Parameter Studies on the S-76 Rotor Using HELIOS,” in *55th AIAA Aerospace Sciences Meeting*, p. 1431. Grapevine, Texas, 2017

[142] “Turing GPU Architecture Whitepaper,” NVIDIA Corporation, https://images.nvidia.com/aem-dam/en-zz/Solutions/design-visualization/technologies/turing-architecture/NVIDIA-Turing-Architecture-Whitepaper.pdf (accessed May, 2021).

VITA

Po-Wei Chen was born in August 1989 in Chiayi city, Taiwan. He received his Bachelor of Science in Physics from National Chung Cheng University in June 2011. During his study in National Chung Cheng University, he was awarded President's Fellowship and received 1st place for the interdisciplinary research competition. Po-Wei received a Master of Science degree in Aeronautical Engineering from National Cheng Kung University in June 2015. His master's thesis focused on both experimental and numerical study on the external aerodynamics of low-aspect-ratio wing at low Reynolds numbers. He joined the Daniel Guggenheim School of Aerospace Engineering at Georgia Institute of Technology in August 2016. During his Ph.D. studies, Po-Wei enhanced the hybrid Navier-Stokes/free wake methodology solver (GT-Hybrid) for general multi-rotor configurations operating in broad range of the flow conditions including laminar, transition, and turbulent flow. He is a member of the Vertical Flight Society since 2017. Upon graduation he plans to work at ANSYS, Inc.